X-ray emission from nearby early-type galaxies and origin of Type Ia Supernovae

Ákos Bogdán

München 2010

X-ray emission from nearby early-type galaxies and origin of Type Ia Supernovae

Ákos Bogdán

Dissertation
an der Fakultät für Physik
der Ludwig–Maximilians–Universität
München

vorgelegt von
Ákos Bogdán
aus Pécs, Ungarn

München, den 23. 12. 2009

Erstgutachter: Prof. Dr. Rashid Sunyaev
Zweitgutachter: Prof. Dr. Gerhard Börner
Tag der mündlichen Prüfung: 25. 02. 2010

Summary

In this dissertation we consider several astrophysical phenomena. We reveal the nature of progenitors of Type Ia Supernovae (SNe Ia), derive constraints on progenitors of Classical Novae, and investigate the origin and properties of the unresolved X-ray emission in Andromeda galaxy (M31).

Type Ia Supernovae, used as standards candles, played a major role in establishing that the Universe undergoes an accelerated expansion, the fact that directly pointed at the existence of dark energy. Although there is a general agreement that SNe Ia originate from thermonuclear explosions of white dwarf stars, the nature of their progenitors is still debated. The nuclear runaway could arise from a white dwarf gradually accumulating matter from a companion star until it reaches the Chandrasekhar mass limit, or from two white dwarfs merging in a compact binary. The X-ray signatures of the two possible paths are completely different. Whereas no strong electromagnetic emission is expected in the merger scenario until shortly before the supernova, the white dwarf accreting material from the normal star becomes a source of copious X-rays for about 10^7 years before the explosion. This offers a means to determine which scenario dominates. We demonstrated that the X-ray flux from a sample of six early-type galaxies is factor of about $30 - 50$ times less than predicted in the accretion scenario. Therefore at most 5 per cent of SNe Ia in early-type galaxies can be produced by accreting white dwarfs.

Using a similar line of arguments we derived constraints on the nature of Classica Nova (CN) progenitors. CNe are nuclear explosions occuring upon accumulation of certain amount of hydrogen-rich material on the surface of an accreting white dwarf in a close binary system. The accretion energy is released in the optical, ultraviolet, or X-ray wavelengths, depending on the type of the progenitor system. In magnetic systems (polars and intermediate polars) and dwarf novae in quiescence it is mainly emitted in the X-ray regime. Comparing the X-ray flux from these systems with the observed value in the bulge of M31, we placed an upper limit of about 10 per cent on the contribution of magnetic systems to the observed CN rate. We also demonstrated that in dwarf novae at least 90 per cent of the material is accreted during outburst periods, and only small fraction during quiescent periods.

We studied M31, the nearby spiral galaxy, to understand the nature of the unresolved X-ray emission. After removing the bright resolved point sources (accreting neutron stars and black holes in binary stellar systems), we showed that the unresolved emission consists of three components. One of the them is associated with the old stellar population and it is built up from a large number of faint sources, mainly accreting white dwarfs and stars with active stellar coronae, similar to the Galactic ridge X-ray emission of the Milky Way. We also revealed the presence of hot ionized gas, located in the bulge of M31. The

temperature of the gas is about $(3 – 4) \cdot 10^6$ K and its total mass is about $2 \cdot 10^6$ $M_\odot$. From the morphology and physical conditions of the gas we concluded that it outflows from the galaxy perpendicular to its plane. Such an outflow can be sustained by the mass loss of evolved stars and it can be driven by the energy release of SNe Ia. We also detected a shadow cast on the gas emission by spiral arms and the 10-kpc star-forming ring, that allowed us to estimate the vertical off-plane extent of the gas outflow – it is greater than 2.5 kpc. The third X-ray emitting component is associated with the spiral arms of M31. Presumably the observed emission, originating from the star forming regions, is due to the population of young stellar objects and young stars, which are well-known sources of X-ray radiation.

Zusammenfassung

In dieser Arbeit betrachten wir verschiedene astrophysikalische Phänomene. Insbesondere zeigen wir neue Erkenntnisse über die Vorläuferobjekte von Typ Ia Supernovae (SNe Ia) und leiten Bedingungen für die Vorläufersysteme von klassischen Novae ab. Außerdem untersuchen wir Ursprung und Eigenschaften nicht-aufgelöster Röntgenstrahlung in der Andromedagalaxie (M31).

Die Verwendung von SNe Ia als Standardkerzen zur Entfernungsmessung spielt eine zentrale Rolle in der Beweisführung, dass das Weltall einer beschleunigten Expansion unterliegt, die von einer “dunklen Energie” getrieben wird. Allerdings sind die Vorläuferobjekte von SNe Ia bisher unbekannt. Heute wird zwar allgemein akzeptiert, dass diese leuchstarken Objekte von thermonuklearen Explosionen eines weißen Zwergsterns herrühren, allerdings ist unsicher was die Explosion auslöst. Hierfür werden verschiedene Szenarien diskutiert: (i) die Akkretion von Gas aus der Hülle eines Begleitsterns bis der weiße Zwerg die Chandrasekharmasse erreicht, oder (ii) das Verschmelzen eines engen Doppelsternsystems aus zwei weißen Zwergen, deren Gesamtmasse die Chandrasekharmasse übersteigt. Da die emittierte Röntgenstrahlung in diesen beiden Szenarien völlig verschieden ist, lassen sich die Vorläuferobjekte durch Beobachtungen einschränken. Während beim Verschmelzen zweier weißer Zwerge bis kurz vor der Supernova keine erhebliche elektromagnetische Emission stattfindet, wird im Akkretionsszenario für ungefähr 10^7 Jahre vor der Explosion massiv Röntgenstrahlung frei. Wir demonstrieren, dass die Röntgenemission in sechs ausgewählten Galaxien frühen Typs ungefähr $30 - 50$ mal geringer ist, als im Akkretionsszenario erwartet. Daher können maximal 5 Prozent der SNe Ia in diesen Galaxien von akkretierenden weißen Zwergen stammen.

Ähnliche Argumente ermöglichen es die Eigenschaften von Vorläufersystemen klassischer Novae einzuschränken. Dabei handelt es sich um akkretierende weiße Zwerge in denen das akkretierte Material vor Erreichen der Chandrasekharschen Massengrenze durch eine thermonukleare Explosion an der Oberfläche verbrennt. Abhängig von der Akkretionsgeometrie wird die freigesetzte Energie in einem charakteristischen Wellenlängenbereich abgestrahlt: in magnetischen Systemen (polars und intermediate polars) und Zwergnovae in Ruhe vor allem im Röntgenlicht. Durch einen Vergleich der erwarteten Röntgenemissionen von diesen Systemen mit der beobachteten Leuchtkraft in der Bulge von M31 finden wir eine obere Grenze von ungefähr 10 Prozent für den Anteil von magnetischen Systemen an der beobachteten Rate klassicher Novae. Außerdem finden wir, dass in Zwergnovae mindestens 90 Prozent des Materials während Ausbruchsperioden akkretiert werden.

Für die nahe gelegene Spiralgalaxie M31 zeigen wir schließlich, dass die nach Subtraktion der hellen

kompakten Quellen (akkretierende Neutronensterne und schwarze Löcher in Doppelsternsystemen) nicht-aufgelöste Röntgenemission aus drei Komponenten besteht. Eine dieser Komponenten stammt aus der Überlagerung viel schwächerer kompakter Quellen, nämlich aus akkretierenden weißen Zwergen und Sternen mit aktiven Vorgängen in ihren heißen Gashüllen. So erklärt beispielsweise die gemeinsame Strahlung schwacher Quellen den Großteil oder sogar die gesamte Röntgenstrahlung aus der Scheibe unserer Galaxis. Eine weitere Komponente bildet heißes ionisiertes interstellares Gas in der Bulge von M31. Die Temperatur dieses Gases beträgt ungefähr $3 \cdot 10^6$ K, und seine Masse ist ungefähr $2 \cdot 10^6$ $M_\odot$. Form und spektrale Merkmale deuten darauf hin, dass dieses Gas vorwiegend orthogonal zur Scheibe aus der Galaxie ausströmt. Dieser Ausfluss kann durch die Energiefreisetzung von SNe Ia und durch den Massenverlust entwickelter Sterne erklärt werden. Da die Spiralarme und die Sternbildungsregion einen Schatten auf das ionisierte Gas werfen, konnten wir eine untere Grenze von 2.5 kpc für die vertikale Ausdehnung des Ausfluss festlegen. Die dritte röntgenstrahlende Komponente ist mit den Spiralarmen verbunden und vermutlich auf junge stellare Objekte und junge Sterne in Sternbildungsregionen zurückzuführen, welche wohlbekannte Quellen von Röntgenstrahlung sind.

Contents

List of Figures

List of Tables

Chapter 1

Introduction

1.1 Type Ia Supernovae

1.1.1 General properties

Supernovae are among the brightest transient objects of the Universe. These events, often outshining their host galaxy and sometimes bright enough to be visible in daytime, have always impressed mankind. The prompt appearance and the extraordinary brightness of Supernovae made them detectable long before the invention of telescopes. The earliest recorded Supernova, SN185, was observed by Chinese astronomers, whereas SN 1006 and SN 1054 were chronicled and described in details by Chinese and Arab astronomers – the latter Supernovae formed the Crab Nebula (Lundmark, 1921). The first modern observations of Supernovae are reported by Tycho Brahe (SN 1572) and Johannes Kepler (SN 1604). These detections were essential for the improvement of modern astronomy since they played an important role in the revision of the geocentric worldview of Aristotle. The first extragalactic Supernova, which was even visible with naked eye, was observed in the bulge of M31 in 1885 (Hartwig, 1898).

The detailed study of these very luminous events started in the 20th century. Baade & Zwicky (1934) were the first to make a distinction between “Common-novae” and “Super-novae”, also realizing that Supernovae are much brighter and less frequent. Further studies of these events pointed our that their spectra are not uniform and they can be classified upon the presence of Balmer-lines in their spectra. Type I Supernovae do not contain hydrogen lines, whereas Type II Supernovae show hydrogen spectral features (Minkowski, 1941).

The modern classification scheme of Supernovae, illustrated in Figure 1.1, relies exclusively on their observed properties – on spectral characteristics and light curves. Keeping the two main classes of Supernovae, introduced by Minkowski (1941), the Type I class is further divided into Ia, Ib, and Ic subclasses depending on the presence of silicon and helium spectral features. Type II Supernovae are categorized based on the light curve shape: IIP have a slower decline Plateau and IIL have Linear decline. However note, that these definitions are less precise than those based on spectral features for Type I objects.

There is an overall agreement that Supernovae are produced in two different physical mechanisms. On the one hand Type Ia Supernovae (SNe Ia) arise from thermonuclear explosions of degenerate white dwarf stars approaching the Chandrasekhar mass limit ($M_{Ch} \approx 1.38$ M$_\odot$). On the other hand Type Ib,

Ic, and Type II Supernovae are the result of a compact iron core collapse in an evolved star with mass exceeding about 9 $M_{\odot}$. The subclasses of core collapse Supernovae are thought to originate from the somewhat different evolution of the progenitor stars. Observations of the most energetic core collapse Supernovae, the so-called "Hypernovae", indicate that these events may be connected to long Gamma Ray Bursts (Iwamoto et al., 1998).

In the present work we focus on SNe Ia. In Section 1.1.2 the astrophysical importance of Type Ia Supernovae is overviewed and in Section 1.1.3 the most enigmatic problem in our understanding about SNe Ia is introduced.

1.1.2 Relevance of Type Ia Supernovae in cosmology

One of the most exciting findings of the last decades is that the Universe undergoes an accelerated expansion (Riess et al., 1998; Perlmutter et al., 1999) since around $z \approx 0.5$ (Riess et al., 2004). In order to come to this conclusion it was indispensable to recognize that SNe Ia can be used as standard candles.

In astrophysics, a standard candle is an object with known absolute brightness, allowing to infer the distance to the object from its measured apparent brightness. The cosmic distance ladder starts with the trigonometrical parallax method, enabling to measure distances up to about 1 kpc with high precision, e.g. the *Hipparcos* satellite could obtain accurate distances of $\sim 10^5$ nearby stars. At larger distances the

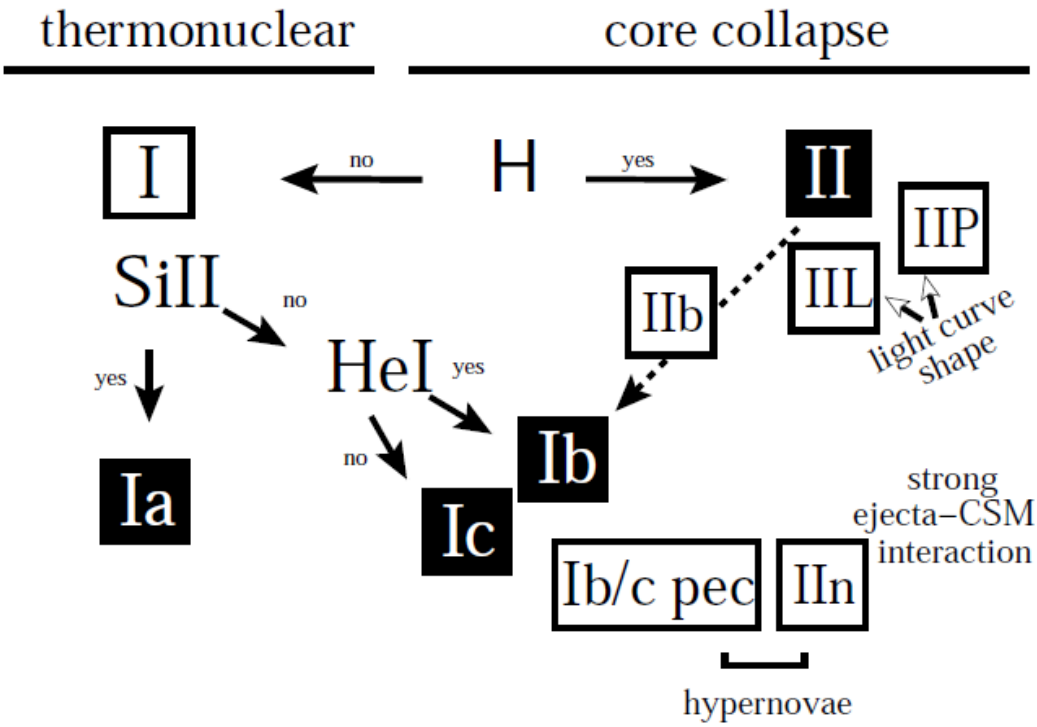

Figure 1.1: Modern classification scheme of Supernovae, taken from Turatto (2003). Note, that Type Ia Supernovae are the result of thermonuclear explosions of white dwarf stars, whereas other Supernovae originate from the compact iron core collapse in massive evolved stars.

correlation between the pulsation period and the absolute magnitude of RR Lyrae and Cepheid variable stars allows the precise measurement of distances up to ~ 1 Mpc and ~ 40 Mpc with the *Hubble Space Telescope*.

Early observations of SNe Ia indicated that their luminosity is uniform (Zwicky, 1939). Accordingly, they could serve as distance indicators at cosmological distance scales due to their outstanding brightness. However, more precise observations of SNe Ia pointed out that they are not standard candles since their peak brightness show a scatter of about 2 magnitudes and their decline rate is also not uniform. An important step towards the extension of the cosmic distance ladder was to recognize that SNe Ia can be "standardized" (Phillips, 1993; Hamuy et al., 1996a; Riess et al., 1996; Perlmutter, 1997). By means of empirical relationships between the peak luminosity and the light curve shape, they can be used as

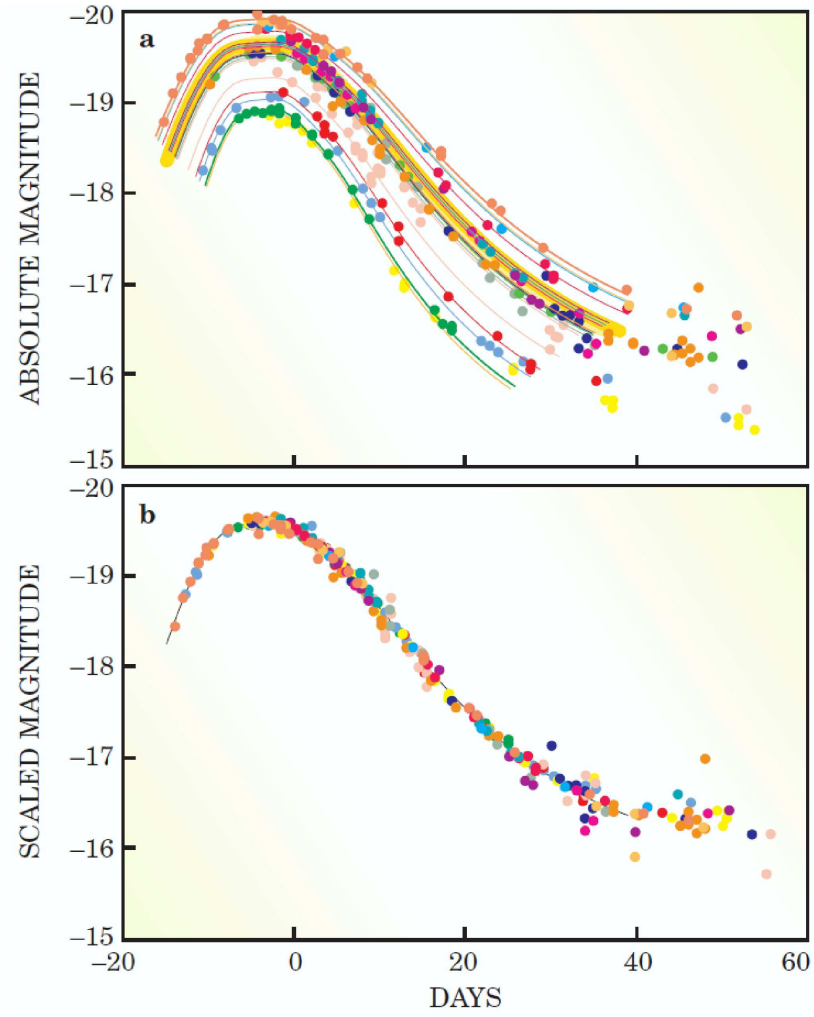

Figure 1.2: Light curves of nearby SNe Ia (Perlmutter, 2003). On the upper panel their absolute magnitude is plotted against the decay time. Note, that most SNe Ia are in the thick yellow band. The brighter ones have wider light curves whereas the fainter ones exhibit narrower light curves. On the lower panel the light curves of outlier SNe Ia are stretched and their brightness is adjusted accordingly, as a result all light curves match to each other.

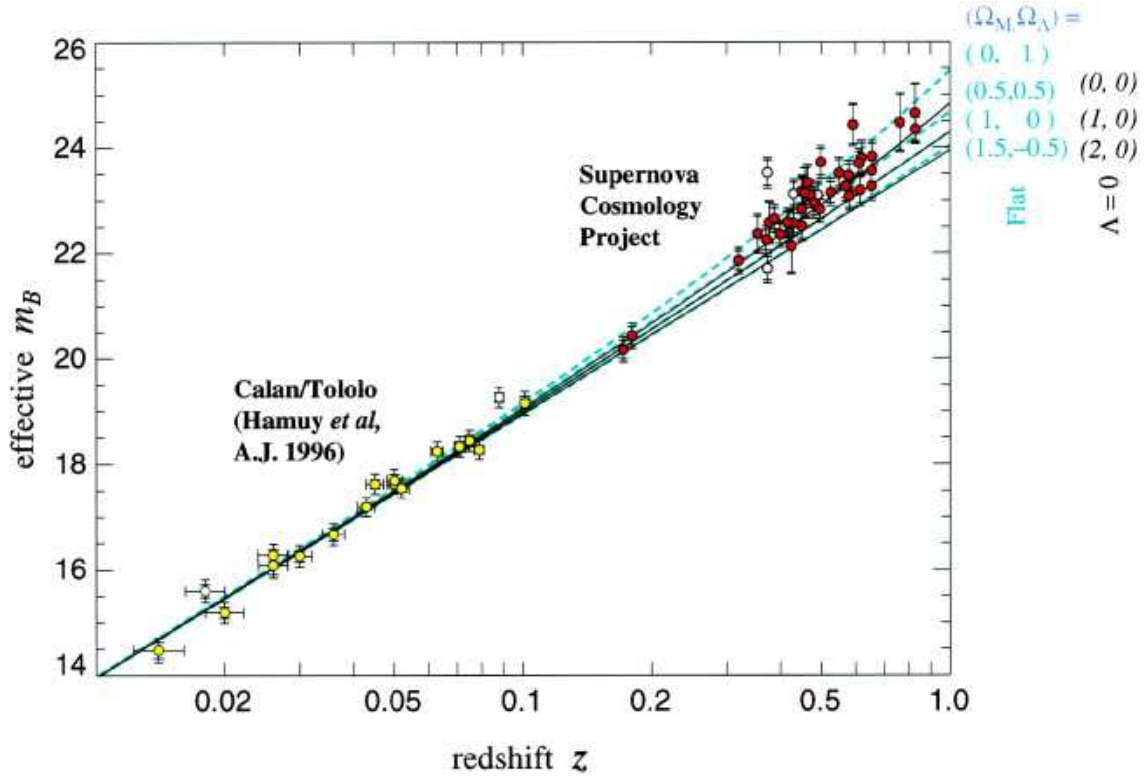

Figure 1.3: Hubble diagram for 42 high redshift and 18 low redshift SNe Ia, taken from Perlmutter et al. (1999). The solid lines indicate the theoretical effective $m_B(z)$ for various cosmological models for a range of Ω_M and Ω_Λ.

distance indicators, as illustrated in Figure 1.2. Another key ingredient was the two large and homogeneous supernova samples with multifilter lightcurves of the Calán/Tololo (Hamuy et al., 1996b) and of the Harvard-Smithsonian Center for Astrophysics survey (Riess et al., 1999). Using a nearby sample of SNe Ia, the corrections to the light curve shapes were determined. With these corrections, objects at small distances ($z \lesssim 0.1$) follow a straight line in the Hubble-diagram[1]. The application of SNe Ia at high redshifts ($z \approx 1$) led to the unexpected result that more distant objects are dimmer by ≈ 0.25 magnitudes than expected in an empty Universe ($\Omega = 0$) as shown in Figure 1.3 (Riess et al., 1998; Perlmutter et al., 1999). This observational outcome implies that SNe Ia at large redshifts are more distant than expected.

Using the above described results the density parameters of matter (Ω_M) and cosmological constant (Ω_Λ) can be determined. In order to explain fainter SNe Ia at large redshifts a non-zero Ω_Λ is needed, which implies the existence of an energy component with negative pressure, similarly to the cosmological constant of Einstein. Beyond SNe Ia there are several other methods aiming to measure the matter and energy density: (i) the measurement of anisotropies of the cosmic microwave background with the *Wilkinson Microwave Anisotropy Probe* (*WMAP*) (Spergel et al., 2003), (ii) constraints from the large-scale structure of 2dF Galaxy Redshift Survey (Percival et al., 2001), (iii) baryon acoustic oscillations (e.g. Cole et al., 2005; Eisenstein et al., 2005), or (iv) galaxy cluster mass functions (Vikhlinin et al., 2009). The resulting density parameters from all methods are consistent with those obtained from SNe Ia. Combining all results

[1]The Hubble-diagram connects the redshift and the apparent brightness of an object with known absolute brightness.

we obtain the currently favored ΛCDM model[2] with $\Omega_M \approx 0.26$ and $\Omega_\Lambda \approx 0.74$.

Using a larger sample of SNe Ia, the physical model, responsible for the accelerated expansion of the Universe, can be tested by determining the equation-of-state parameter *w*, which connects the energy density with the pressure: $p = w\rho c^2$. This reveals whether the dark energy is caused by vacuum energy density or quintessence models (Caldwell et al., 1998) are needed to explain the accelerated expansion of the Universe. The largest SNe Ia surveys, the Supernova Legacy Survey (SNLS) (Astier et al., 2006) and the ESSENCE project (Wood-Vasey et al., 2007) obtained $w = -1$ within ∼ 10 per cent uncertainties. This value is consistent within 1σ with a cosmological constant.

In conclusion, SNe Ia are a powerful tool for cosmological distance measurements, moreover they can be used to study the global geometry of the Universe. However, to make even more precise constraints about the time evolution of *w* the systematic uncertainties in their absolute magnitude need to be further decreased. To achieve this goal, it is essential to understand SNe Ia in all details.

1.1.3 Progenitor systems of Type Ia Supernovae

One of the most interesting questions regarding SNe Ia is how they are exactly produced. In this Section the composition of the progenitor white dwarf star is discussed and the potential evolutionary channels are described.

There are three possible compositions of white dwarfs, that in principle, could lead to a SNe Ia: helium, oxygen-neon, and carbon-oxygen. Helium white dwarfs have typical mass of $M_{WD} \sim 0.45$ $M_\odot$ (Iben & Tutukov, 1985) and they can explode following a central He ignition at the mass of ~ 0.7 $M_\odot$. A strong objection against helium white dwarfs is that the composition of the ejecta contains only unburned helium, ^{56}Ni, and its decay products (Nomoto & Sugimoto, 1977) – being completely inconsistent with observational data of SNe Ia. Oxygen-neon white dwarfs are believed to undergo an accretion-induced collapse when reaching the Chandrasekhar mass limit instead of an explosion (Nomoto & Kondo, 1991). Moreover, their number statistics is too small to be the main evolutionary channel of SNe Ia. Therefore oxygen-neon white dwarfs also have to be excluded. Carbon-oxygen white dwarfs are the best candidates, since they are produced in large number in main-sequence stars below $\lesssim 8$ $M_\odot$, and they are expected to produce a supernova explosion when approaching the Chandrasekhar mass limit (Nomoto & Kondo, 1991). The fate of a carbon-oxygen white dwarf is shown in Figure 1.4. To conclude, there is a general agreement that SNe Ia are associated with the thermonuclear explosions of carbon-oxygen white dwarf stars.

An enigmatic question about SNe Ia is the evolutionary channel, in which the white dwarf nears the Chandrasekhar mass. The two proposed evolutionary channels are the double-degenerate and the single-degenerate scenarios. The double-degenerate scenario employs the coalescence of two carbon-oxygen white dwarfs in close binary systems due to emission of gravitational waves (Iben & Tutukov, 1984; Webbink, 1984). Alternatively, in the single-degenerate channel carbon-oxygen white dwarfs accrete hydrogen-rich material from their non-degenerate companion until they approach the Chandrasekhar

[2]The so-called Lamba-Cold Dark Matter model, often referred to as concordance model, is currently the most accepted cosmological model that is in good agreement with observed phenomena of the Universe.

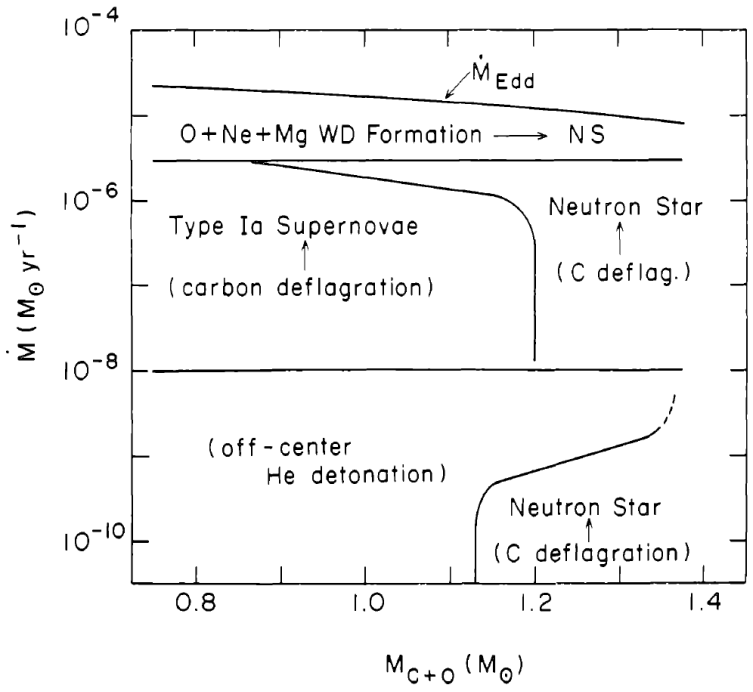

Figure 1.4: The fate of an accreting carbon-oxygen white dwarf as a function of their initial mass (M_{C+O}) and accretion rate ($\dot{M}$) (Nomoto & Kondo, 1991). In the neutron star regime the white dwarf collapses instead of undergoing a thermonuclear explosion.

mass limit (Whelan, & Iben, 1973).

The most attractive feature in the double-degenerate scenario is that it explains naturally the absence of hydrogen in the spectrum of SNe Ia. The fact, that white dwarfs are typically produced in the mass range of $\sim 0.5 - 0.8$ $M_\odot$ (Homeier et al., 1998) also favors this scenario, as it is relatively easy to exceed the Chandrasekhar mass limit in a double white dwarf system. Moreover, population synthesis studies are able to reproduce the observed SN Ia rate with the double-degenerate scenario (Branch et al., 1995). However, there are also strong objections against this scenario. Most importantly, the homogeneity of SNe Ia is strongly questionable if two white dwarfs having different "initial conditions" (mass, composition, and angular momentum) need to produce (almost) the same burning conditions. It is also unclear, whether the merger of two white dwarfs could trigger a thermonuclear explosion leading to a SN Ia, or it results rather an accretion-induced collapse (Nomoto & Iben, 1985; Woosley & Weaver, 1986; Saio & Nomoto, 1985, 1998). Recently, Pakmor et al. (2009) demonstrated by performing hydrodynamical simulations that equal-mass white dwarf mergers may lead to thermonuclear explosions[3] if the total mass of the system exceeds ~ 1.8 $M_\odot$.

The other alternative progenitor channel, the single-degenerate scenario can explain the observed homogeneity of SNe Ia, since the thermonuclear explosion is bound to the Chandrasekhar mass. The upper limit of the initial mass of a carbon-oxygen white dwarf is ~ 1.2 $M_\odot$ (Weidemann, 2000), hence the system

[3]In fact they showed that explosions triggered by the merger of two 0.9 $M_\odot$ white dwarfs are faint and their observational characteristics resemble to those of the sub-luminous 1991bg-like events. Although even more massive systems could explain brighter SNe Ia, they are not numerous enough to account for the observed frequency of SNe Ia.

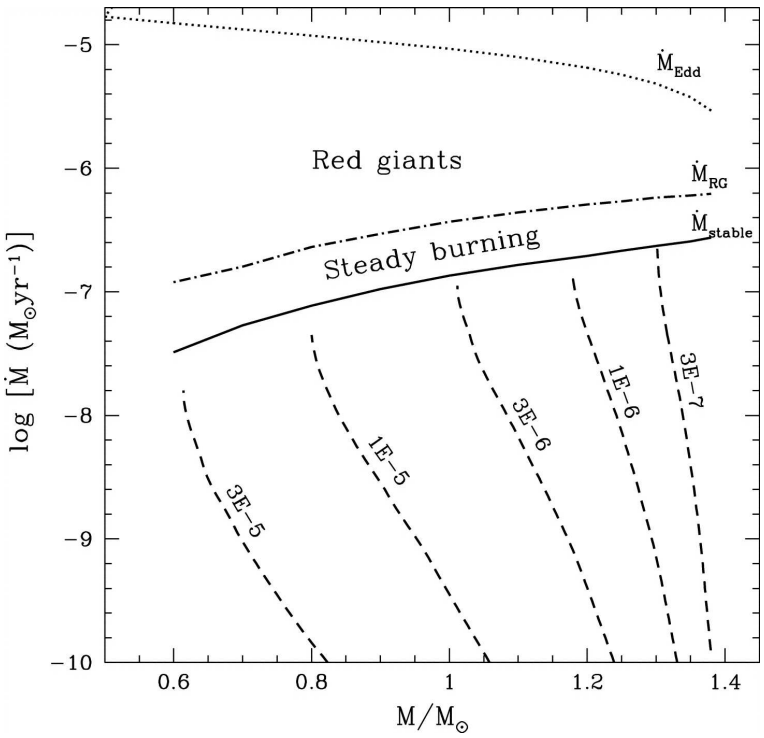

Figure 1.5: Parameter space of hydrogen burning on the surface of a white dwarf shown in the plane of its mass (M) and accretion rate ($\dot{M}$) (Nomoto, 1982). Thermally stable hydrogen burning occurs in the range between the solid and dashed-dotted horizontal lines. Below this region the hydrogen burning proceeds in flashes giving rise to nova outbursts. At high accretion rates the stellar envelope expands to red giant dimensions or an optically-thick wind evolves.

inevitably needs to accrete ~ 0.2 M$_\odot$ matter before the Chandrasekhar mass limit is reached. However, the mass of the white dwarf can grow only in a very "fine-tuned" binary system. Three regimes can be differentiated in the parameter space of white dwarf mass (M_{WD}) and accretion rate ($\dot{M}$) (Figure 1.5). In a rather narrow range of accretion rates the accumulated hydrogen burns steadily to helium and possibly further to carbon and oxygen, therefore the white dwarf can increase its mass. The required accretion rate for the stable nuclear burning is $\sim 10^{-7}$ M$_\odot$/yr. If the accretion rate is smaller, the hydrogen burning becomes unstable to flashes. The shell flashes give rise to Classical Nova (CN) eruptions, during which most of the accreted and some of the original white dwarf material is lost. As a consequence the white dwarf is not able to grow in mass and never reaches the Chandrasekhar mass. For very high accretion rates, the white dwarf radius expands to red giant dimensions, it even may engulf the donor star and form a common envelope configuration (Nomoto et al., 1979; Livio, 2000). However, this envelope is ejected on a time scale of ~ 1000 years (Taam & Sandquist, 2000), and within this time the white dwarf mass can not increase by more than 10^{-3} M$_\odot$ (Livio, 2000). Calculations by Hachisu et al. (1996) indicated that at high accretion rates, instead of a common envelope, an optically-thick wind may form with photospheric velocities of ~ 1000 km s^{-1} (Hachisu et al., 1999). However, observations of SN Ia remnants are incompatible with the presence of strong accretion winds (Badenes et al., 2007). A further problem with the single-degenerate scenario is that population synthesis studies suggest that this evolutionary channel may contribute at most

$\sim$ 10 per cent to the observed SN Ia frequency (Yungelson et al., 1995, 1996).

Although it is quite uncertain whether accreting white dwarfs are able to reach the Chandrasekhar mass eventually, a strong argument favors the single-degenerate scenario. A class of objects, namely the supersoft X-ray sources, could be identified which are potential progenitors of SNe Ia (Greiner et al., 1991; van den Heuvel et al., 1992; Kahabka & van den Heuvel, 1997), see the discussion in Section 1.2.2. This confirms the theory that hydrogen burning on the surface of a white dwarf can proceed steadily, even if only in a narrow range of accretion rates.

A subclass of the single-degenerate models are the so called sub-Chandrasekhar models. In this scenario the carbon-oxygen white dwarf does not reach the critical density and temperature needed for the explosive carbon burning, instead the ignition occurs by an external trigger. This mechanism could be the detonations of an accreted helium layer, which can produce a strong flash that initiates the carbon detonation (e.g. Iben & Tutukov, 1984). The advantage of this model is that it does not get into conflict with population synthesis studies, and it does not have to reach the Chandrasekhar mass limit. However, the models obtained for these systems failed so far to reproduce the observed spectra and light curves of SNe Ia (Höflich & Khokhlov, 1996; Nugent et al., 1997), despite continuing effort (Fink et al., 2007).

In Chapter 2 we further investigate the progenitor scenarios of SNe Ia in early-type galaxies based on *Chandra* observations (Gilfanov & Bogdán, 2010).

1.2 X-ray emission from galaxies

The study of X-ray emission from normal galaxies was started after the launch of *Einstein Observatory* in 1978 (Giacconi et al., 1979). During three and a half years time of its operation more than 100 galaxies were observed. The high sensitivity and the few arcsecond angular resolution allowed to study the X-ray morphology and spectra of galaxies, and also numerous bright X-ray sources could be resolved in the Magellanic Clouds and in the Andromeda galaxy. Since the era of *Einstein Observatory* several X-ray satellites have been launched, contributing essentially to our understanding about the origin and properties of X-ray emission from galaxies. The most successful and outstanding missions are *ROSAT*, *ASCA* and the currently operating *Chandra X-ray Observatory* (*Chandra*) and *XMM-Newton*.

The origin of the X-ray emission from normal galaxies is diverse. In majority of galaxies, the X-ray emission is dominated by the population of bright X-ray binaries (see Fabbiano, 2006, for a review). Their typical luminosity is in the range of $\sim 10^{35} - 10^{39}$ erg s^{-1}. These binary systems consist of a compact object, which can be either a neutron star or a black hole, and a normal star. The compact object accretes material from the donor star and during accretion copious X-rays are liberated. X-ray binaries are classified based on the mass of the secondary star to high-mass X-ray binaries (HMXBs) and to low-mass X-ray binaries (LMXBs).

The population of cataclysmic variables (CVs) also adds a notable contribution to the observed X-ray emission of galaxies. These systems possess a degenerate white dwarf star and a normal star. The accretion onto the white dwarf is the source of X-ray emission but due to their shallower potential well the typical emitted luminosity is in the range of $\sim 10^{31} - 10^{35}$ erg s^{-1}. According to their relatively low brightness,

majority of these sources can not be resolved at extragalactic distances.

Other type of discrete sources, such as Supernova remnants or coronal emission from stars also emit X-ray radiation. These are rather weak sources, e.g. the luminosity of stellar coronae is of the order of $\sim 10^{28} - 10^{33}$ erg s^{-1} (Vaiana et al., 1981).

X-ray emission from hot ionized gas with sub-keV temperatures is also present (see Mathews & Brighenti, 2003, for a review). The amount of the gas component varies from galaxy to galaxy, usually more massive galaxies are gas-rich and less massive ones tend to be gas-poor.

In this Section we overview the various X-ray emitting components from normal early-type galaxies. We discuss briefly the properties of X-ray binaries in Section 1.2.1, CVs are in focus in Section 1.2.2, and we introduce X-ray emission from hot ionized gas in Section 1.2.3.

1.2.1 X-ray binaries

Although most stars are born in binary systems, X-ray binaries are relatively rare due to the special conditions required for their formation. On the one hand, a very massive star is needed to form a black hole or a neutron star on the other, the orbital separation also has to be "fine-tuned". If the separation of the binary is too small, they can merge in the common envelope phase, but if it is too large, the mass transfer in the system can not start. Beyond these, the evolutionary stage of the donor star also plays a crucial role in the formation of an X-ray binary. As a result, in average about 140 bright LMXBs ($L_X > 10^{37}$ erg s^{-1}) are formed per 10^{11} $M_\odot$.

The mass transfer onto the compact object occurs either via Roche-lobe overflow or via strong stellar winds from the secondary star [4]. The Roche-lobe of the donor star can be filled by two mechanisms: either it evolves off the main sequence during which it expands, or the Roche-lobe shrinks due to gravitational radiation and magnetic braking. If the Roche-lobe is filled, material flows through the Lagrangian point (L_1) towards the compact object. To transfer enough material by stellar winds a rather massive, at least ~ 5 $M_\odot$, star is needed, therefore the wind accretion plays a role only in HMXBs.

The observed luminosity of X-ray binaries is due to accretion onto the compact object. As the secondary star transfers mass through the Lagrangian point, it forms an accretion disk around the white dwarf. The accretion process was described by Shakura & Sunyaev (1973) by a geometrically-thin and optically-thick disk of gas. The disk has an anomalous viscosity that transports angular momentum outwards and thus allows the accretion of matter onto the compact object. This process releases energy from the surface of the disk covering a broad wavelength-range. Since the temperature of the disk is inversely dependent on its radius, X-rays are primarily liberated at the inner disk.

1.2.2 Cataclysmic variables

Cataclysmic variables (CVs) are binary systems in which degenerate white dwarf stars accrete material from their non-degenerate secondary stars. One of the most outstanding characteristics of CVs is that

[4]The two mechanisms for transferring material onto the compact objects does not apply only for X-ray binaries but also for CVs.

they show variations on time scales of days-weeks-years. Based on the strength of the magnetic field we differentiate magnetic and non-magnetic CVs[5]. Considering the outburst frequencies the major subclasses are Classical Novae (CNe), Recurrent Novae (RNe), Nova-like variables (NLs), and Dwarf Novae (DNe).

In this Section we give a general overview about major properties of various CV subclasses and we also discuss a special case of accreting white dwarfs, the so-called supersoft X-ray sources.

Classical Novae, Recurrent Novae and Nova-like variables

Classical Novae have one recorded outburst, during which the brightness of the system increased by 6 – 19 magnitudes. Nova outbursts are caused by thermonuclear runaways on the surface of white dwarf stars in cataclysmic variable systems. The accreted hydrogen-rich material from the companion star accumulates on the surface of a white dwarf in a shell. As the mass of the shell increases, its pressure reaches the critical value needed to trigger a thermonuclear explosion, giving rise to a nova (Fujimoto, 1982).

CNe are very energetic events, their total energy release[6] is of the order of 10^{44} – 10^{45} ergs. This energy can expel the accreted shell and probably some of the original white dwarf material is also lost. The substantial mass loss ($\Delta M \sim 10^{-4}$ – 10^{-5} $M_\odot$) forms an expanding envelope around the white dwarf. As it expands, the envelope cools down and after $\sim$ 1000 days it can be observed as a nebulosity (Hellier, 2001). If the nova shell is spatially resolved, and its expansion speed is measured, the apparent size of the shell can be used to infer the distance to the system (Cohen, 1985).

The relationship between the absolute magnitude at the maximum light and the decline rate of novae was early recognized (Zwicky, 1936; Mclaughlin, 1945). This finding could make nova outbursts an extragalactic distance indicator. However, the increasing observational data pointed out that properties of novae are not uniform, they vary in galaxies and may depend on the underlying stellar populations. Moreover, models studying nova explosions demonstrated that the brightness and decline rate of novae are strongly dependent on the mass of the white dwarf and on the accretion rate (e.g. Shara et al., 1980; Prialnik & Kovetz, 1995). Although in the last decade statistics of nova observations increased rapidly, the consensus is still missing. Therefore CNe can not be used as standard candles.

CVs undergoing multiple nova explosions are called Recurrent Novae (RNe). Their well known representatives are RS Ophiuchi and T Pyxidis which produced nova outbursts four and five times in the last $\sim$ 100 years. Nova evolution models suggest (Prialnik & Kovetz, 1995; Yaron et al., 2005) that RNe with such short recurrence times possess a very massive white dwarf ($M_{WD} \gtrsim 1.3$ $M_\odot$). Since the white dwarf radius decreases as its mass increases (Panei et al., 2000), the nova explosion can be ignited with smaller amount of accreted mass in a massive white dwarf. Obviously, assuming the same accretion rate, a nova explosion recur more often in a CV consisting of a white dwarf star close to the Chandrasekhar mass limit[7].

[5]This term is not entirely correct since at some level magnetic field acts in all CVs – it plays a role in magnetic braking and/or provides the source of viscosity in the accretion disk. Here we use the "non-magnetic" expression to mark those systems in which the white dwarf has weak magnetic field ($B \lesssim 10^5$ G) and the accretion disk extends to the surface of the white dwarf.

[6]Note, that the energy release from Supernovae is significantly larger – it is around 10^{51} ergs.

[7]The expected recurrence time of the nova outburst in an accreting binary system consisting of a 1 $M_\odot$ white dwarf is about 10^5 – 10^6 years (Yaron et al., 2005).

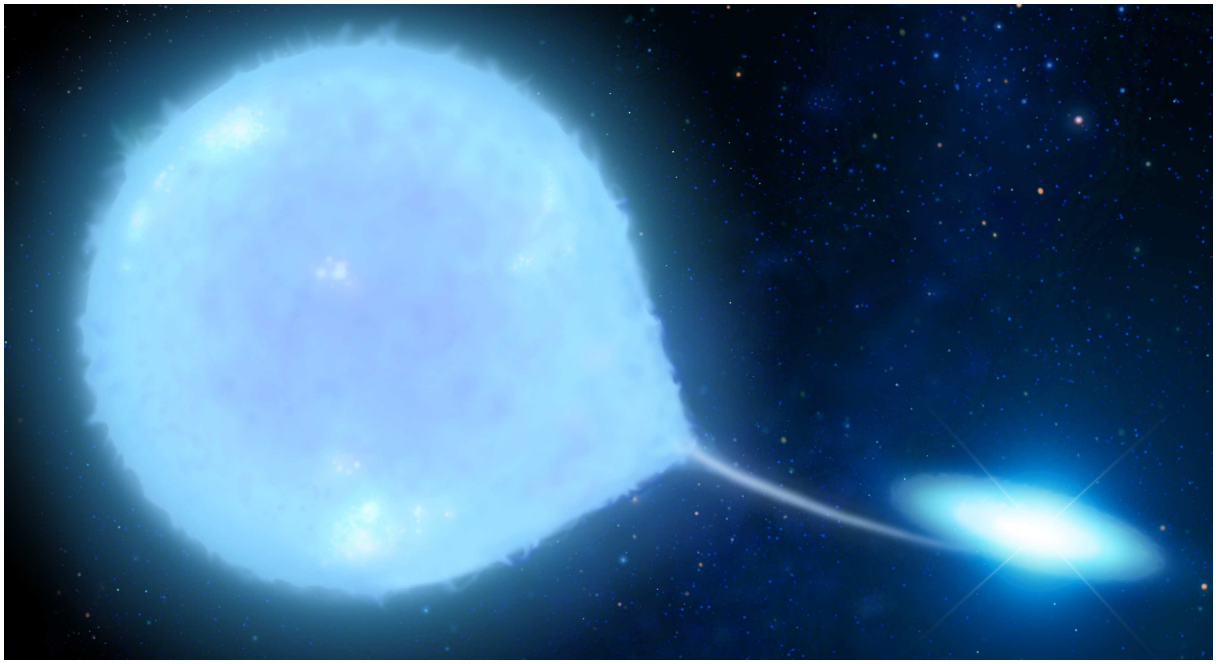

Figure 1.6: Artist's impression of a supersoft X-ray source. Credit: Mark A. Garlick.

Model computations also indicate that RNe expel less material during outbursts than they accrete, hence the white dwarf may increase its mass (Yaron et al., 2005). Eventually it may approach the Chandrasekhar mass limit, leading to a SN Ia.

The class of Nova-like variables include those CVs, which so far did not show an eruption. NLs show very similar spectral properties to CNe which settled back to quiescence, suggesting that these systems are either in the pre-nova or in the post-nova state. In principal, it is only a matter of time to observe a nova explosion in these systems. The mass transfer rate in NLs is rather high, and the system is dominated by a bright accretion disk (Warner, 1995).

In Chapter 4 we study the nature of CN progenitors in details (Bogdán & Gilfanov, 2010b).

Dwarf novae

Dwarf novae (DNe) are characterized by frequent outbursts occurring on a time scale of weeks-months. These outbursts are fainter than CNe, the increase in brightness is in the range of $2-6$ magnitudes.

DN outbursts are caused by disk instability, that was first described by Osaki (1974) in the framework of the disk instability model (DIM)[8]. The standard DIM model assumes a constant mass transfer rate from the secondary star and explains the nova outbursts by thermal-viscous instability. The physical mechanism of the model was studied by Hoshi (1979), who recognized that the disk exhibits bi-stable states: one of them is an optically-thin cool solution with low viscosity where the hydrogen is in neutral state, the other

[8]Another model attempting to explain DN outbursts is the mass transfer instability model (MTI) (Bath, 1975). According to the MTI model the instability and therefore the outburst is caused by an intrinsic instability in the envelope of the secondary star. However, this model is not accepted since it contradicts observations of DNe.

is optically-thick high-viscosity solution where the hydrogen is ionized. More detailed calculations were performed by Meyer & Meyer-Hofmeister (1981), who showed that DN outbursts could be explained by jumps of the accretion disk between these two states. The DIM model is in good agreement with observations of DNe concerning the time scales of DN outbursts, their energetics, and the observed accretion rates.

Supersoft X-ray sources

Supersoft X-ray sources (illustrated in Figure 1.6) are a subclass of bright X-ray sources, exhibiting very soft spectra ($kT \sim 30 - 40$ eV) and high luminosity ($\sim 10^{38}$ erg s^{-1}). The first supersoft sources were detected in the Large Magellanic Cloud (LMC) by *Einstein Observatory*, however their different nature from other X-ray sources was demonstrated only based on *ROSAT* observations (Trümper et al., 1991).

The nature of supersoft sources was unclear at the time of their discovery, they were suggested to be black holes in binary systems (e.g. Smale et al., 1988; Cowley et al., 1990). It was realized by van den Heuvel et al. (1992) that their emission properties and the high luminosities can be explained by a white dwarf, which burns steadily the accreted matter. In order to fulfill the condition of steady hydrogen fusion, an accretion rate of $\sim 10^{-7}$ M$_\odot$/yr is needed, hence the accreted hydrogen is converted at the same rate to helium, and depending on the conditions, further to carbon and oxygen.

Because these systems do not initiate nova explosions, their mass can grow towards the Chandrasekhar mass limit. Therefore, supersoft X-ray sources are considered as a likely path leading to SNe Ia as discussed in Section 1.1.3.

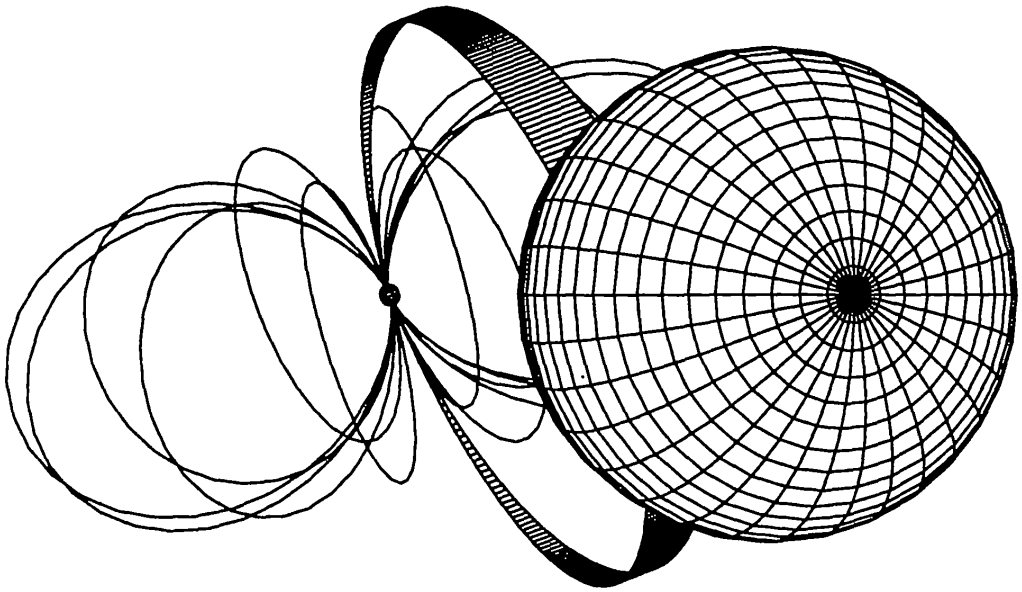

Figure 1.7: Illustration of the polar AR Ursae Majoris (Schmidt, 1999). The accretion stream from the secondary star follows the magnetic field lines towards the white dwarf and it is accreted onto its magnetic poles.

Magnetic systems

Magnetic CVs contain a strongly magnetized white dwarf. Depending on the strength of the magnetic field, two subclasses exist: polars (AM Her systems) with a magnetic field of $\sim 10 - 200$ MG and intermediate polars (IPs) with $\sim 1 - 10$ MG field strength. In polars, the accretion disk is fully disrupted by the strong magnetic field, but in IPs due to the weaker field only the inner parts of the accretion disk are truncated.

In polars the accreted material forms an accretion stream and follows magnetic field lines towards the magnetic poles of the white dwarfs (Figure 1.7). In IPs the matter is transferred through an accretion disk at large distances from the white dwarf, but follows the magnetic field lines from the point, where the disk is truncated. As a result, the transferred matter freely falls onto the white dwarf surface, and forms a strong shock near to its surface (Aizu, 1973). This post-shock region is heated up to high temperatures, typically to $\sim 10 - 20$ keV, and emits X-rays via optically-thin thermal bremsstrahlung emission (Lamb & Masters, 1979). The region around magnetic poles is heated by the emitted hard X-ray radiation, and after thermalization it is reradiated in soft X-ray and extreme ultraviolet wavelengths. According to theoretical predictions the ratio between the soft reprocessed and the hard X-ray luminosity is $L_{soft}/L_{hard} \sim 0.5$ (King & Lasota, 1979), being broadly consistent with observational studies (Ramsay & Cropper, 2004).

1.2.3 Hot gas content of normal galaxies

The presence of hot gas in normal elliptical galaxies was reported by Forman et al. (1979) in a survey of the Virgo cluster using the *Einstein Observatory*. They pointed out that the observed asymmetry of X-ray isophotes, compared to the optical image of M86, is caused by ram pressure stripping by the intracluster medium, indicating the gaseous nature of the extended emission. The increasing sensitivity and angular resolution of next generation X-ray telescopes allowed to study the hot ionized gas content of galaxies in further details.

Observations shed light on the correlation between the observed X-ray luminosity (L_X) and the B-band luminosity (L_B) of early-type galaxies (Canizares et al., 1987). Investigations by O'Sullivan et al. (2001) indicated that in less massive elliptical galaxies $L_X \propto L_B$, whereas in more massive ones $L_X \propto L_B^2$, and the separation in B-band luminosity is at $\sim 3 \cdot 10^{10}$ $L_{B,\odot}$. The X-ray emission in less massive galaxies is dominated by LMXBs, which are distributed according to the stellar light (Gilfanov, 2004). In massive galaxies the change in the ($L_X - L_B$) dependence indicates the presence of an additional X-ray emitting component with non-stellar origin. This component, dominating the observed X-ray emission, originates from hot ionized gas with a temperature typically below $kT \lesssim 1$ keV. The relation of X-ray luminosity versus optical luminosity for a broad sample of early-type galaxies is shown in Figure 1.8.

The hot ionized gas, observable at X-ray wavelengths, could be either produced within the galaxy or it could originate from inflows to the galaxy. The internal sources of gas are evolved stars which continuously eject material via stellar wind. The temperature of stellar ejecta is $\sim 10^4$ K, therefore the gas needs to be heated to the observed temperatures. This can happen during the star passes through shocks, and SNe Ia also contribute to its heating. Whether external sources are also involved depends on the evolutionary stage of the galaxy. At $z = 0$ the gravitational potential of massive ellipticals is deep enough to keep the gas

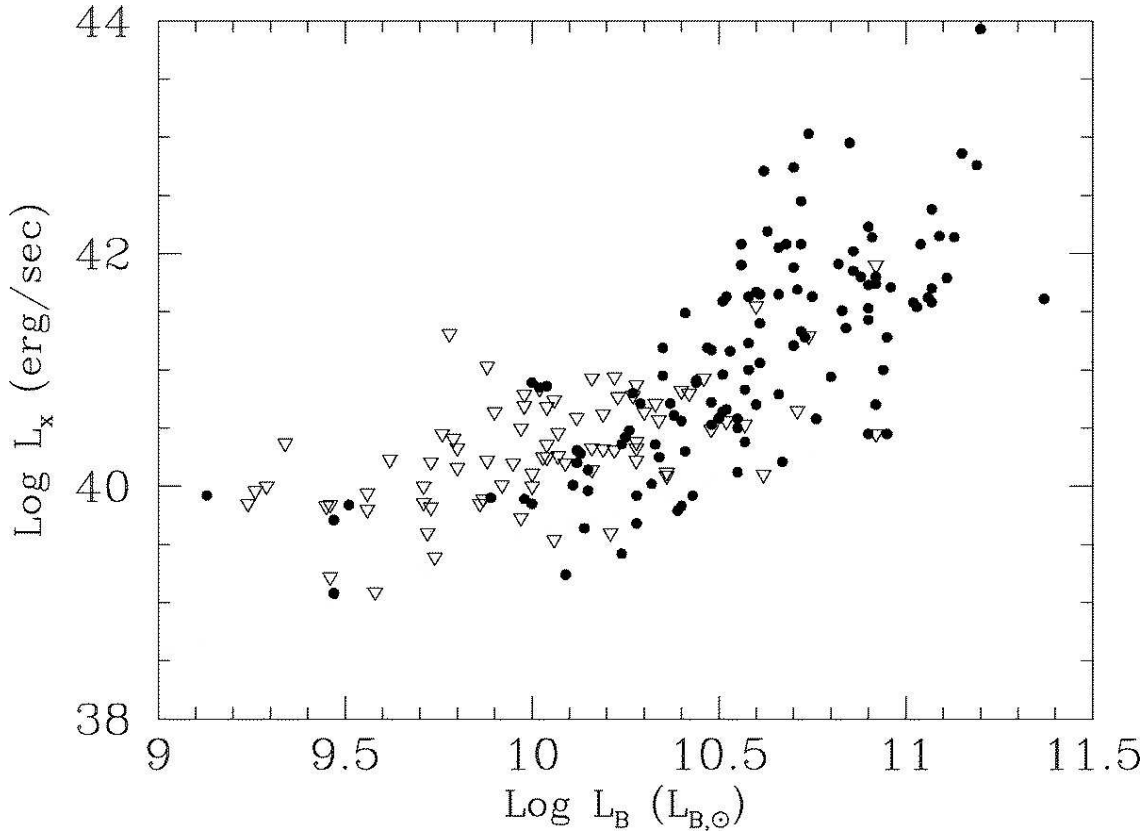

Figure 1.8: Bolometric X-ray luminosity (L_X) versus B-band luminosity (L_B) for a large sample of elliptical galaxies taken from Mathews & Brighenti (2003) based on the compilation of O'Sullivan et al. (2001).

trapped, however in early phases of galaxies very frequent Type II Supernovae could drive galactic winds enriching their local environment. Ciotti et al. (1991) demonstrated that at a later evolutionary state an inflow may evolve and a fraction of the local gas is transferred back into the galaxy providing an external source of gas. The authors explain the large scatter in the ($L_X - L_B$) plot (Figure 1.8) with the different evolutionary phases of galaxies: transition is occurring between the outflow and the inflow. The outflow implies a low L_X/L_B ratio, whereas an inflow has a high L_X/L_B ratio.

Since the binding energy per unit mass decreases with the mass of the galaxy, in less massive ellipticals the interstellar gas is less bound to the galaxy (Faber et al., 1997). Therefore, in principle, SNe Ia could drive a galactic wind from low-mass ellipticals. Indeed, David et al. (2006) pointed out that the energy input from SNe Ia is sufficient to drive an outflow. Further arguments supporting the presence of outflow is the long cooling time[9] of the gas, being much longer than the mass replenishment time by evolved stars. However, to detect such an outflow the various X-ray emitting components have to be separated from the diffuse gas emission. The population of bright X-ray binaries has to be removed, in which *Chandra* observatory has an outstanding role with its superior angular resolution. Moreover, it was revealed recently that fraction of the extended X-ray emission is associated with the stellar population and is the

[9]Note, that the cooling time of the gas is typically $\sim 10^9$ years, significantly shorter than the lifetime of the galaxy.

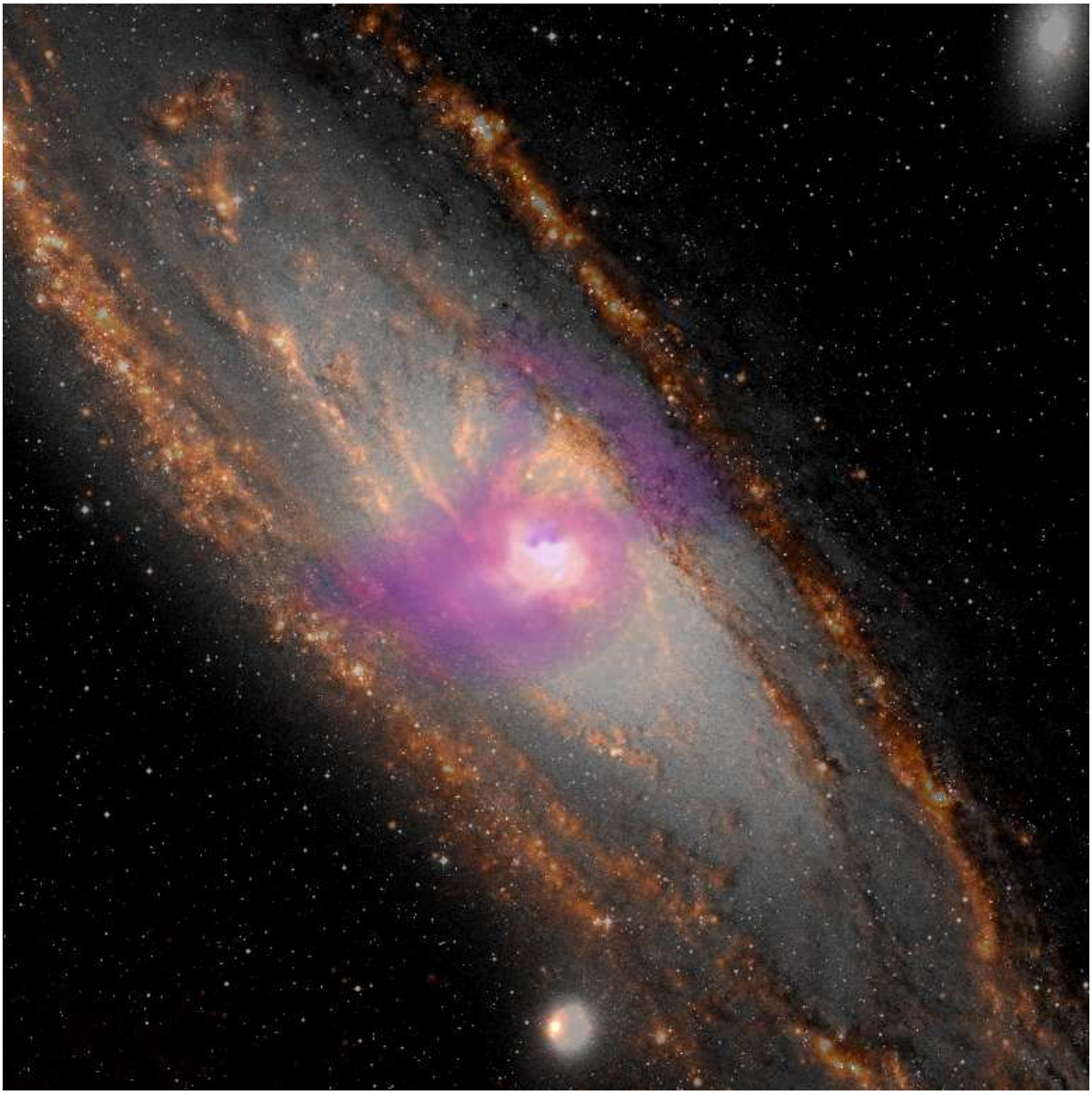

Figure 1.9: Composite image of M31 based on multi-wavelength data. The DSS optical image (grey) represents the distribution of the stellar light, while the 24 micron data of Spitzer Space Telescope (red) traces the distribution of cold gas and dust in spiral arms and in the 10-kpc star-forming ring. Shown in purple is the soft X-ray emission from warm ionized gas which appears to be outflowing from the galaxy.

superposition of a multitude of faint compact sources, mainly accreting white dwarfs and stars with active stellar coronae (Revnivtsev et al., 2006; Sazonov et al., 2006). The typical luminosity of these faint objects is in the range of $10^{27} - 10^{35}$ erg s^{-1}, hence these sources remain unresolved at extragalactic distances.

In Chapter 5 we describe the detection of a galactic wind from the bulge of M31 (Bogdán & Gilfanov, 2008), shown in Figure 1.9.

Figure 1.10: Artist's impression of *Chandra X-ray Observatory*. Credit: Chandra X-ray Center.

1.3 X-ray telescopes

1.3.1 Chandra

Most of the results presented in this work rely on data from *Chandra X-ray Observatory* (Weisskopf et al., 2000), one of NASA's "Great Observatories" (Figure 1.10). The satellite was launched on July 23rd, 1999 from the Kennedy Space Center in Cape Canaveral, aboard the Space Shuttle Columbia as part of STS-93. The satellite was named in honor of the Indian-American Nobel laureate, Subrahmanyan Chandrasekhar, one the most prominent astrophysicists of the 20th century. *Chandra*[10] is the most advanced X-ray telescope built to date.

The satellite has a strongly eccentric orbit, its apogee is ~ 140000 km and its perigee is 10000 km. As a consequence, *Chandra* is in most of the time out of the Earth's radiation belts, allowing to proceed continuous observations for over 100 ks. Therefore it is highly efficient and actively observes during ~ 70 per cent of the time.

Chandra is designed to be a general-purpose X-ray observatory capable to observe photons in the 0.3 – 8 keV energy range. Due to the fact that it has a superior sub-arcsecond angular resolution, its specific focus is high-resolution imaging. The High Resolution Mirror Assembly (HRMA) consists of four pairs of nested Wolter type-I mirrors, the focal length is 10.07 m. The effective area of the HRMA is 800 cm^2 at 0.25 keV, 400 cm^2 at 5 keV, and 100 cm^2 at 8 keV. *Chandra* combines the mirrors with four science instruments: (i) the Advanced CCD Imaging Spectrometer (ACIS) (Garmire et al., 2003), (ii) the High Resolution Camera (HRC) (Murray et al., 2000), (iii) the High Energy Transmission Grating (HETG) (Canizares et al., 2000), and (iv) the Low Energy Transmission Grating (LETG) (Predehl et al.,

[10]The meaning of the word "chandra" is "moon" in Sanskrit.

2000).

The ACIS detector is the most often used among the available instruments. It consists of ten CCDs, eight of them are front-illuminated (FI) and two of them are back-illuminated (BI). The gate structure is mounted facing the mirrors on the FI CCDs, and reverted facing on the BI CCDs. Since no X-ray photons are lost in the gate structure, the BI CCDs have larger effective area at low energies, however their background is also higher. The spectral resolution of FI CCDs is better, however in early stages of the satellite they were damaged by the radiation belts of the Earth, yielding a varying spectral resolution on these CCDs. The set of ACIS CCDs can be arranged in two patterns: either a 2×2 array is used with a 17×17 arcminutes field of view (ACIS-I), or a 1×6 array with 8.5×51 arcminutes field of view (ACIS-S). The pixel size of ACIS CCDs is 0.492 arcsecond.

The HRC is built up from two microchannel plate detectors. It is primarily designed for imaging, has a large 30×30 arcminutes field of view, but these detectors have essentially no energy resolution. The pixel size is smaller than on ACIS detectors and they have also better timing properties.

The two grating assemblies, HETG and LETG, onboard *Chandra* were designed to be used with ACIS-S detectors. The HETG is built up from two different gratings, from the High Energy Grating and from the Medium Energy Grating, they cover the spectral range of $1.2 - 15$ Å and $2.5 - 31$ Å, respectively. The LETG operates in the range of $1.2 - 175$ Å. The spectral resolution of these instruments is excellent, however this applies only within the range of few arcsecond of the source – the energy resolution decreases quickly. The primary use of the grating instruments is the study of bright point sources.

1.3.2 XMM-Newton

In this dissertation we also analyzed data of the *X-ray Multi-Mirror Mission* (*XMM-Newton*). The satellite was launched on December 10th, 1999. It is ESA's second of the four "cornerstone missions" defined by the Horizon 2000 Science Programme. *XMM-Newton* consists of three Wolter type-I mirrors and also a 30 cm UV/optical telescope. The mirrors are efficient in the energy range of $0.1 - 10$ keV, and their main advantage is their large effective area. For each mirror the effective area is 1500 cm^2 at 1.5 keV, 900 cm^2 at 7 keV, and 350 cm^2 at 10 keV, significantly exceeding values for *Chandra* (Figure 1.11). The three instruments onboard *XMM-Newton* are (i) the European Photon Imaging Camera (EPIC) (Strüder et al., 2001; Turner et al., 2001), (ii) the Reflection Grating Spectrometer (RGS) (den Herder et al., 2001), and (iii) the Optical Monitor (OM).

Two of the three EPIC CCD cameras are Metal Oxide Semi-conductor (MOS) CCD arrays. These are mounted behind the X-ray mirrors and have at their foci Reflection Grating Arrays (RGAs), which divert about half of the incoming X-ray light towards the RGSs. The third X-ray telescope focuses its unobstructed beam towards the EPIC PN instrument. The MOS and PN CCDs are used for imaging with large, 30×30 arcminutes field of view. The MOS detector is built up from seven FI CCDs each of them covering 10.9×10.9 arcminutes, while the PN detector consists of twelve CCDs, they cover 13.6×4.4 arcminutes. The pixel size is 1.1 arcsecond and 4.1 arcsecond for MOS and PN detectors, respectively. The spectral resolution of the EPIC CCDs is moderate $E/\Delta E \sim 20 - 50$ and the on-axis point-spread-function with a full-width-half maximum is 6 arcsecond.

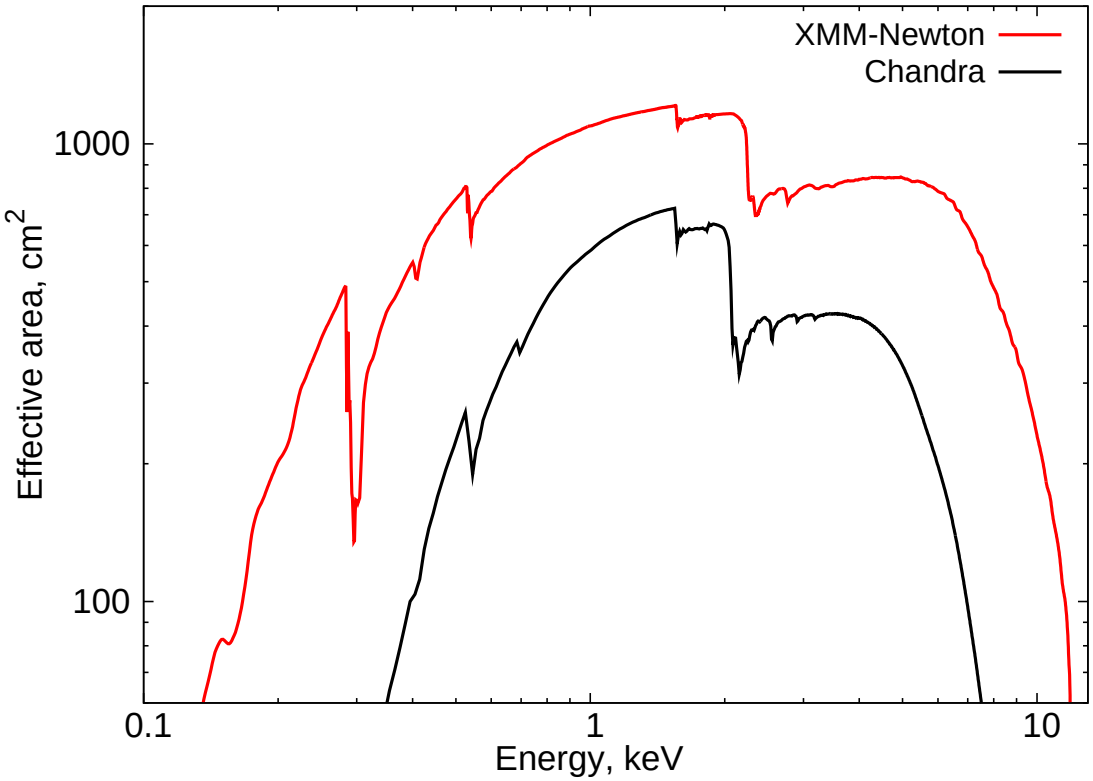

Figure 1.11: Comparison of the effective area of *XMM-Newton* (EPIC PN detector) and *Chandra* (BI detector).

The RGS have an outstanding resolving power of $E/\Delta E \sim 150 - 800$. However, the fact that this spectral resolution can be achieved only in the cross-dispersion direction strongly limits its use.

The OM covers the wavelength range of $170 - 650$ nm and it makes an image of the central 17×17 arcminute region of the X-ray field of view. The telescope is a modified Ritchey-Chretien design, with focal length of 3.8 meters and focal ratio of f/12.7. The OM offers the possibility to monitor the sky in X-rays and in UV wavelengths simultaneously.

1.4 Outline

This dissertation consists of the results of four studies. In Chapter 2 we study the progenitor scenarios of SNe Ia in early-type galaxies and constrain the contribution of the single-degenerate scenario to the observed SN Ia rate. The results of this work are accepted for publication in *Nature* (Gilfanov & Bogdán, 2010). In an accompanying work, presented in Chapter 3, we place upper limits on the combined X-ray emission from the population of steady nuclear burning white dwarfs. In the framework of the single-degenerate scenario these systems are believed to be likely progenitors of SNe Ia. This work is accepted for publication in *Astronomy & Astrophysics* (Bogdán & Gilfanov, 2010a). We derive constraints on the nature of CN progenitors in Chapter 4, in particular we study the contribution of magnetic systems to the observed CN rate and place upper limits on the fraction of accreted mass in dwarf novae during quies-

cence. In this Chapter we also investigate the origin of unresolved emission from M31 based on *Chandra* and *XMM-Newton* data, and study the X-ray to star-formation rate ratio along the 10-kpc star-forming ring of the galaxy. This study will be submitted to *Monthly Notices of the Royal Astronomical Society* (Bogdán & Gilfanov, 2010b). In Chapter 5 we investigate the origin and properties of the unresolved X-ray emission from the bulge of M31, and report about the detection of a hot gas outflow. These results are published in *Monthly Notices of the Royal Astronomical Society* (Bogdán & Gilfanov, 2008). In Chapter 6 we summarize our results.

Bibliography

Aizu, K., 1973, PThPh, 49, 1184

Astier, P., Guy, J., Regnault, N., et al., 2006, A&A, 447, 31

Baade, W.; Zwicky, F., 1934, PNAS, 20, 254

Badenes, C., Hughes, J. P., Bravo, E. & Langer, N., 2007, ApJ, 662, 472

Bath, G. T., 1975, MNRAS, 171, 311

Branch, D., Livio, M., Yungelson, L. R., Boffi, F. R. & Baron, E., 1995, PASP, 107, 1019

Bogdán, Á., Gilfanov, M., 2008, MNRAS, 388, 56

Bogdán, Á., Gilfanov, M., 2010a, A&A, in press

Bogdán, Á., Gilfanov, M., 2010b, MNRAS, in press

Caldwell, R. R., Dave, R. & Steinhardt, P. J., 1998, PhRvL, 80, 1582

Canizares, C. R.; Fabbiano, G. & Trinchieri, G., 1987, ApJ, 312, 503

Canizares, C. R., Huenemoerder, D. P., Davis, D. S., et al., 2000, ApJ, 539, 41

Ciotti, L., D'Ercole, A., Pellegrini, S. & Renzini, A., 1991, ApJ, 376, 380

Cohen, J. G., 1985, ApJ, 292, 90

Cole, S., Percival, W. J., Peacock, J. A., et al., 2005, MNRAS, 362, 505

Cowley, A. P., Schmidtke, P. C., Crampton, D. & Hutchings, J. B., et al., 1990, ApJ, 350, 288

David, L. P., Jones, C., Forman, W., et al., 2006, 653, 207

den Herder, J. W., Brinkman, A. C., Kahn, S. M., et al., 2001, A&A, 365, 7

Eisenstein, D. J., Zehavi, I., Hogg, D. W., et al., 2005, ApJ, 633, 560

Eggleton, P. P., 1983, ApJ, 268, 368

Evans, P. A. & Hellier, C., 2007, MNRAS, 663, 1277

Fabbiano, G. 2006, ARA&A, 44, 323

Faber, S. M., Tremaine, S., Ajhar, E. A., et al., 1997, AJ, 114, 1771

Fink, M., Hillebrandt, W. & Röpke, F. K., 2007, A&A, 476, 1133

Forman, W., Schwarz, J., Jones, C., Liller, W. & Fabian, A. C., 1979, ApJ, 234, 27

Fujimoto, M. Y., 1982, ApJ, 257, 752

Garmire, G. P., Bautz, M. W., Ford, P. G., Nousek, J. A. & Ricker, G. R. Jr., 2003, SPIE, 4851, 28

Giacconi, R., Branduardi, G., Briel, U., et al., 1979, ApJ, 230, 540

Gilfanov, M. 2004, MNRAS, 349, 146

Gilfanov, M. & Bogdán, Á. 2010, Nature, 463, 924

Greiner, J., Hasinger, G. & Kahabka, P., 1991, A&A, 246, 17

Haberl, F. & Motch, C., 1995, A&A, 297, 37

Hachisu, I., Kato, M. & Nomoto, K., 1996, ApJ, 470, 97

Hachisu, I., Kato, M., Nomoto, K., 1999, ApJ, 522, 487

Hamuy, M., Phillips, M. M., Suntzeff, N. B., Schommer, R. A., Maza, J. & Aviles, R., 1996, AJ, 112, 2391

Hamuy, M.; Phillips, M. M.; Suntzeff, N. B., et al., 1996, AJ, 112, 2408

Hartwig, E., 1898, AN, 148, 11

Hellier, C., 2001, Cataclysmic Variable Stars, Springer

Höflich, P. & Khokhlov, A. 1996, ApJ, 457, 500

Homeier, D., Koester, D., Hagen, H.-J., Jordan, S., Heber, U., Engels, D., Reimers, D. & Dreizler, S., 1998, A&A, 338, 563

Hoshi, R., 1979, PThPh, 61, 1307

Iben, I., Jr. & Tutukov, A. V., ApJS, 54, 335

Iben, I., Jr. & Tutukov, A. V., 1985, ApJS, 58, 661

Iwamoto, K., Mazzali, P. A., Nomoto, K., et al., 1998, Nature, 395, 672

Kahabka, P. & van den Heuvel, E. P. J., 1997, ARA&A, 35, 69

King, A. R. & Lasota, J. P., 1979, MNRAS, 188, 653

King, A. R. & Lasota, J. P., 1990, MNRAS, 247, 214

Lamb, D. Q. & Masters, A. R., 1979, ApJ, 234, 117

Livio, M. 2000, Type Ia Supernovae, Theory and Cosmology. Eds.: J. C. Niemeyer and J. W. Truran, Cambridge University Press, 2000, 33

Lundmark, K., 1921, PASP, 33, 225

Mathews, W. G. & Brighenti, F., 2003, ARA&A, 41, 191

Mclaughlin, D. B., 1945, PASP, 57, 69

Meyer, F. & Meyer-Hofmeister, E., 1981, A&A, 104, 10

Minkowski, R., 1941, PASP, 53, 224

Murray, S. S., Chappell, J. H., Kenter, A. T., et al., 2000, SPIE, 4140, 144

Nomoto, K. & Sugimoto, D., 1977, PASJ, 29, 765

Nomoto, K., Nariai, K. & Sugimoto, D., 1979, PASJ, 31, 287

Nomoto, K., 1982, ApJ, 253, 798

Nomoto, K. & Iben, I., Jr., 1985, ApJ, 297, 531

Nomoto, K. & Kondo, Y., 1991, ApJ, 367, 19

Nomoto, K., Saio, H., Kato, M. & Hachisu, I., 2007, ApJ, 663, 1269

Nugent, P., Baron, E., Branch, D., Fisher, A. & Hauschildt, P. H. 1997, ApJ, 485, 812

Osaki, Y., 1974, PASJ, 26, 429

O'Sullivan, E., Forbes, D. A., Ponman, T. J., 2001, MNRAS, 328, 461O

Pakmor, R., Kromer, M., Röpke, F. K., Sim, S. A., Ruiter, A. J. & Hillebrandt, W., 2009, arXiv:0911.0926

Panei, J. A., Althaus, L. G. & Benvenuto, O. G. 2000, A&A, 353, 970

Percival, W. J., Baugh, C. M., Bland-Hawthorn, J., et al., 2001, MNRAS, 327, 1297

Perlmutter, S., Gabi, S., Goldhaber, G., et al., 1997, ApJ, 483, 565

Perlmutter, S., Aldering, G., Goldhaber, G., et al., 1999, ApJ, 517, 565

Perlmutter, S. 2003, PhT, 56, 53

Phillips, M. M., 1993, ApJ, 413, 105

Predehl, P., Aschenbach, B., Braeuninger, H., et al, 2000, Atomic Data Needs for X-ray Astronomy, 11

Prialnik, D. & Kovetz, A., 1995, ApJ, 445, 789

Ramsay, G., Mason, K. O., Cropper, M., Watson, M. G. & Clayton, K. L., 1994, MNRAS, 270, 692

Ramsay, G. & Cropper, M., 2004, MNRAS, 347, 497

Revnivtsev, M., Sazonov, S., Gilfanov, M., Churazov, E. & Sunyaev, R., 2006, A&A, 452, 169

Riess, A. G., Press, W. H. & Kirshner, R. P., 1996, ApJ, 473, 88

Riess, A. G., Filippenko, A. V., Challis, P., et al., 1998, AJ, 116, 1009

Riess, A. G., Kirshner, R. P., Schmidt, B. P., et al., 1999, AJ, 117, 707

Riess, A. G., Strolger, L.-G., Tonry, J., et al, 2004, ApJ, 607, 665

Ritter, H. & Kolb, U., 2003, A&A, 404, 301

Saio, H. & Nomoto, K., 1985, A&A, 150, 21

Saio, H. & Nomoto, K., 1998, ApJ, 500, 388

Sazonov, S., Revnivtsev, M., Gilfanov, M., Churazov, E. & Sunyaev, R., 2006, A&A, 450, 117

Schmidt, G. D., 1999, ASPC, 157, 207

Shakura, N. I. & Sunyaev, R. A., 1973, A&A, 24, 337

Shara, M. M., Prialnik, D. & Shaviv, G., 1980, ApJ, 239, 586

Smale, A. P., Corbet, R. H. D., Charles, P. A., et al., 1988, MNRAS, 233, 51

Spergel, D. N., Verde, L., Peiris, H. V., et al., 2003, ApJS, 148, 175

Strüder, L., Briel, U., Dennerl, K., et al. 2001, A&A, 365, L18

Taam, R. E., Sandquist, E. L., 2000, ARA&A, 38, 113

Trümper, J., Hasinger, G., Aschenbach, B., et al., 1991, Natur, 349, 579

Turatto, M., 2003, LNP, 598, 21

Turner, M. J. L., Abbey, A., Arnaud, M., et al. 2001, A&A, 365, L27

Vaiana, G. S., Cassinelli, J. P., Fabbiano, G., et al., 1981, ApJ, 245, 163

van den Heuvel, E. P. J., Bhattacharya, D., Nomoto, K. & Rappaport, S. A., 1992, A&A, 262, 97

Vikhlinin, A., Kravtsov, A. V., Burenin, R. A, et al., 2009, ApJ, 692, 1060

Warner, B., 1995, Cataclysmic variable stars, Cambridge Astrophysics Series, Cambridge, New York: Cambridge University Press

Webbink, R. F., ApJ, 277, 355

Weidemann, V., 2000, A&A, 363, 647

Weisskopf, M. C., Tananbaum, H. D., Van Speybroeck, L. P. & O'Dell, S. L., 2000, SPIE, 4012, 2

Whelan, J. & Iben, I. Jr. 1973, ApJ, 186, 1007

Wood-Vasey, W. M., Miknaitis, G., Stubbs, C. W., et al., 2007, ApJ, 666, 694

Woosley, S. E. & Weaver, T. A., 1986, ARA&A, 24, 205

Yaron, O., Prialnik, D., Shara, M. M. & Kovetz, A., 2005, ApJ, 623, 398

Yungelson, L., Livio, M., Tutukov, A. & Kenyon, S. J., 1995, ApJ, 447, 656

Yungelson, L., Livio, M., Truran, J. W., Tutukov, A. & Fedorova, A., 1996, ApJ, 466, 890

Zwicky, F., 1936, PASP, 49, 191

Zwicky, F., 1939, PhRv, 55, 726

Chapter 2

Chandra unveils progenitors of Type Ia Supernovae in early-type galaxies

Nature, 463, 924, 2010

Gilfanov, M. & Bogdán, Á.

2.1 Abstract

There is wide agreement that Type Ia Supernova (used as standard candles for cosmology) are associated with the thermonuclear explosions of white dwarf stars (Hillebrandt & Niemeyer, 2000; Livio, 2000). The nuclear runaway that leads to the explosion could start in a white dwarf gradually accumulating matter from a companion star until it reaches the Chandrasekhar mass limit (Whelan & Iben, 1973), or could be triggered by the merger of two white dwarfs in a compact binary system (Iben & Tutukov, 1984; Webbink, 1984). The X-ray signatures of these two possible paths are very different. Whereas no strong electromagnetic emission is expected in the merger scenario until shortly before the Supernova, the white dwarf accreting material from the normal star becomes a source of copious X-rays for about 10^7 years before the explosion. This offers a means to determine which path dominates. Here we report that the observed X-ray flux from six nearby elliptical galaxies and galaxy bulges is a factor of $\sim 30 - 50$ less than predicted in the accretion scenario, based upon an estimate of the Supernova rate from their K-band luminosities. We conclude that no more than about 5 per cent of Type Ia Supernovae in early-type galaxies can be produced by white dwarfs in accreting binary systems, unless their progenitors are much younger than the bulk of the stellar population in these galaxies, or explosions of sub-Chandrasekhar white dwarfs make a significant contribution to the Supernova rate.

2.2 Introduction

The maximum possible mass of a carbon-oxygen white dwarf formed through standard stellar evolution can not not exceed $\approx 1.1 - 1.2 M_\odot$ (Weidemann, 2000). Although the nuclear detonation can start below the Chandrasekhar mass ($\approx 1.38 M_\odot$), sub-Chandrasekhar models have so far failed to reproduce observed properties of SNe Ia (Höflich & Khokhlov, 1996; Nugent et al., 1997), despite continuing effort (Fink et al., 2007). Thus the white dwarf needs to accrete $\Delta M \gtrsim 0.2 M_\odot$ of matter before the Supernova explosion happens. As accreted material accumulates on the white dwarf surface, hydrogen shell burning is ignited, converting hydrogen to helium and, possibly, further to carbon and oxygen. Depending on the mass accretion rate $\dot{M}$, it may proceed either in a (quasi-)steady regime or explosively, giving rise to Classical Nova events (Nomoto et al., 2007). Because mass is lost in Nova outbursts,Yaron et al. (2005) the white dwarf does not grow if nuclear burning is unstable. For this reason the steady burning regime is strongly preferred by the accretion scenario (Livio, 2000), limiting the range of the mass accretion rate relevant to the problem of SN Ia progenitors to $\dot{M} \gtrsim 10^{-7}\ M_\odot$/yr. In this regime energy of hydrogen fusion is released in the form of electromagnetic radiation, with luminosity of $L_{WD,nuc} = \epsilon_H X \dot{M} \sim 10^{37}$ erg/s, where $\epsilon_H \approx 6 \cdot 10^{18}$ erg/g is energy release per unit mass and X – hydrogen mass fraction (the solar value of $X = 0.72$ is assumed). The nuclear luminosity exceeds by more than an order of magnitude the gravitational energy of accretion and maintains the effective temperature of the white dwarf surface at the level (defined by the Stefan-Boltzmann law):

$$T_{\rm eff} \approx 45\ (\dot{M}/10^{-7} M_\odot/yr)^{1/4} (R_{\rm WD}/10^{-2} R_\odot)^{-1/2}\ {\rm eV}. \tag{2.1}$$

The blackbody spectrum of this temperature peaks in the soft X-ray band and, therefore, is prone to absorption by interstellar gas and dust, especially at the lower end of the temperature range. Because the white dwarf radius $R_{\rm WD}$ decreases with its mass (Panei et al., 2000), the $T_{\rm eff}$ increases as the white dwarf approaches the Chandrasekhar limit – the signal, detectable at X-ray wavelengths, will be dominated by the most massive white dwarfs. Such sources are indeed observed in the Milky Way and nearby galaxies and are known as supersoft sources (Kahabka & van den Heuvel, 1997).

2.3 Predicted X-ray luminosity from accreting white dwarfs

The Type Ia Supernova rate scales with stellar mass and, hence, with near-infrared luminosity of the host galaxy (Mannucci et al., 2005). The scale factor is calibrated through extensive observations of nearby galaxies and for E/S0 galaxies equals (Mannucci et al., 2005), $\dot{N}_{\rm SNIa}/L_K \approx 3.5 \cdot 10^{-4}$ yr^{-1} per $10^{10}\ L_{K,\odot}$, corresponding to one Supernova in a few hundred years for a typical galaxy. If the white dwarf mass increases at a rate $\dot{M}$, a population of

$$N_{\rm WD} \sim \frac{\Delta M}{\dot{M}\,\langle \Delta t \rangle} \sim \frac{\Delta M}{\dot{M}} \dot{N}_{\rm SNIa} \tag{2.2}$$

accreting white dwarfs is needed in order for one Supernova to explode on average every $\langle \Delta t \rangle = \dot{N}^{-1}_{\rm SNIa}$ years. With $\dot{M} \sim 10^{-7} - 10^{-6}\ M_\odot$/yr, for a typical galaxy, $N_{\rm WD}$ is a few hundreds or thousands – the

Table 2.1: Comparison of the accretion scenario with observations. Listed for each galaxy are: name, K-band luminosity, number of accreting white dwarfs and X-ray luminosities in the soft (0.3–0.7 keV) band. The statistical errors for observed X-ray luminosities range from 20 per cent (NGC 3377) to less than 7 per cent. The columns marked "predicted" display total number and combined X-ray luminosity (absorption applied) of accreting white dwarfs in the galaxy predicted in case the single degenerate scenario would produce all SNe Ia. They were computed assuming $\dot{M} = 10^{-7}\ M_{\odot}$/yr and initial white dwarf mass of $1.2 M_{\odot}$. The $N_{\rm WD}$ drops by a factor of 10 for $\dot{M} = 10^{-6}\ M_{\odot}$/yr.

Name	L_K [$L_{K,\odot}$]	$N_{\rm WD}$	L_X [erg/s]	
	observed	predicted	observed	predicted
M32	$8.5 \cdot 10^8$	25	$1.5 \cdot 10^{36}$	$7.1 \cdot 10^{37}$
NGC3377	$2.0 \cdot 10^{10}$	$5.8 \cdot 10^2$	$4.7 \cdot 10^{37}$	$2.7 \cdot 10^{39}$
M31 bulge	$3.7 \cdot 10^{10}$	$1.1 \cdot 10^3$	$6.3 \cdot 10^{37}$	$2.3 \cdot 10^{39}$
M105	$4.1 \cdot 10^{10}$	$1.2 \cdot 10^3$	$8.3 \cdot 10^{37}$	$5.5 \cdot 10^{39}$
NGC4278	$5.5 \cdot 10^{10}$	$1.6 \cdot 10^3$	$1.5 \cdot 10^{38}$	$7.6 \cdot 10^{40}$
NGC3585	$1.5 \cdot 10^{11}$	$4.4 \cdot 10^3$	$3.8 \cdot 10^{38}$	$1.4 \cdot 10^{40}$

accretion scenario predicts a numerous population of accreting white dwarfs. The brightest and hottest of them may reveal themselves as supersoft sources (Di Stefano et al., 2004), but the vast majority must remain unresolved or hidden from the observer, for example by interstellar absorption. The combined luminosity of this "sea" of accreting white dwarfs is

$$L_{tot,nuc} = L_{WD,nuc} \times N_{\rm WD} = \epsilon X \Delta M \dot{N}_{\rm SNIa} \tag{2.3}$$

where ΔM is the difference between the Chandrasekhar mass and the initial white dwarf mass. Unlike the number of sources, the luminosity allows an accurate account for absorption and bolometric corrections and therefore a quantitative comparison with observations can be made.

2.4 Observed X-ray luminosity from accreting white dwarfs

To this end we collected archival data of X-ray (Chandra) and near-infrared (Spitzer and 2MASS) observations of several nearby gas-poor elliptical galaxies and for the bulge of M31 (Table 2.1). Using K-band measurements to predict the SN Ia rates, we computed combined X-ray luminosities of SN Ia progenitors, based on a conservative, but plausible choice of parameters: $\dot{M} = 10^{-7} M_{\odot}$/yr and initial white dwarf mass of 1.2 $M_{\odot}$. The SN Ia rate was reduced by a half in order to account for the fact that galaxies in our test-sample are somewhat older (Terlevich & Forbes, 2002) than those used to derive the rate (Gallagher et al., 2008). In computing the spectral energy distribution we took into account the dependence of the effective temperature on the white dwarf mass as described by equation (2.1), and the effect of the interstellar absorption (which does not exceed a factor of $\sim 3-4$). The observed X-ray luminosities were not corrected for absorption and include unresolved emission and emission from

resolved compact sources with hardness ratio corresponding to $kT_{bb} \leq 200$ eV. The contribution of warm ISM was subtracted, when possible. Obviously, the observed values present upper limits on the luminosity of the hypothetical population of accreting white dwarf, as there may be other types of X-ray sources contributing to the observed emission. As is clear from the Table 2.1, predicted luminosities surpass observed ones by a factor of $\sim 30 - 50$ demonstrating that the accretion scenario is inconsistent with observations by a large margin.

2.5 High accretion rate scenarios

There exists a maximum rate at which hydrogen can burn on the white dwarf surface, $\dot{M}_{RG} \sim 10^{-6} M_{\odot}/\mathrm{yr}$ (Nomoto et al., 2007). The excess material may leave the system in the form of a radiation driven wind (Hachisu et al., 1996) or may form a common envelope configuration (Nomoto et al., 1979; Livio, 2000). In both cases, because of the large photospheric radius, $\sim 10^2 - 10^3$ $\mathrm{R}_{\odot}$, the peak of the radiation is in the UV part of the spectrum and emission from such an object will be virtually undetectable, owing to interstellar absorption and dilution with the stellar light. However, there is a nearly universal consensus (Livio, 2000) that the common envelope configuration does not lead to the SN Ia explosion, producing a double white dwarf binary system instead.

In the wind regime, the white dwarf could grow in mass but it is a rather inefficient process because a significant fraction of the transferred mass is lost in the wind (Hachisu et al., 1996; Li & van den Heuvel, 1997). Therefore a relatively massive, $M \gtrsim 1.3-1.7 M_{\odot}$, donor star is required for the white dwarf to reach the Chandrasekhar limit. Because the lifetimes of such stars do not exceed $\sim 2 - 5$ Gyrs, they may exist only in the youngest of early-type galaxies, in which no more than $\sim 30 - 40$ per cent of Supernovae are detected (Gallagher et al., 2008). We took this into account in our calculations by halving the canonical value of the SN Ia rate (Mannucci et al., 2005). On a related note, in many elliptical galaxies small sub-populations of young stars are detected (Schawinski, 2009). The ages of SN Ia progenitors are not very well constrained observationally, so it is possible in principle that these progenitors are much younger than the bulk of the stellar population. However, given a small fraction of young sub-populations in elliptical galaxies (a few per cent or less), would imply very high efficiency of young stars in producing Supernovae and SN Ia rates in spiral galaxies, that are too high, much higher than observed (Mannucci et al., 2005). This is therefore not a likely scenario.

2.6 Conclusions

Thus, in early-type galaxies, white dwarfs accreting from a donor star in a binary system and detonating at the Chandrasekhar mass limit do not contribute more than about 5 per cent to the observed SN Ia rate. At present the only viable alternative is the merger of two white dwarfs, so we conclude that SNe Ia in early-type galaxies predominantly arise from the double degenerate scenario. In late-type galaxies, in contrast, massive donor stars are available making the mass budget less prohibitive, so that white dwarfs can grow to the Chandrasekhar mass entirely inside an optically thick wind (Hachisu et al., 1996; Li & van den Heuvel, 1997) or, via accretion of He-rich material from a He-donor star Iben & Tutukov (1994). In addition, a

star-forming environment is usually characterized by large amounts of neutral gas and dust, leading to increased absorption obscuring soft X-ray radiation from accreting white dwarfs. Therefore in late-type galaxies the accretion scenario may play a significant role.

Acknowledgements. We thank F. Meyer and H. Ritter for discussions of various aspects of mass transfer in binary systems and the role of the common envelope evolution and L. Yungelson for discussions on the type Ia supernovae progenitor problem in general. This research has made use of Chandra archival data, provided by the Chandra X-ray Center (CXC) in the application package CIAO. This research has also made use of data products from the Two Micron All Sky Survey, which is a joint project of the University of Massachusetts and the Infrared Processing and Analysis Center/California Institute of Technology, funded by NASA and the NSF. The Spitzer Space telescope is operated by the Jet Propulsion Laboratory, California Institute of Technology, under contract with NASA.

Author Contributions. Both authors contributed equally to this Letter.

2.7 Supplementary information

2.7.1 Unstable and stable nuclear burning

At low values of the mass accretion rate $\dot{M}$ nuclear burning on the white dwarf surface is thermally unstable and proceeds in flashes, the exact boundary depending on the white dwarf mass Nomoto et al. (2007): $\dot{M}_{crit} \approx 3.1 \cdot 10^{-7}\,(M_{\rm WD}/M_\odot - 0.54)$ M$_\odot$/yr. At yet smaller $\dot{M} \lesssim$ few$\times 10^{-8}$ M$_\odot$/yr flashes become dynamical, triggering Classical Nova (CN) outbursts Yaron et al. (2005). These relatively low $\dot{M}$ systems – parent population for CNe, are broadly referred to as cataclysmic variables. The nuclear burning stabilizes at higher $\dot{M}$. In this regime, believed to be the most plausible evolutionary path to SN Ia Livio (2000), an accreting white dwarf reveals itself as a supersoft X-ray source (SSS) powered by the nuclear energy of hydrogen fusion on its surface Greiner (2000). The dichotomy between unstable and stable nuclear burning systems is vividly illustrated by their $\dot{M}$ distributions (Figure 2.1). The remarkably sharp boundary between CNe and SSS is the consequence of the stabilization of nuclear burning at $\log(\dot{M}) \sim -7.5$, in accord with theory.

2.7.2 The single degenerate scenario and statistics of Classical Novae

It is predicted by theory Yaron et al. (2005) and confirmed by observations Shore et al. (2003) that in CN outbursts most of the accreted envelope and some of the original white dwarf material will be lost. For this reason, it is believed that the white dwarf can not grow in mass unless the accretion rate exceeds $\gtrsim$ few $\times\, 10^{-8}\ M_\odot$/yr. Independently from this consideration we present an argument showing that the statistics of CNe predicted in the single-degenerate scenario is inconsistent with the observed CN frequency.

Assuming that cataclysmic variables are the main type of SN Ia progenitors one can relate the CN and SN Ia rates:

$$\Delta M_{acc}\, \dot{N}_{\rm CN} \sim \Delta M_{\rm SN}\, \dot{N}_{\rm SN} \tag{2.4}$$

where ΔM_{acc} is the mass accumulated by the white dwarf per one classical nova outburst cycle, ΔM_{SN} is the mass needed for the white dwarf to reach the Chandrasekhar limit. As these quantities depend on the $\dot{M}$ and white dwarf mass, we write more precisely:

$$\frac{\dot{N}_{\rm CN}}{\dot{N}_{\rm SNIa}} = \int \frac{dM_{\rm WD}}{\Delta M_{acc}(M_{\rm WD}, \dot{M})} \geq \int \frac{dM_{\rm WD}}{\Delta M_{\rm CN}(M_{\rm WD}, \dot{M})} \tag{2.5}$$

where ΔM_{CN} is the mass of the hydrogen shell required for the nova outburst to start Yaron et al. (2005). The inequality in the equation (2.5) follows from the fact that $\Delta M_{acc} \leq \Delta M_{CN}$, due to the possible mass loss during CN outburst Yaron et al. (2005). As the ΔM_{CN} decreases steeply with the white dwarf mass, the main contribution to the predicted CN rate is made by the most massive white dwarfs near the Chandrasekhar limit. They will be producing frequent outbursts with relatively short decay times Yaron et al. (2005), thus resulting in a large population of fast recurrent novae, in apparent contradiction to the statistics of CNe (Figure 2.2). Note that, although short, these outbursts are not fainter than the longer ones Yaron et al. (2005) and could not have been missed in the past Arp (1956) and more recent Capaccioli et al.

(1989) CN surveys of M31.

Based on the statistics of fast CNe (Figure 2.2), the contribution of cataclysmic variables to the SN Ia rate can be constrained. The observed rate of CN with decay time shorter than 20 days in the bulge of M31 is $\approx 5.2 \pm 1.1$ yr^{-1}, predicted rates are ≈ 300 yr^{-1} and ≈ 75 yr^{-1} for $\dot{M} = 10^{-8}$ and $10^{-10} M_{\odot}$/yr. The upper limit on the contribution of cataclysmic variables is $\lesssim 7$ per cent in the least favorable case of $\dot{M} = 10^{-10} M_{\odot}$/yr. Yet lower $\dot{M}$ is not feasible for a potential SN Ia progenitor because of the binary evolution consideration Hillebrandt & Niemeyer (2000).

2.7.3 Helium donors

An outcome of the binary evolution Iben & Tutukov (1994) of a two initially massive stars may be a CO white dwarf accreting helium from a helium star. This type of binary systems may be a viable path Yoon & Langer (2003); Wang et al. (2009) to SN Ia, as it is not prone to the well-known shortcoming of the H-accretion models – the strong helium flashes Iben & Tutukov (1994); Livio (2000). Although the $\dot{M}$ scale for helium burning is shifted upwards by an order of magnitude, the mass accumulation efficiency of a helium-accreting white dwarf may be high even at $\dot{M} \sim 10^{-8} - 10^{-7} M_{\odot}$/yr Kato & Hachisu (2004). Because the nuclear burning efficiency is 10 times lower than for hydrogen, the X-ray output of a population of He-accreting white dwarfs will be smaller and may agree with X-ray observations. This channel, however, requires large initial mass of the donor star Yoon & Langer (2003); Wang et al. (2009), $\sim 8 M_{\odot}$, hence it can only produce SN Ia with short delay times, $\sim 10^{7} - 10^{8}$ Myrs and is irrelevant to supernovae in early-type galaxies.

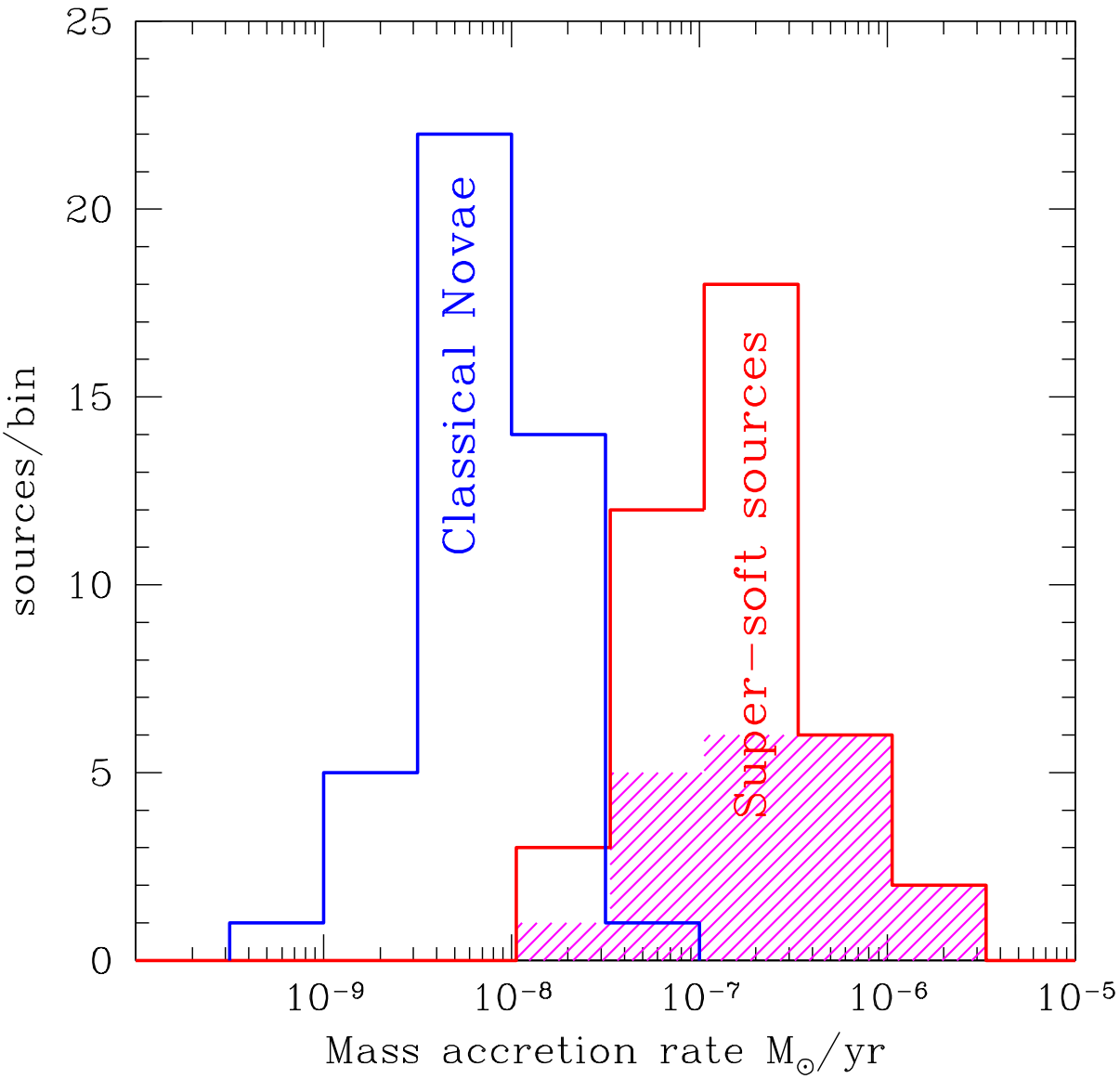

Figure 2.1: The observed mass accretion rate distributions for CNe and supersoft X-ray sources. The $\dot{M}$ for the former were computed from absolute V-band magnitudes Warner (1987) in quiescence using average $M_V - \dot{M}$ relation Puebla et al. (2007) for accreting white dwarfs. The ROSAT SSS sample Greiner (2000) includes sources in the M31, Milky Way and Magellanic Clouds. Their $\dot{M}$ were computed from bolometric X-ray luminosities assuming nuclear burning efficiency for hydrogen and solar abundance of the accreting material. Depending on the detailed spectral shape of the emission from the hydrogen burning layer on the white dwarf surface, the M31 sample may be affected by incompleteness near the low $\dot{M}$ end. For the Milky Way and LMC samples on the contrary, the incompleteness effects are insignificant at $\dot{M} \gtrsim 10^{-8} M_\odot$/yr. Their contribution is shown by the dashed region.

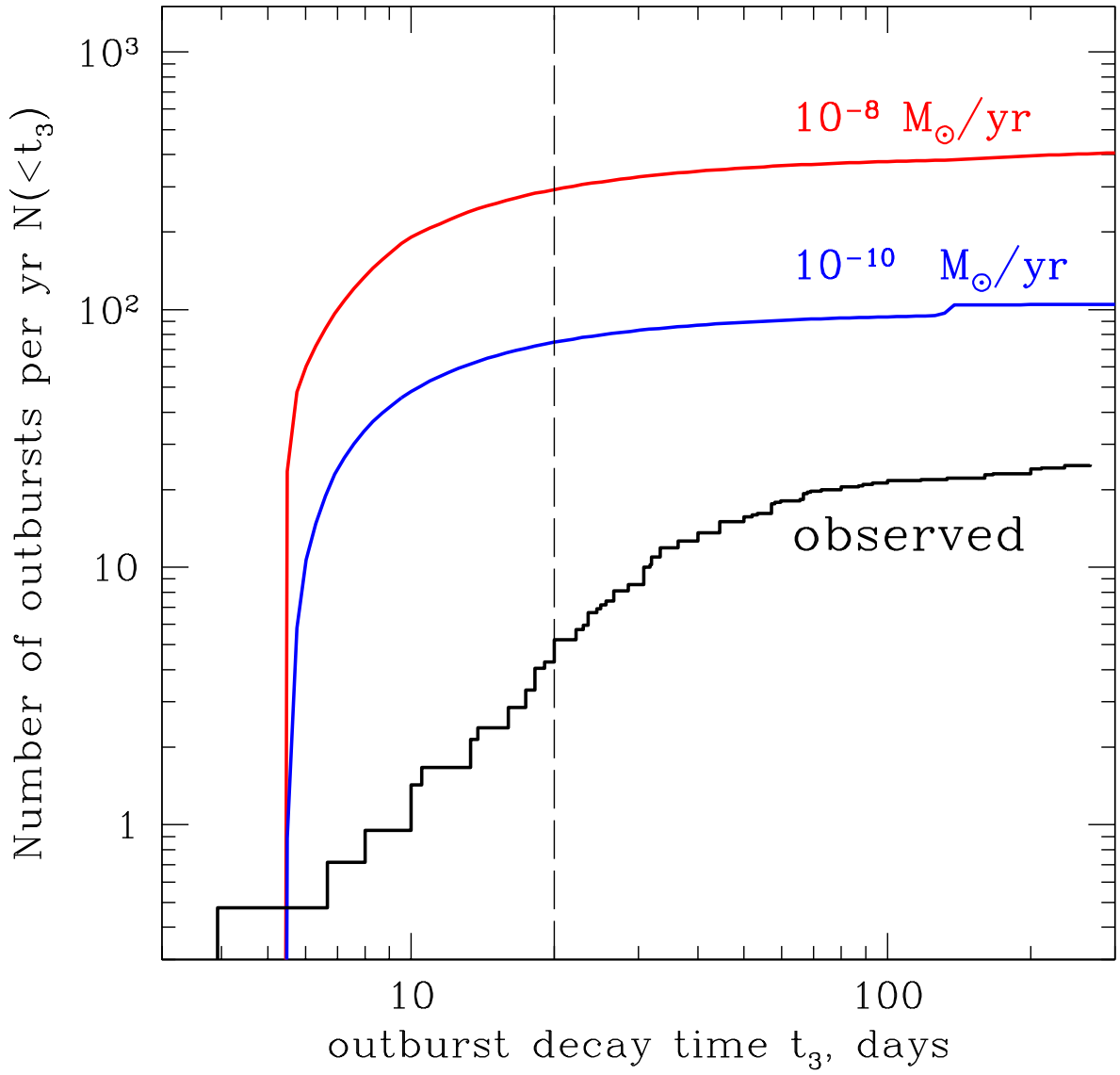

Figure 2.2: The decay time t_3 distribution for CNe in the bulge of M31. The histogram shows the observed Capaccioli et al. (1989) distribution, two smooth lines – predicted ones for two different values of $\dot{M}$. They are computed assuming that cataclysmic variables are the sole progenitors of SN Ia and are based on the results of numerical simulations of CN outburst cycles Yaron et al. (2005) for the white dwarf core temperature of 10^7 K. The distributions are normalized to the CNe rate in the bulge of M31, 25 CN/yr. The vertical dashed line denotes the boundary of the very fast Novae, which statistics is discussed in the text.

Bibliography

Arp, H. C., 1956, AJ, 61, 15

Capaccioli, M., della Valle, M., Rosino, L. & D'Onofrio, M., 1989, 97, 1622

Di Stefano, R., *et al.* 2004, ApJ, 610, 247

Fink, M., Hillebrandt, W. & Röpke, F. K., 2007, A&A, 476, 1133

Gallagher, J. S., *et al.* 2008, ApJ, 685, 752

Greiner, J., 2000, NewA, 5, 137

Hachisu, I., Kato, M. & Nomoto, K. A 1996, ApJ, 470, L97

Hillebrandt, W. & Niemeyer, J. C. 2000, ARA&A, 38, 191

Höflich, P. & Khokhlov, A. 1996, ApJ, 457, 500

Iben, I. Jr. & Tutukov, A. V. 1984, ApJS, 54, 335

Iben, I. Jr. & Tutukov, A. V. 1994, ApJ, 431, 264

Kahabka, P. & van den Heuvel, E. P. J. 1997, ARA&A, 35, 69

Kato, M. & Hachisu, I., 2004, ApJ, 613, L129

Li, X.-D. & van den Heuvel 1997, A&A, 322, L9

Livio, M. 2000, Type Ia Supernovae, Theory and Cosmology. Eds.: J. C. Niemeyer and J. W. Truran. Cambridge University Press, 33

Mannucci, F., *et al.* 2005, A&A, 433, 807

Nomoto, K., Nariai, K. & Sugimoto, D. 1979, PASJ, 31, 287

Nomoto, K., Saio, H., Kato, M. & Hachisu, I. 2007, ApJ, 633, 1269

Nugent, P., Baron, E., Branch, D., Fisher, A. & Hauschildt, P. H. 1997, ApJ, 485, 812

Panei, J. A., Althaus, L. G. & Benvenuto, O. G. 2000, A&A, 353, 970

Puebla, R. E., Diaz, M. P. & Hubeny, I., 2007, AJ, 134, 1923

Schawinski, K. 2009, MNRAS, 397, 717

Shore, S. N., Schwarz, G., Bond, H. E., et al., 2003, AJ, 125, 1507

Terlevich, I. A., & Forbes, D. A. 2002, MNRAS, 330, 547

Wang, B., Meng, X., Chen, X. & Han, Z., 2009, MNRAS, 395, 847

Warner, B., 1987, MNRAS, 227, 23

Webbink, R. 1984, ApJ, 277, 355

Weidemann, W. 2000, A&A, 363, 647

Whelan, J. & Iben, I. Jr. 1973, ApJ, 186, 1007

Yaron, O., Prialnik, D., Shara, M. M. & Kovetz, A. 2005, ApJ, 623, 398

Yoon, S.-C. & Langer, N., 2003, A&A, 412, L53

Chapter 3

Soft band X/K luminosity ratios for gas-poor early-type galaxies

Astronomy & Astrophysics, in press, 2010

Bogdán, Á. & Gilfanov, M.

3.1 Abstract

We aim to place upper limits on the combined X-ray emission from the population of steady nuclear-burning white dwarfs in galaxies. In the framework of the single-degenerate scenario, these systems, known as supersoft sources, are believed to be likely progenitors of Type Ia supernovae.

From the *Chandra* archive, we selected normal early-type galaxies with the point source detection sensitivity better than 10^{37} erg s^{-1} in order to minimize the contribution of unresolved low-mass X-ray binaries. The galaxies, contaminated by emission from ionized ISM, were identified based on the analysis of radial surface brightness profiles and energy spectra. The sample was complemented by the bulge of M31 and the data for the solar neighborhood. To cover a broad range of ages, we also included NGC3377 and NGC3585 which represent the young end of the age distribution for elliptical galaxies. Our final sample includes eight gas-poor galaxies for which we determine L_X/L_K ratios in the 0.3 – 0.7 keV energy band. This choice of the energy band was optimized to detect soft emission from thermonuclear-burning on the surface of an accreting white dwarf. In computing the L_X we included both unresolved emission and soft resolved sources with the color temperature of $kT_{bb} \leq 200$ eV.

We find that the X/K luminosity ratios are in a rather narrow range of $(1.7 - 3.2) \cdot 10^{27}$ erg s^{-1} L$_{K,\odot}$. The data show no obvious trends with mass, age, or metallicity of the host galaxy, although a weak anti-correlation with the Galactic NH appears to exist. It is much flatter than predicted for a blackbody emission spectrum with temperature of $\sim 50 - 75$ eV, suggesting that sources with such soft spectra contribute significantly less than a half to the observed X/K ratios. However, the correlation of the X/K ratios with NH has a significant scatter and in the strict statistical sense cannot be adequately described by a superposition of a power law and a blackbody components with reasonable parameters, thus precluding quantitative constraints on the contribution from soft sources.

3.2 Introduction

In the framework of the singe-degenerate scenario (Whelan, & Iben, 1973) white dwarfs accreting from a donor star in a binary system and burning steadily the accreted material on their surface are believed to be a likely path to the Type Ia Supernova (Hillebrandt & Niemeyer, 2000; Livio, 2000). Nuclear burning is stable (required for the white dwarf to grow in mass) only if the mass accretion rate is high enough, $\dot{M} \sim 10^{-7} - 10^{-6} M_{\odot}$/yr. Given that the nuclear burning efficiency for hydrogen is $\epsilon_H \approx 6 \cdot 10^{18}$ erg/g, the bolometric luminosity of such systems are in the $\sim 10^{37} - 10^{38}$ erg s^{-1} range, making them potentially bright X-ray sources. Their emission, however, has a rather low effective temperature, $T_{\rm eff} \lesssim 50 - 100$ eV and therefore is prone to absorption by cold ISM (Gilfanov & Bogdán, 2009). The brightest and hardest sources of this type are indeed observed as supersoft sources in the Milky Way and nearby galaxies (Greiner, 2000). The rest of the population, however, remains unresolved – weakened by absorption and blended with other types of faint X-ray sources and, thus, makes its contribution to the unresolved X-ray emission from galaxies.

We have proposed recently, that the combined energy output of accreting white dwarfs can be used to measure the rate at which white dwarfs increase their mass in galaxies (Gilfanov & Bogdán, 2009). This allowed us to severely constrain the contribution of the single-degenerate scenario to the observed Type Ia Supernova rate in early-type galaxies. The critical quantity in our argument is the X-ray to K-band luminosity ratio of the population of accreting white dwarfs. This quantity can not be measured unambiguously, due to several reasons. Firstly, galaxies have large populations of bright compact X-ray sources – accreting neutron stars and black holes in binary systems (Gilfanov, 2004). Although their spectra are relatively hard, these sources make a significant contribution to X/K ratios, even in the soft band. Unless their contribution is removed, the obtained X/K ratios are rendered useless. This requires an adequate sensitivity and angular resolution – the combination of qualities, which currently can only be delivered by *Chandra* observatory. Another source of contamination is hot ionized gas present in some of galaxies (Mathews & Brighenti, 2003). Although there is a general correlation of the gas luminosity with the mass of the galaxy, the large dispersion precludes an accurate subtraction of the gas contribution based on, for example, optical properties of galaxies. The gas contribution may increase X/K ratio by $\sim 1 - 2$ orders of magnitude, therefore gas-rich galaxies needs to be identified and excluded from the sample. Finally, other types of faint sources do exist and make their contribution to unresolved X-ray emission. As different components in the unresolved emission can not be separated, only upper limits on the luminosity of white dwarfs can be obtained.

The aim of this paper is to measure L_X/L_K ratios in the $0.3 - 0.7$ keV band for a sample of nearby gas-poor galaxies. The energy range has been optimized in order to detect emission from nuclear burning white dwarfs, taking into account the range of effective temperatures, absorption column densities and the effective area curve of *Chandra* detectors.

The paper is structured as follows: in Section 3.3 we describe the sample selection and data preparation and analysis. We identify and remove gas-rich galaxies from the sample in Section 3.4. The obtained X/K ratios are presented and discussed in Section 3.5. Our results are summarized in Section 3.6.

3.3 Sample selection and data reduction

3.3.1 Sample selection

The superb angular resolution combined with low and stable instrumental background of *Chandra* observatory makes the satellite perfectly suitable for the present study. We searched the *Chandra* archive for observations in the science category "Normal Galaxies" and selected a sample of early-type galaxies with point source detection sensitivity better than 10^{37} erg s^{-1}. This threshold was chosen to minimize the contribution of unresolved low-mass X-ray binaries (LMXBs) and its particular value is explained later in this paper (Section 3.5.2). The sample was further extended to include the bulge of M31 which has similar stellar population and gas and dust content to elliptical galaxies. In order to explore young elliptical galaxies we also added NGC3377 and NGC3585, which would otherwise do not pass our selection criteria due to large point source detection sensitivity.

The thus constructed sample includes 14 galaxies and galaxy bulges, their main properties are listed in Table 3.1. The point source detection sensitivity refers to the 0.5 – 8 keV band, and was calculated assuming average spectrum of LMXBs – a power law with $\Gamma = 1.56$ (Irwin et al., 2003).

3.3.2 *Chandra*

We analyzed 70 archival *Chandra* observations, listed in Table 3.2. The total exposure time of the data is $T_{\rm obs} \approx 2.8$ Ms. For ACIS-I observations we extracted data of the entire ACIS-I array, while for ACIS-S observations we used only the S3 chip. The data reduction was performed with standard CIAO[1] software package tools (CIAO version 4.1; CALDB version 4.1.3).

The main steps of the data reduction are similar to those outlined in Bogdán & Gilfanov (2008). Firstly the flare contaminated time intervals were removed, which decreased the exposure time by $\lesssim$ 10 per cent. Note, that for the point source detection we used the unfiltered data, as longer exposure time outweighs higher background periods. We combined the available data for each galaxy by projecting them into the coordinate system of the observation with the longest exposure time. We ran the CIAO `wavdetect` tool on the merged data in the 0.5 – 8 keV energy range, and applied the same parameters like in Bogdán & Gilfanov (2008). This results in relatively large source cells, in order to minimize the contribution of residual point source counts to the unresolved emission. We find that $\gtrsim$ 98 per cent of the source counts lie within the obtained regions. Because of the large cell size, some of the source cells may overlap in the central regions of some of the galaxies from our sample. However, this is not an issue as the goal of this analysis is the unresolved emission, rather than point sources. The source list was used to mask out point sources in the analysis of the unresolved emission.

The background subtraction has a crucial role in studying the extended X-ray emission. In all galaxies, except for M31, we used a combination of several regions away from the galaxies to estimate the sky and instrumental background components. This technique can not be applied in M31 since its angular size is significantly larger than the field of view of the detectors, therefore we followed the procedure described in Bogdán & Gilfanov (2008). We constructed exposure maps by assuming a power law model with slope

[1] http://cxc.harvard.edu/ciao

Table 3.1: The list of early-type galaxies and galaxy bulges studied for the analysis.

Name	Distance (Mpc)	N_H (cm^{-2})	Morphological type	L_K ($L_{K,\odot}$)	T_{obs} (ks)	T_{filt} (ks)	L_{lim} (erg s^{-1})	R_1 (arcsec)	R_2 (arcsec)
M31 bulge	0.78[a]	$6.7 \cdot 10^{20}$	SA(s)b	$3.7 \cdot 10^{10}$	180.1	143.7	$2 \cdot 10^{35}$	300	720
M32	0.805[b]	$6.3 \cdot 10^{20}$	cE2	$8.5 \cdot 10^{8}$	178.8	172.2	$1 \cdot 10^{34}$	25	90
M60	16.8[c]	$2.2 \cdot 10^{20}$	E2	$2.2 \cdot 10^{11}$	109.3	90.5	$9 \cdot 10^{36}$	50	125
M84	18.4[c]	$2.6 \cdot 10^{20}$	E1	$1.6 \cdot 10^{11}$	117.0	113.8	$9 \cdot 10^{36}$	50	100
M105	9.8[d]	$2.8 \cdot 10^{20}$	E1	$4.1 \cdot 10^{10}$	341.4	314.0	$1 \cdot 10^{36}$	30	90
NGC1291	8.9[e]	$2.1 \cdot 10^{20}$	(R)SB(s)0/a	$6.3 \cdot 10^{10}$	76.7	51.2	$5 \cdot 10^{36}$	60	130
NGC3377	11.2[c]	$2.9 \cdot 10^{20}$	E5-6	$2.0 \cdot 10^{10}$	40.2	34.0	$2 \cdot 10^{37}$	–	79
NGC3585	20.0[c]	$5.6 \cdot 10^{20}$	E7/S0	$1.5 \cdot 10^{11}$	95.9	89.1	$2 \cdot 10^{37}$	50	180
NGC4278	16.1[c]	$1.8 \cdot 10^{20}$	E1-2	$5.5 \cdot 10^{10}$	467.7	443.0	$2 \cdot 10^{36}$	50	110
NGC4365	20.4[c]	$1.6 \cdot 10^{20}$	E3	$1.1 \cdot 10^{11}$	198.3	181.4	$8 \cdot 10^{36}$	30	80
NGC4636	14.7[c]	$1.8 \cdot 10^{20}$	E/S0_1	$8.1 \cdot 10^{10}$	212.5	202.1	$5 \cdot 10^{36}$	30	102
NGC4697	11.8[c]	$2.1 \cdot 10^{20}$	E6	$5.1 \cdot 10^{10}$	195.6	162.0	$4 \cdot 10^{36}$	30	95
NGC5128	3.7[f]	$8.6 \cdot 10^{20}$	S0 pec	$5.8 \cdot 10^{10}$	569.1	568.9	$1 \cdot 10^{36}$	65	240
Sagittarius	0.0248[g]	$1.2 \cdot 10^{21}$	dSph(t)	$8.9 \cdot 10^{5}$	30.1	29.7	$1 \cdot 10^{32}$	–	55

The point source detection sensitivity L_{lim} refers to the 0.5 – 8 keV energy range, the N_H is the Galactic absorption column density (Dickey & Lockman, 1990), T_{obs} and T_{filt} are the exposure times before and after data filtering. The morphologycal types of galaxies are taken from NED (http://nedwww.ipac.caltech.edu/). R_1 and R_2 are the radii used for the inner and outer regions in obtaining the spectra presented in Figure 3.2. The orientation and shape of the regions were taken from K-band measurements (http://irsa.ipac.caltech.edu/applications/2MASS/). Distances are taken from: [a] Stanek & Garnavich (1998); Macri (1983) – [b] Mateo (1998) – [c] Tonry et al. (2001) – [d] Jensen et al. (2003) – [e] de Vaucouleurs (1975) – [f] Ferrarese et al. (2007) – [g] Kunder & Chaboyer (2009).

Table 3.2: The list of *Chandra* observations used for the analysis. The abbreviation "I" in the detector (Det.) column denotes observations performed with ACIS-I, while "S" stands for the ACIS-S detector.

Obs-ID	$T_{\rm obs}$, ks	$T_{\rm filt}$, ks	Date	Det.	Galaxy	Obs-ID	$T_{\rm obs}$, ks	$T_{\rm filt}$, ks	Date	Det.	Galaxy
303	12.0	8.2	1999 Oct 13	I	M31	7075	84.2	79.0	2006 Jul 03	S	M105
305	4.2	4.0	1999 Dec 11	I	M31	7076	70.1	66.7	2007 Jan 10	S	M105
306	4.2	4.1	1999 Dec 27	I	M31	795	39.7	31.7	2000 Jun 27	S	NGC1291
307	4.2	3.1	2000 Jan 29	I	M31	2059	37.0	19.5	2000 Nov 07	S	NGC1291
308	4.1	3.7	2000 Feb 16	I	M31	2934	40.2	34.0	2003 Jan 06	S	NGC3377
311	5.0	3.9	2000 Jul 29	I	M31	2078	35.8	33.1	2001 Jun 03	S	NGC3585
312	4.7	3.8	2000 Aug 27	I	M31	9506	60.2	56.0	2008 Mar 11	S	NGC3585
1575	38.2	38.2	2001 Oct 05	S	M31	4741	37.9	34.7	2005 Feb 03	S	NGC4278
1577	5.0	4.9	2001 Aug 31	I	M31	7077	111.7	103.2	2006 Mar 16	S	NGC4278
1583	5.0	4.1	2001 Jun 10	I	M31	7078	52.1	46.4	2006 Jul 25	S	NGC4278
1585	5.0	4.1	2001 Nov 19	I	M31	7079	106.4	100.2	2006 Oct 24	S	NGC4278
2895	4.9	3.2	2001 Dec 07	I	M31	7080	56.5	53.6	2007 Apr 20	S	NGC4278
2896	5.0	3.7	2002 Feb 06	I	M31	7081	112.1	104.9	2007 Feb 20	S	NGC4278
2897	5.0	4.1	2002 Jan 08	I	M31	2015	41.0	36.1	2001 Jun 02	S	NGC4365
2898	5.0	3.2	2002 Jun 02	I	M31	5921	40.0	37.3	2005 Apr 28	S	NGC4365
4360	5.0	3.4	2002 Aug 11	I	M31	5922	40.0	38.3	2005 May 09	S	NGC4365
4678	4.9	2.7	2003 Nov 09	I	M31	5923	40.1	34.7	2005 Jun 14	S	NGC4365
4679	4.8	2.7	2003 Nov 26	I	M31	5924	27.1	25.7	2005 Nov 25	S	NGC4365
4680	5.2	3.2	2003 Dec 27	I	M31	7224	10.1	9.3	2005 Nov 26	S	NGC4365
4681	5.1	3.3	2004 Jan 31	I	M31	323	53.0	46.4	2000 Jan 26	S	NGC4636
4682	4.9	1.2	2004 May 23	I	M31	324	8.5	4.7	1999 Dec 04	I	NGC4636
7064	29.1	23.2	2006 Dec 04	I	M31	3926	75.7	75.7	2003 Feb 14	I	NGC4636
7068	9.6	7.7	2007 Jun 02	I	M31	4415	75.3	75.3	2003 Feb 15	I	NGC4636
2017	46.5	42.2	2001 Jul 24	S	M32	784	39.8	37.8	2000 Jan 15	S	NGC4697
2494	16.2	13.9	2001 Jul 28	S	M32	4727	40.4	36.4	2003 Dec 26	S	NGC4697
5690	116.1	116.1	2005 May 27	S	M32	4728	36.2	31.4	2004 Jan 06	S	NGC4697
785	38.6	23.2	2000 Apr 20	S	M60	4729	38.6	19.5	2004 Feb 12	S	NGC4697
8182	53.0	49.6	2007 Jan 30	S	M60	4730	40.6	36.9	2004 Aug 18	S	NGC4697
8507	17.7	17.7	2007 Feb 01	S	M60	7797	98.2	98.0	2007 Mar 22	I	NGC5128
803	28.8	28.6	2000 May 19	S	M84	7798	92.0	92.0	2007 Mar 27	I	NGC5128
5908	46.7	46.1	2005 May 01	S	M84	7799	96.0	96.0	2009 Mar 30	I	NGC5128
6131	41.5	39.1	2005 Nov 07	S	M84	7800	92.0	92.0	2007 Apr 17	I	NGC5128
1587	31.9	25.1	2001 Feb 13	S	M105	8489	95.2	95.2	2007 May 08	I	NGC5128
7073	85.2	76.8	2006 Jan 23	S	M105	8490	95.7	95.7	2007 May 30	I	NGC5128
7074	70.0	66.4	2006 Apr 09	S	M105	4448	30.1	29.7	2003 Sep 01	I	Sagittarius

of $\Gamma = 2$.

3.3.3 Near-infrared data

In order to trace the stellar light distribution we use the K-band data of 2MASS Large Galaxy Atlas (Jarrett et al., 2003). Due to the large angular size of M31, the background is somewhat oversubtracted on its near-infrared images (T. Jarrett, private communication). Hence the outer bulge and disk of the galaxy appears to be too faint. To avoid uncertainties caused by the improper background subtraction, we used the Infrared Array Camera (IRAC) onboard *Spitzer Space Telescope* (*SST*) to trace the stellar light in M31. In order to facilitate the comparison of results with other galaxies in our sample, we convert the observed near-infrared *Spitzer* luminosities to K-band values. The scale between the 3.6 μm IRAC and 2MASS K-band data was determined in the center of M31, where the background level is negligible. The obtained conversion factor between the pixel values is $C_K/C_{3.6\ \mu\mathrm{m}} \approx 10.4$.

3.4 Identifying gas-poor galaxies

In many luminous elliptical galaxies truly diffuse emission is present, originating from warm ionized gas. Its luminosity may exceed significantly the emission from unresolved compact X-ray sources. Therefore our aim is to identify the emission of warm ionized gas, and, if possible, to separate it from unresolved faint compact sources. In order to reveal the presence and map the distribution of the ISM we construct radial surface brightness profiles of the unresolved X-ray emission and study its spectra.

In Figure 3.1 the distribution of X-ray surface brightness is shown for the studied galaxies. The profiles were extracted in the $0.5-2$ keV energy band using circular annuli, centered in the center of the galaxy. The data is corrected for vignetting, all background components are subtracted. The contribution of resolved compact sources is removed as described in the previous Section.

It is known that the distribution of unresolved compact objects follows the stellar mass (Revnivtsev et al., 2006; Bogdán & Gilfanov, 2008; Revnivtsev et al., 2008). Hence we look for deviations of the X-ray profile from the distribution of the K-band light as an indication of a presence of additional emission component, presumably emission of warm ionized gas. There are five galaxies, M32, M105, NGC3377, NGC3585 and Sagittarius in which the X-ray brightness closely follows the stellar light distribution at all central distances. In several others – M31, M60, NGC1291 and NGC4278 the X-ray emission follows the near-infrared light only in the outer regions. In the inner parts of these galaxies an additional X-ray emitting component is present and often dominates. In all other cases the X-ray surface brightness strikingly deviates from the near-infrared light distribution, indicating the presence of strong additional X-ray emitting components. The most different X-ray and K-band profiles are observed in M84, NGC4636 and in NGC5128. These galaxies are known to show recent activity in their nuclei (e.g. Finugenov et al., 2008; Kraft et al., 2008; Baldi et al., 2009).

To confirm the presence of emission from ionized gas, we investigate the spectra of unresolved emission (Figure 3.2). As the gas emission is more centrally concentrated in some of the galaxies, we make distinction between inner and outer regions. The dividing radii are listed in Table 3.1. Similar to the radial

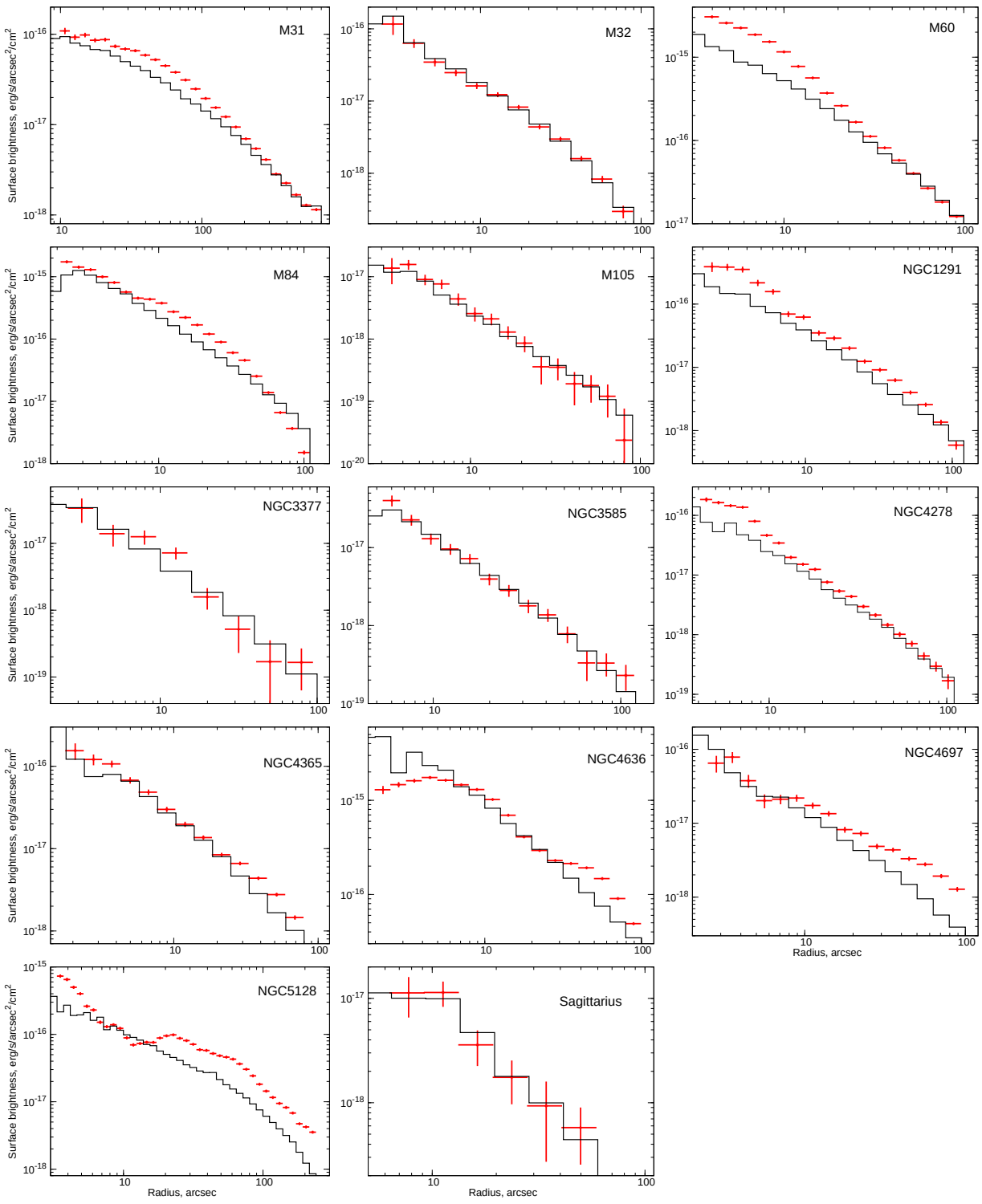

Figure 3.1: Surface brightness profiles of the 14 galaxies in our sample in the 0.5 – 2 keV energy range. All background components are subtracted. Crosses (red) show the distribution of unresolved X-ray emission based on *Chandra* data, the solid line (black) shows the (arbitrarily) re-normalized near-infrared brightness.

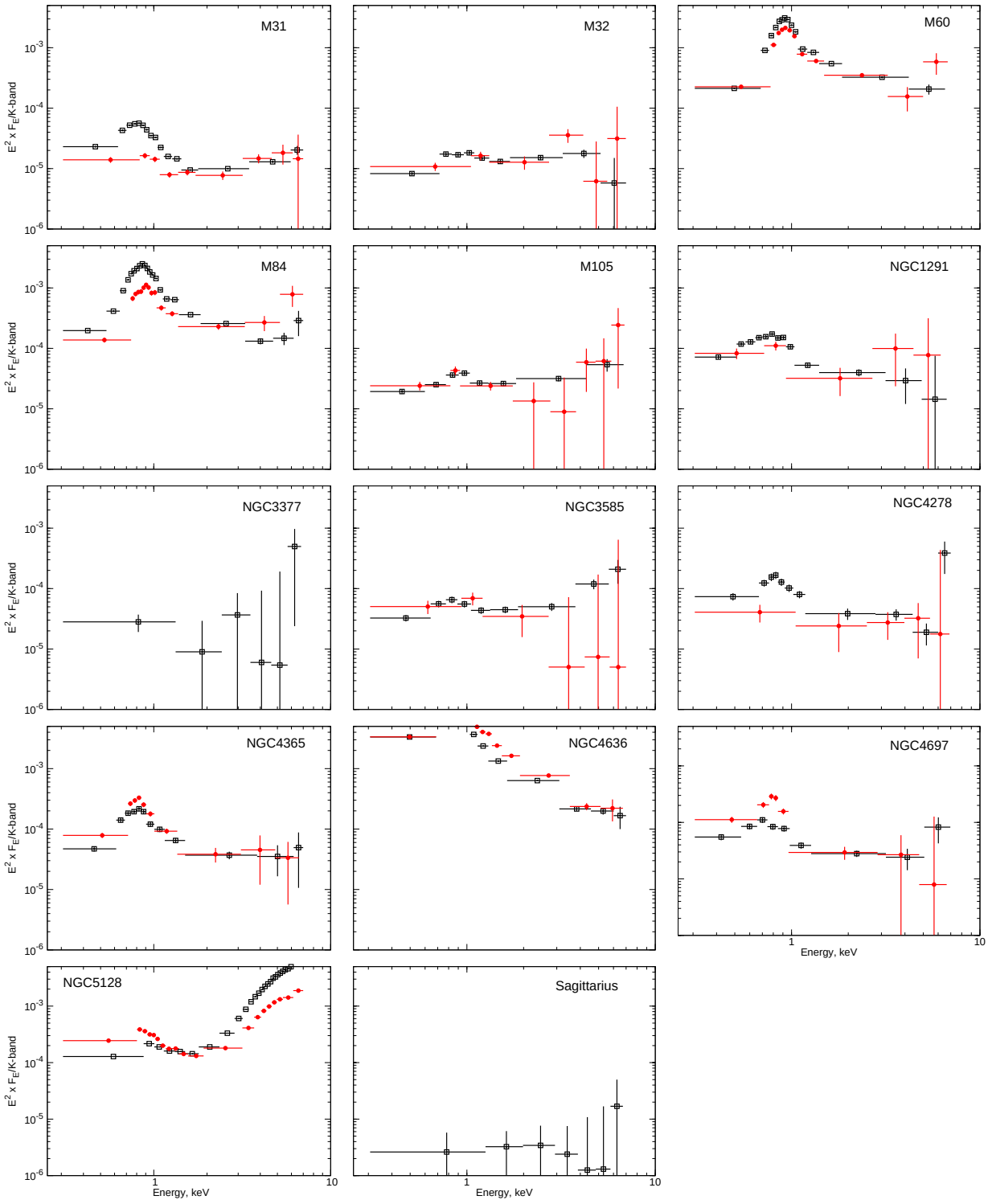

Figure 3.2: Energy spectra of the 14 galaxies in our sample. All spectra are normalized to the same level of near-infrared brightness and to an assumed distance of 10 Mpc, background is subtracted. The scales on the *x*-axis and on the *y*-axis are the same in all panels. For each galaxy, hollow squares (black) show the spectrum of the inner region, while filled circles (red) represent the outer region spectrum. In case of NGC3377 and Sagittarius spectra of the entire galaxy are shwon because of the relatively low number of counts.

Table 3.3: Results of spectral fits of unresolved emission for 14 early-type galaxies.

Name	kT_{MKL} (keV)	Γ	L_{MKL} (erg s^{-1})	L_{PL} (erg s^{-1})	L_{LMXB} (erg s^{-1})	L_{MKL}/L_{PL}	$L_{MKL}/(L_{PL}-L_{LMXB})$	χ^2/d.o.f
M31 bulge	0.32 ± 0.01	1.82 ± 0.04	$1.8 \cdot 10^{38}$	$2.5 \cdot 10^{38}$	–	0.72	0.72	473/223
M32	0.60 ± 0.13	1.65 ± 0.15	$1.1 \cdot 10^{36}$	$5.3 \cdot 10^{36}$	–	0.21	0.21	76/70
M60	0.80 ± 0.01	1.70 ± 0.11	$6.2 \cdot 10^{40}$	$1.5 \cdot 10^{40}$	$2.0 \cdot 10^{39}$	4.13	4.77	1015/100
M84	0.65 ± 0.01	1.45 ± 0.12	$3.0 \cdot 10^{40}$	$1.1 \cdot 10^{40}$	$1.5 \cdot 10^{39}$	2.73	3.16	385/122
M105	0.64 ± 0.05	2.26 ± 0.19	$4.7 \cdot 10^{37}$	$1.8 \cdot 10^{38}$	$3.8 \cdot 10^{37}$	0.26	0.33	74/73
NGC1291	0.31 ± 0.03	2.64 ± 0.23	$6.3 \cdot 10^{38}$	$9.9 \cdot 10^{38}$	$3.2 \cdot 10^{38}$	0.64	0.94	83/67
NGC3377	0.4	2.15 ± 0.47	$< 1.8 \cdot 10^{37}$	$3.0 \cdot 10^{38}$	$3.3 \cdot 10^{38}$	< 0.06	–	45/34
NGC3585	0.4	2.75 ± 0.61	$< 8.0 \cdot 10^{38}$	$2.5 \cdot 10^{39}$	$3.0 \cdot 10^{39}$	< 0.32	–	46/39
NGC4278	0.47 ± 0.06	2.34 ± 0.31	$5.1 \cdot 10^{38}$	$1.1 \cdot 10^{39}$	$1.1 \cdot 10^{38}$	0.46	0.52	151/132
NGC4365	0.49 ± 0.04	1.67 ± 0.17	$2.4 \cdot 10^{39}$	$2.8 \cdot 10^{39}$	$9.0 \cdot 10^{38}$	0.86	1.26	128/98
NGC4636	0.59 ± 0.01	2.64 ± 0.05	$1.1 \cdot 10^{41}$	$1.3 \cdot 10^{40}$	$4.1 \cdot 10^{38}$	8.46	8.74	1122/199
NGC4697	0.33 ± 0.03	2.54 ± 0.54	$7.3 \cdot 10^{38}$	$4.7 \cdot 10^{38}$	$2.1 \cdot 10^{38}$	1.55	2.81	78/66
NGC5128	0.62 ± 0.01	-0.76 ± 0.01	$2.1 \cdot 10^{39}$	$3.0 \cdot 10^{40}$	$5.1 \cdot 10^{37}$	0.07	0.07	3547/435
Sagittarius	0.4	2.44 ± 0.51	$< 1.2 \cdot 10^{33}$	$2.5 \cdot 10^{33}$	–	< 0.48	< 0.48	18/20

The spectra were derived from full regions which parameters are presented in the Table 3.1 and fitted by a model consisting of a power law and an optically-thin plasma emission model (MEKAL in XSPEC, solar composition). The hydrogen column density was fixed at the Galactic value (Dickey & Lockman, 1990). Column marked kT_{MKL} lists the temperature of thermal emission, Γ is the photon index of the power law. The 0.5 – 8 keV luminosities are listed in the corresponding columns; L_{LMXB} is the combined luminosity of unresolved low-mass X-ray binaries brighter than 10^{35} erg/s (but fainter than the sensitivity limit for the given galaxy) estimated from the K-band luminosity of the studied region and the average LMXB X-ray luminosity function of Gilfanov (2004). L_{MKL}/L_{PL} is the observed luminosity ratio of the soft thermal component to the power law. $L_{MKL}/(L_{PL}-L_{LMXB})$ is the same ratio corrected for contribution of unresolved LMXBs. For NGC3377 and NGC3585 the predicted LMXB luminosity exceeds the observed luminosity of the power law component, presumably due to a scatter in X/K ratios for LMXBs, therefore no LMXB-corrected luminosity ratio is computed.

profiles we excluded the contribution of resolved compact sources. In order to facilitate the comparison, all spectra, shown in Figure 3.2, are normalized to the same K-band luminosity of $L_K = 10^{11}$ $L_{K,\odot}$ and projected to a distance of 10 Mpc. In case of Sagittarius and NGC3377 we show only the spectrum of the entire galaxy due to the relatively low number of counts. The emission from the hot ISM reveals itself as a soft component, clearly visible in the spectra of many of the galaxies. In order to characterize quantitatively its contribution we performed fits to the spectra of unresolved emission (Table 3.3), using the MEKAL model in XSPEC to represent the emission from ionized gas and a power law spectrum for the contribution of unresolved compact sources. The metal abundances for the thermal component were fixed at the solar values. Such a simple model does not always describe the observed spectra well from the statistical point of view, as illustrated by the large chi-square values given in the last column of the Table 3.3. However, it does describe the spectra with relative accuracy of better than $\lesssim$ 10 per cent which is entirely sufficient for the purpose of this calculation. The contribution of the hot ISM is, in principle, characterized by the ratio of luminosities of thermal and power law components. The latter however includes contribution of unresolved LMXBs, which may be dominant for galaxies with a too large point source detection sensitivity, $\gtrsim 10^{36}$ erg/s, making the luminosity ratios also dependent on the sensitivity of the available Chandra data. In order to compensate for this, we estimated the contribution of unresolved LMXBs using the average LMXB X-ray luminosity function of Gilfanov (2004) and subtracted their contribution from the luminosity of the power law component. These corrected values are shown in the column labeled $L_{MKL}/(L_{PL} - L_{LMXB})$ in the Table 3.3.

The spectral analysis results presented in Table 3.3 lead to the conclusions consistent with the brightness profile analysis. As expected from surface brightness profiles, M32, M105, NGC3377, NGC3585 and Sagittarius show the same spectral properties at all central radii – they have a rather weak soft component. In M31 and in NGC4278 there is a significant difference between the spectra of inner and outer regions – the luminous soft component is present only in the former, suggesting that the hot gas is centrally concentrated (Bogdán & Gilfanov, 2008). In all other galaxies the soft component dominates at all central radii, and can be well fitted with an optically-thin thermal plasma emission model with temperature in the range of $kT \approx 0.3 - 0.8$ keV, in a good agreement with previous studies (Sarazin et al., 2001; Irwin et al., 2002; Sivakoff et al., 2003; Randall et al., 2004).

Based on radial profiles and spectral analysis we conclude that the following seven galaxies are relatively gas-poor and may be suitable for our analysis: the bulge of M31, M32, M105, NGC3377, NGC3585, NGC4278 and Sagittarius. In all other cases the signatures of a recent activity of the galactic nucleus and/or large amount of hot gas make the galaxies unsuitable for our study.

3.5 Results

3.5.1 Resolved supersoft sources

Due to large bolometric luminosity, $\sim 10^{37} - 10^{38}$ erg/s some (generally speaking unknown) fraction of the nuclear burning white dwarfs will be detected by *Chandra* as supersoft sources, despite the low color temperature of their emission. These sources obviously should be included in computing the final X/K ra-

tios. In order to separate them from LMXBs we use spectral properties of compact sources. The temperature of the hydrogen burning layer is in the range of $T_{eff} \sim 30 - 100$ eV, but we conservatively included all resolved sources having hardness ratios corresponding to the blackbody temperature lower than $kT_{bb} < 200$ eV. We used this method for all galaxies, except for M31, where we relied on the catalogue of supersoft sources from Di Stefano et al. (2004). Because of the increased source cell size (Section 3.3) some of the sources are merged into one. This may compromise identification of supersoft sources as some of them may in principle be confused with harder sources and missed in our analysis. To exclude this possibility, we repeated analysis with nominal source cell size and did not find any difference in the list of super-soft sources.

3.5.2 L_X/L_K ratios

The results of our analysis are presented in Table 3.4. Listed in the table are: X-ray luminosity of unresolved emission $L_{\rm X,unres}$, of resolved supersoft sources $L_{\rm X,sss}$, and of ionized gas $L_{\rm X,gas}$. From these quantities and from the K-band luminosity of the studied region (Table 3.1) we compute the X-ray to K-band luminosity ratios – $L_{\rm X}/L_{\rm K}$. In the case of M31 and in NGC4278 we compute L_X/L_K ratio in the outer regions, where no significant gas emission is detected. The Milky Way value was obtained using the results of Sazonov et al. (2006), who computed the luminosity of active binaries (ABs) and cataclysmic variables (CVs) in the Solar neighborhood. The interstellar absorption is negligible in this case. We converted their X-ray-to-mass ratios from the 0.1 – 2.4 keV band to the 0.3 – 0.7 keV energy range, using typical spectrum of ABs and CVs (see Figure 3.3), and assuming a mass-to-light ratio of $M_\star/L_K = 1.0$ (Kent, 1992)

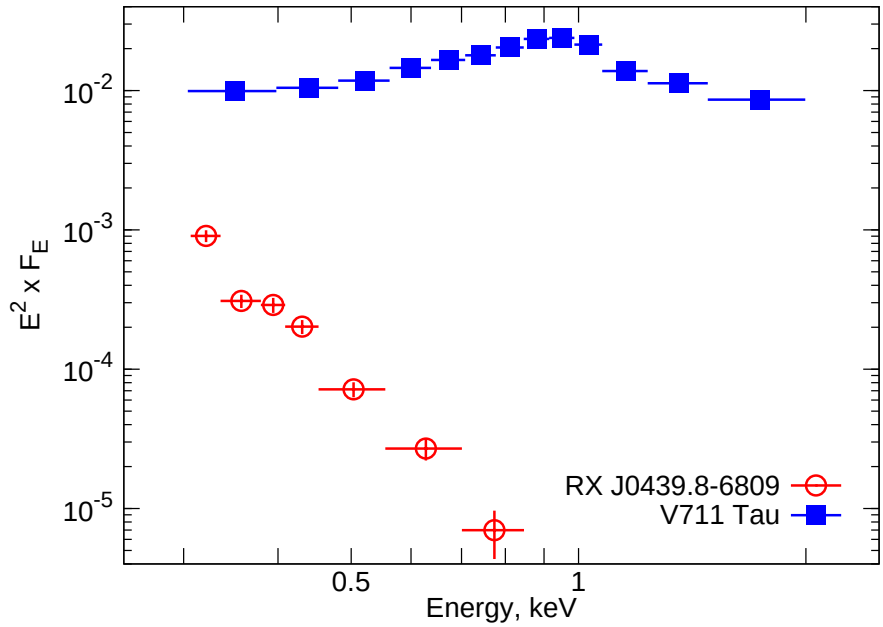

Figure 3.3: The spectrum of the active binary V711 Tau and of a steady nuclear burning white dwarf of RX J0439.8-6809. The spectrum of the former was extracted using *XMM-Newton* data, while the latter was observed by *Chandra*. The background is subtracted from both spectra.

The obtained ratios are in the range of $L_X/L_K = (1.2 - 4.1) \cdot 10^{27}$ erg s^{-1} L$_{K,\odot}^{-1}$ and show a large dispersion. This dispersion is caused by the large difference in the point source detection sensitivity for the galaxies in our sample (Table 3.1). In order to correct for this effect and to bring all galaxies to the same source detection sensitivity we chose the threshold luminosity of $2 \cdot 10^{36}$ erg s^{-1}. In those galaxies which had better source detection sensitivity (M31 bulge, M32, M105, Sagittarius) we did not remove any source fainter than $2 \cdot 10^{36}$ erg s^{-1} in computing the luminosity of "unresolved" emission. In case of NGC3377 and NGC3585 having much worse detection sensitivity we subtracted the contribution of unresolved LMXBs in the luminosity range of $2 \cdot 10^{36} - 2 \cdot 10^{37}$ erg s^{-1} from the measured luminosity of unresolved emission. To estimate the former we used two methods. In the first method, we measured the combined X-ray emission from hard resolved sources in this luminosity range in three galaxies, M31, M105, NGC4278, which allowed us to compute for each of these three galaxies the L_X/L_K ratio due to such sources. We obtained fairly uniform values with the average number of $\approx (1.5 \pm 0.2) \cdot 10^{27}$ erg s^{-1} L$_{K,\odot}^{-1}$, where the cited error is rms of the calculated values. In the second method, the contribution of unresolved hard sources was estimated from the luminosity function of LMXBs (Gilfanov, 2004). In the luminosity range of $2 \cdot 10^{36} - 2 \cdot 10^{37}$ erg s^{-1} the X-ray to K-band luminosity ratio is $\approx 1.4 \cdot 10^{28}$ erg s^{-1} L$_{K,\odot}^{-1}$ in the 2 – 10 keV band. In order to convert this value to the 0.3 – 0.7 keV energy range we use the average spectrum of LMXBS, described by a power law model with slope of $\Gamma = 1.56$ (Irwin et al., 2003) and assume a column density of $N_H = 4 \cdot 10^{20}$ cm^{-2}. The obtained value is $L_X/L_K \approx (1.7 \pm 0.1) \cdot 10^{27}$ erg s^{-1} L$_{K,\odot}^{-1}$ which is in a reasonable agreement with the value obtained from the first method.

Note that both methods are based on the assumption that the X/K ratio for LMXBs is the same for all galaxies in the sample. This assumption may be contradicted by the fact that in NGC 3377 and NGC 3585 the predicted luminosity of unresolved LMXBs exceeds the observed luminosity of unresolved emission (Table 3.3). Incidentally or not, these are the two youngest galaxies in our sample. The possible age dependence of the LMXB X/K ratio can not be excluded but remains yet to be established. On the other hand, the correction due to unresolved LMXBs is less than $\lesssim 40$ per cent of the observed value of L_X/L_K (Table 3.4). This accuracy is sufficient for the present study, which purpose is to constrain the luminosity of nuclear burning white dwarfs. Therefore we defer further investigation of the possible effect of non-constant LMXB X/K ratio for a follow-up study.

The X-ray to K-band luminosity ratios transformed to the same point sources detection sensitivity are listed in Table 3.4. These numbers are fairly uniform $L_X/L_K = (2.4 \pm 0.4) \cdot 10^{27}$ erg s^{-1} L$_{K,\odot}^{-1}$, where, as before, the cited error refers to the rms of the measured values.

3.5.3 Contribution of unresolved LMXBs

The excellent source detection sensitivity, achieved in the bulge of M31, and the large number of compact X-ray sources in this galaxy allows us to estimate the contribution of unresolved LMXBs having the luminosities below the adopted threshold of $2 \cdot 10^{36}$ erg/s to the L_X/L_K ratio. We consider the inner 6 arcmin of the bulge where the source detection is complete down to $2 \cdot 10^{35}$ erg s^{-1} (Voss & Gilfanov, 2007). In this region we collect all compact sources with the luminosity in the range $2 \cdot 10^{35} - 2 \cdot 10^{36}$ erg/s, excluding those classified as supersoft sources. The combined X-ray luminosity of these sources is

Table 3.4: X-ray luminosities in the 0.3 – 0.7 keV band of various X-ray emitting components in gas-poor galaxies.

Name	$L_{\mathrm{X,unres}}$ (erg s^{-1})	$L_{\mathrm{X,sss}}$ (erg s^{-1})	$L_{\mathrm{X,gas}}$ (erg s^{-1})	$L_{\mathrm{X}}/L_{\mathrm{K}}$ (erg s^{-1} $\mathrm{L}_{\mathrm{K},\odot}^{-1}$)	$(L_{\mathrm{X}}/L_{\mathrm{K}})_{\mathrm{corr}}$ (erg s^{-1} $\mathrm{L}_{\mathrm{K},\odot}^{-1}$)	Age (Gyr)
(1)	(2)	(3)	(4)	(5)	(6)	(7)
M31 bulge	$1.1 \cdot 10^{38}$	$3.5 \cdot 10^{37}$	$7.9 \cdot 10^{37}$	$(1.8 \pm 0.2) \cdot 10^{27}$	$(2.2 \pm 0.2) \cdot 10^{27}$	6-10[a]
M32	$6.4 \cdot 10^{35}$	$9.0 \cdot 10^{35}$	–	$(1.8 \pm 0.2) \cdot 10^{27}$	$(2.4 \pm 0.2) \cdot 10^{27}$	4-10[b]
M105	$6.4 \cdot 10^{37}$	$1.9 \cdot 10^{37}$	–	$(2.0 \pm 0.2) \cdot 10^{27}$	$(2.0 \pm 0.2) \cdot 10^{27}$	8-15[c]
NGC3377	$6.7 \cdot 10^{37}$	$1.1 \cdot 10^{37}$	–	$(3.9 \pm 0.6) \cdot 10^{27}$	$(2.4 \pm 0.6) \cdot 10^{27}$	4.1[d]
NGC3585	$6.2 \cdot 10^{38}$	–	–	$(4.1 \pm 0.3) \cdot 10^{27}$	$(2.6 \pm 0.3) \cdot 10^{27}$	3.1[d]
NGC4278	$5.5 \cdot 10^{38}$	$3.4 \cdot 10^{37}$	$4.1 \cdot 10^{38}$	$(3.2 \pm 0.2) \cdot 10^{27}$	$(3.2 \pm 0.2) \cdot 10^{27}$	10.7[d]
Sagittarius	$3.5 \cdot 10^{32}$	$7.3 \cdot 10^{32}$	–	$(1.2 \pm 0.4) \cdot 10^{27}$	$(1.7 \pm 0.4) \cdot 10^{27}$	6.5-9.5[e]
Milky Way	–	–	–	$(3.4 \pm 1.0) \cdot 10^{27}$	–	–

(1) Name (2) Luminosity of unresolved X-ray emission (3) Luminosity of resolved supersoft sources (4) Luminosity of ionized gas (5) Observed X-ray to K-band ratio (6) X-ray to K-band ratio transformed to the same point source detection sensitivity of $2 \cdot 10^{36}$ erg s^{-1}. The errors in columns 5 and 6 correspond to statistical uncertainties in X-ray count rates. (7) Age of the stellar population. References for ages: [a] Olsen et al. (2006), [b] Coelho et al. (2009), [c] Gregg et al. (2004), [d] Terlevich & Forbes (2002), [e] Bellazzini et al. (2006)

divided by the near-infrared luminosity of the same region, to produce $L_X/L_K = (3.6\pm0.3)\cdot10^{26}$ erg s^{-1} L$_{K,\odot}^{-1}$. This number represents the L_X/L_K ratio in the soft band of low-mass X-ray binaries with luminosities in the $2\cdot10^{35} - 2\cdot10^{36}$ erg s^{-1} range. We conclude that LMXBs contribute $\sim$ 15 per cent to the L_X/L_K ratio derived above.

3.5.4 The effect of the interstellar absorption

The possible effect of the interstellar absorption on the observed X-ray luminosities, depends on the energy spectra of the main X-ray emitting components – active binaries and supersoft sources. ABs have significantly harder spectra than supersoft sources, which is illustrated in Figure 3.3. The class of ABs is represented by V711 Tau, it was observed by *XMM-Newton* for 3.2 ks in Obs-ID 0116340601, while RX J0439.8-6809 is an example of steady hydrogen burning sources, based on a *Chandra* exposure with 8.1 ks in Obs-ID 83. As a consequence of the harder spectrum ABs are less affected by the interstellar absorption.

In Figure 3.4 we plot the corrected X/K ratio ($(L_X/L_K)_{corr}$ in Table 3.4) against the Galactic column density. A weak anti-correlation between these two quantities appears to exist. This dependence or, rather, absence of a stronger one, can be used, in principle, to further constrain the contribution of sources with

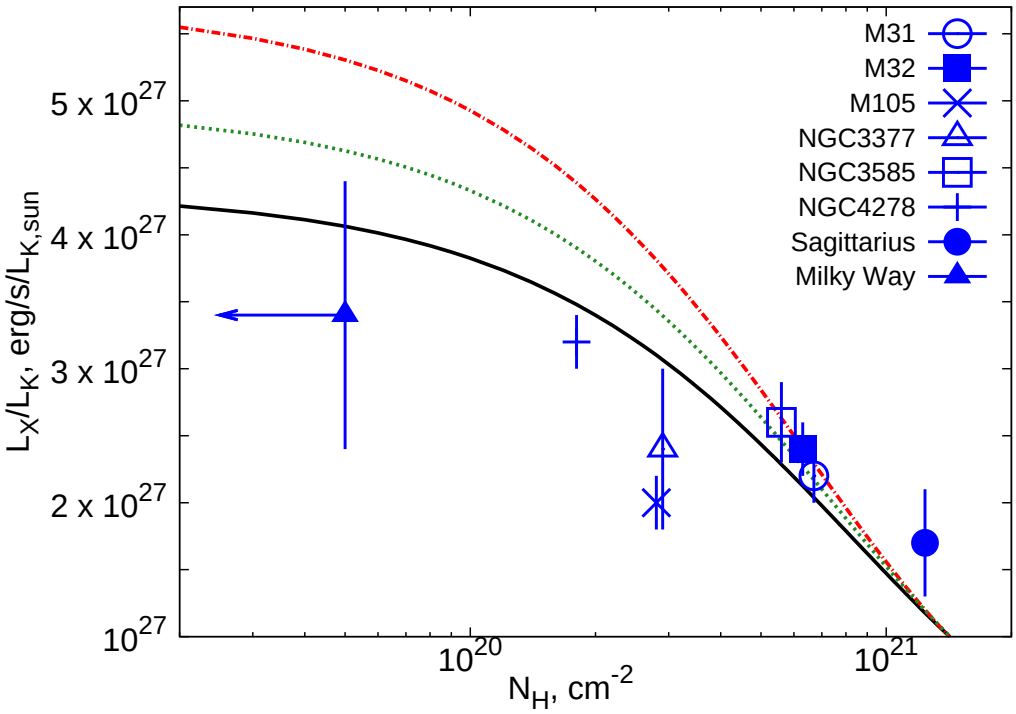

Figure 3.4: The sensitivity corrected L_X/L_K ratio versus Galactic column density. The solid line (black) shows the dependence of the absorbed flux on the N_H assuming a power law emission spectrum with slope $\Gamma = 2$. The dotted line (green in the color version of this plot) and the dashed-dotted line (red) correspond to the combination of the same power law with a blackbody spectrum with $kT_{bb} = 75$ eV and $kT_{bb} = 50$, respectively. The two components have same unabsorbed luminosities in the 0.3 – 0.7 keV band.

soft spectra to the X/K ratio. Indeed, the data is roughly consistent with the N_H dependence for emission with a power law spectrum with the slope $\Gamma = 2$. The value obtained for the Solar neighborhood also fits well this dependence. On the other hand, a much steeper dependence would be expected if a significant fraction (e.g. a half of the unabsorbed flux) of the 0.3 – 0.7 keV emission had a blackbody spectrum with temperature of 50 eV. This suggests that contribution of sources with soft emission spectra, $kT_{bb} \sim 50-75$ eV is not dominant. The discrepancy decreases quickly, with the temperature of the soft emission, and becomes negligible for the blackbody temperature of $kT_{bb} \sim 100$ eV which has approximately same dependence as a $\Gamma = 2$ power law. Therefore the contribution of the sources with harder spectra could not be constrained using this method.

Due to remaining dispersion in the data points caused by unknown systematic effects, the data can not be adequately fitted in a strict statistical sense by a combination of power law and soft spectral components with reasonable parameters. For this reason quantitative constrains on the contribution of sources with soft spectra would not be feasible. However the qualitative conclusion from the analysis of the N_H dependence of the L_X/L_K ratio is in general agreement with the result of Sazonov et al. (2006), who concluded that the emission from accreting white dwarfs contributes $\lesssim 1/3$ to the L_X/L_K ratio of the Solar neighborhood in the 0.1 – 2.4 keV energy band.

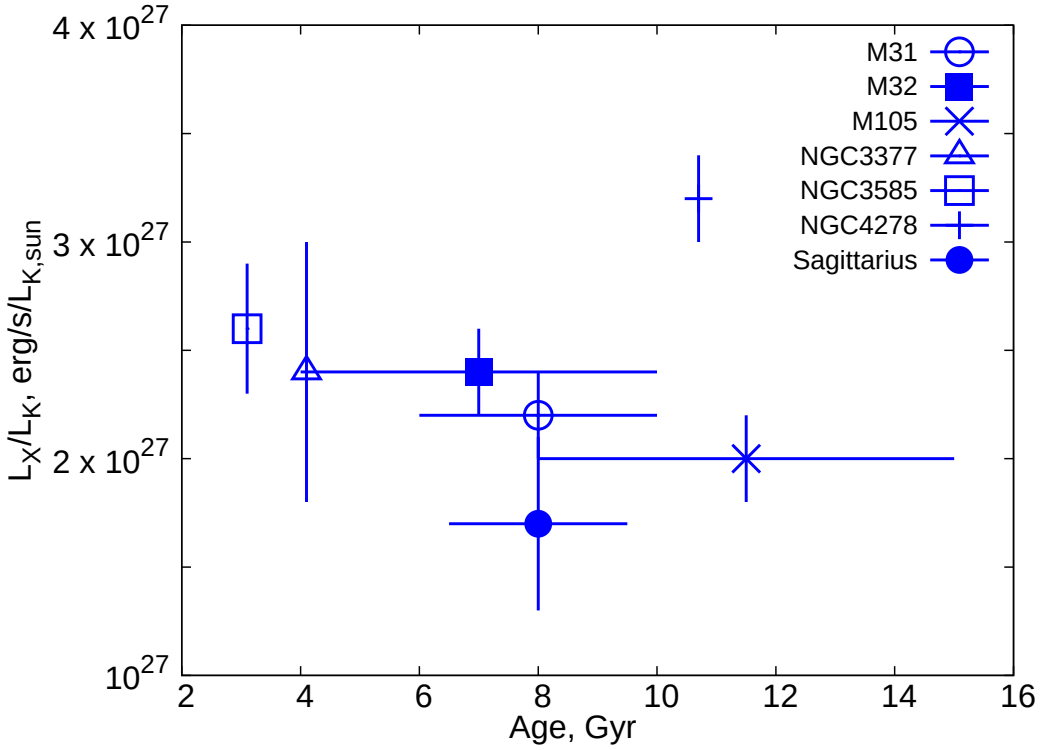

Figure 3.5: The sensitivity corrected X-ray to K-band luminosity ratio versus the age of the stellar population.

3.5.5 Dependence of L_X/L_K ratios on the parameters of galaxies

We did not find any obvious correlations of the sensitivity corrected L_X/L_K ratios with the mass, metallicity (Terlevich & Forbes, 2002) and age (Figure 3.5) of the host galaxy. In particular, we conclude tentatively that there is no significant difference between younger ($\sim 3-4$ Gyrs) and older ($\sim 6-12$ Gyrs) early-type galaxies in our sample (but see the comment in the end of the Section 3.5.2 regarding the possible effect of the non-constant LMXB X/K ratio on the result of the sensitivity correction applied to the two youngest galaxies in our sample).

3.6 Conclusions

Based on *Chandra* archival data we have measured the X-ray to K-band luminosity ratio in the $0.3-0.7$ keV energy band in a sample of nearby gas-poor early-type galaxies. In computing the X/K ratios we retained only those components of X-ray emission, which could be associated with the emission of steady nuclear burning white dwarfs, namely unresolved emission and emission of resolved supersoft sources. To this end, we excluded from our sample gas-rich galaxies and removed the contribution of resolved low-mass X-ray binaries. Our final sample contains seven external galaxies covering a broad range of stellar masses and galaxy ages. It was complemented by the Solar neighborhood data.

We measured fairly uniform set of X/K ratios with average value of $L_X/L_K = (2.4 \pm 0.4) \cdot 10^{27}$ erg/s/$L_{K,\odot}$. The error associated with this number corresponds to the rms of the values obtained for individual galaxies. We estimate, that unresolved low-mass X-ray binaries contribute ~ 15 per cent of this value. We did not find any significant dependence of X/K ratios on the parameters of the galaxies, namely, their mass, age, metallicity. There appears to be a weak anti-correlation of X/K ratios with the galactic absorption column N_H. The relative flatness of this dependence suggests that contribution of the sources with soft spectra $kT_{bb} \lesssim 50-75$ eV to this ratio is not dominant. The remaining dispersion in the data points precludes more rigorous and quantitative conclusions.

Acknowledgements. We thank the anonymous referee for his/her useful and constructive comments. This research has made use of *Chandra* archival data provided by the *Chandra* X-ray Center in the application package CIAO. This research has made use of *Chandra* archival data provided by the *Chandra* X-ray Center in the application package CIAO. *XMM-Newton* is an ESA science mission with instruments and contributions directly funded by ESA Member States and the USA (NASA). This publication makes use of data products from Two Micron All Sky Survey, which is a joint project of the University of Massachusetts and the Infrared Processing and Analysis Center/California Institute of Technology, funded by the NASA and the National Science Foundation. The *Spitzer Space Telescope* is operated by the Jet Propulsion Laboratory, California Institute of Technology, under contract with the NASA.

Bibliography

Anders, E., Grevesse, N. 1989, Geochimica et Cosmochimica Acta, 53, 197

Baldi, A., Forman, W., Jones, C., et al. 2009 [arXiv:0904.2569]

Bellazzini, M., Correnti, M., Ferraro, F. R., et al. 2006, A&A, 446, L1

Bogdán, Á., Gilfanov, M., 2008, MNRAS, 388, 56

Coelho, P., Mendes de Oliveira, C. & Cid F. R. 2009, MNRAS, 396, 624

de Vaucouleurs, G. 1975, ApJS, 29, 193

Dickey, J. M., Lockman, F. J., 1990, ARA&A, 28, 215

Di Stefano, R., Kong, A. K. H., Greiner, J., et al. 2004, ApJ, 610, 247

Ferrarese, L., Mould, J. R., Stetson, P. B., et al. 2007, ApJ, 654, 186

Finugenov, A., Ruszkowski, M., Jones, C. et al. 2008, ApJ, 686, 911

Gilfanov, M. 2004, MNRAS, 349, 146

Gilfanov, M. & Bogdán, Á. 2010, Nature, 463, 924

Gregg, M. D., Ferguson, H. C., Minniti, D., et al. 2004, AJ, 127, 1441

Greiner, J. 2000, New Astronomy, 5, 137

Hillebrandt, W. & Niemeyer, J. C. 2000, ARA&A, 38, 191

Irwin, J. A., Sarazin, C. L. & Bregman, J. N. 2002, ApJ, 570, 152

Irwin, J. A., Athney, A. E. & Bregman, J. N. 2003, ApJ, 587, 356

Jarrett, T. H., Chester, T., Cutri, R., et al. 2003, AJ, 125, 525

Jensen, J. B., Tonry, J. L., Barris, B. J., et al. 2003, ApJ, 583, 712

Kent, S. M. 1992, ApJ, 387, 181

Kraft, R. P., Hardcastle, M. J., Sivakoff, G. R., et al. 2008, ApJ, 677, L97

Kunder, A. & Chaboyer, B. 2009, AJ, 137, 4478

Livio, M. 2000, Type Ia Supernovae, Theory and Cosmology. Eds.: J. C. Niemeyer and J. W. Truran, Cambridge University Press, 2000, 33

Macri, L. M. 2001, ApJ, 549, 721

Mateo, M. L. 1998, ARA&A, 36, 435

Mathews, W. G. & Brighenti, F. 2003, ARA&A, 41, 191

Olsen, K. A. G., Blum, R. D., Stephens, A. W., et al. 2006, AJ, 132, 271

Randall, S. W., Sarazin, C. L. & Irwin, J. A. 2004, ApJ, 600, 729

Revnivtsev, M., Sazonov, S., Gilfanov, M., et al. 2006, A&A, 452, 169

Revnivtsev, M., Churazov, E., Sazonov, S., et al. 2008, A&A, 490, 37

Sarazin, C. L., Irwin, J. A. & Bregman, J. N. 2001, ApJ, 556, 533

Sazonov, S., Revnivtsev, M., Gilfanov, M., et al. 2006, A&A, 450, 117

Sivakoff, G. R., Sarazin, C. L. & Irwin, J. A. 2003, ApJ, 599, 218

Stanek, K. Z., Garnavich, P. M., 1998, ApJ, 503, 131

Terlevich, A. I. & Forbes, D. A. 2002, MNRAS, 330, 547

Tonry, J. L., Dressler, A., Blakeslee, J. P., et al. 2001, ApJ, 546, 681

Voss, R. & Gilfanov, M. 2007, A&A, 468, 49

Whelan, J. & Iben, I. Jr. 1973, ApJ, 186, 1007

Chapter 4

Unresolved X-ray emission in M31 and constraints on progenitors of Classical Novae

Monthly Notices of the Royal Astronomical Society, in press, 2010

Bogdán, Á. & Gilfanov, M.

4.1 Abstract

We investigate unresolved X-ray emission from M31 based on an extensive set of archival *XMM-Newton* and *Chandra* data. We show that extended emission, found previously in the bulge and thought to be associated with a large number of faint compact sources, extends to the disk of the galaxy with similar X-ray to K-band luminosity ratio. We also detect excess X-ray emission associated with the 10-kpc star-forming ring. The L_X/SFR ratio in the $0.5-2$ keV band ranges from zero to $\approx 1.8\cdot10^{38}$ (erg s^{-1})/($M_\odot$/yr), excluding the regions near the minor axis of the galaxy where it is $\sim 1.5-2$ times higher. The latter is likely associated with warm ionized gas of the galactic wind rather than with the star-forming ring itself.

Based on this data, we constrain the nature of Classical Nova (CN) progenitors. We use the fact that hydrogen-rich material, required to trigger the explosion, accumulates on the white dwarf surface via accretion. Depending on the type of the system, the energy of accretion may be radiated at X-ray energies, thus contributing to the unresolved X-ray emission. Based on the CN rate in the bulge of M31 and its X-ray surface brightness, we show that no more than ~ 10 per cent of CNe can be produced in magnetic cataclysmic variables, the upper limit being ~ 3 per cent for parameters typical for CN progenitors. In dwarf novae, $\gtrsim 90-95$ per cent of the material must be accreted during outbursts, when the emission spectrum is soft, and only a small fraction in quiescent periods, characterized by rather hard spectra.

4.2 Introduction

Similarly to other normal galaxies, X-ray emission from the bulge of the Andromeda galaxy is dominated by accreting compact sources (e.g. Voss & Gilfanov, 2007). In addition, there is relatively bright extended emission which nature was explored in Bogdán & Gilfanov (2008) (hereafter Paper I) based on extensive set of *Chandra* observations. In Paper I we revealed the presence of warm ionized ISM in the bulge which most likely forms a galactic-scale outflow and showed that bulk of unresolved emission is associated with old stellar population, similar to the Galactic ridge X-ray emission in the Milky Way (Revnivtsev et al., 2006; Sazonov et al., 2006). Although these studies led to a much better understanding of X-ray emission from the bulge of M31, the disk of the galaxy could not be investigated in similar detail due to insufficient *Chandra* data coverage of the galaxy. The *XMM-Newton* data, available at the time, also did not provide adequate coverage of the galaxy either, with only the northern part of the disk observed with relatively short exposures (Trudolyubov et al., 2005).

Over the last several years *XMM-Newton* completed a survey of M31, which data has become publicly available now. The numerous pointings with total exposure time of ~ 1.5 Ms give a good coverage of the entire galaxy. With these data it has become possible to study X-ray emission from the disk of the galaxy. In the present paper we concentrate on the unresolved emission component and compare its characteristics in the disk and bulge. We will also study the 10-kpc star-forming ring to support our earlier claim that excess unresolved emission is associated with star-forming regions in the galactic disk (Paper I).

Classical Nova (CN) explosions are caused by thermonuclear runaway on the surface of a white dwarf in a binary system (Starrfield et al., 1972). In order for the nuclear runaway to start, a certain amount of hydrogen rich material, $\Delta M \sim 10^{-5} M_{\odot}$, needs to be accumulated on the white dwarf surface (Fujimoto, 1982). This material is supplied by the donor star and is accreted onto the white dwarf. Obviously, there is a direct relation between the frequency of CNe and collective accretion rate in their progenitors. The accretion energy is released in the form of electromagnetic radiation which spectrum depends on the type of the progenitor system. In certain types of accreting white dwarfs it peaks in the X-ray band, for example in magnetic systems – polars and intermediate polars. Emission from these systems will be contributing to the unresolved emission in the galaxy, therefore their number and contribution to the CN rate can be constrained using high resolution X-ray data. This is the subject of the second part of the paper.

In the following, the distance to M31 is assumed to be 780 kpc (Stanek & Garnavich, 1998; Macri, 1983) and the Galactic hydrogen column density is 6.7×10^{20} cm^{-2} (Dickey & Lockman, 1990).

The paper is structured as follows. In Section 4.3 we describe the analyzed X-ray and near-infrared data and the main steps of its reduction. In Section 4.4 results of the analysis of unresolved X-ray emission are presented. In Section 4.5 we derive constraints on the nature of CN progenitors. Our results are summarized in Section 4.6.

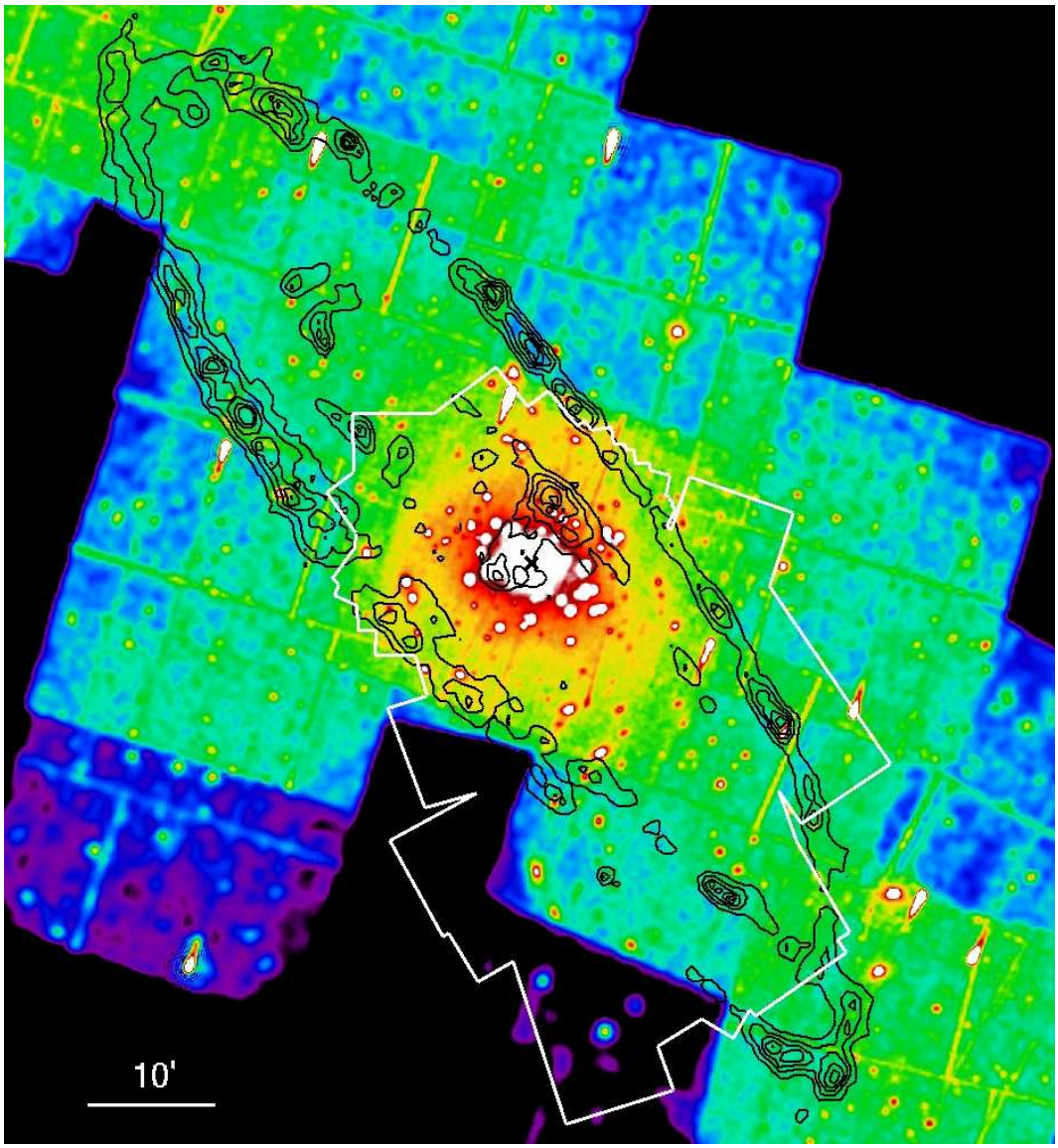

Figure 4.1: Combined raw image of *XMM-Newton* observations in the 0.5 – 2 keV energy band. Black contour show the location of the 10-kpc star-forming ring, traced by the 160 μm *Spitzer* image. The white contour marks the region covered by *Chandra*. The center of M31 is marked with the cross. North is up and east is left.

4.3 Data reduction

4.3.1 *XMM-Newton*

We analyzed 24 observations from *XMM-Newton* survey of M31, listed in Table 4.1. The data was taken between 2000 June 25 and 2007 July 25 and covers nearly the entire disk of M31 and its bulge. The approximate coverage of the galaxy by *XMM-Newton* data is illustrated in Figure 4.1. We analyzed the data of the European Photon Imaging Camera (EPIC) instruments (Strüder et al., 2001; Turner et al., 2001), for its reduction we used Science Analysis System (SAS) version 7.1.

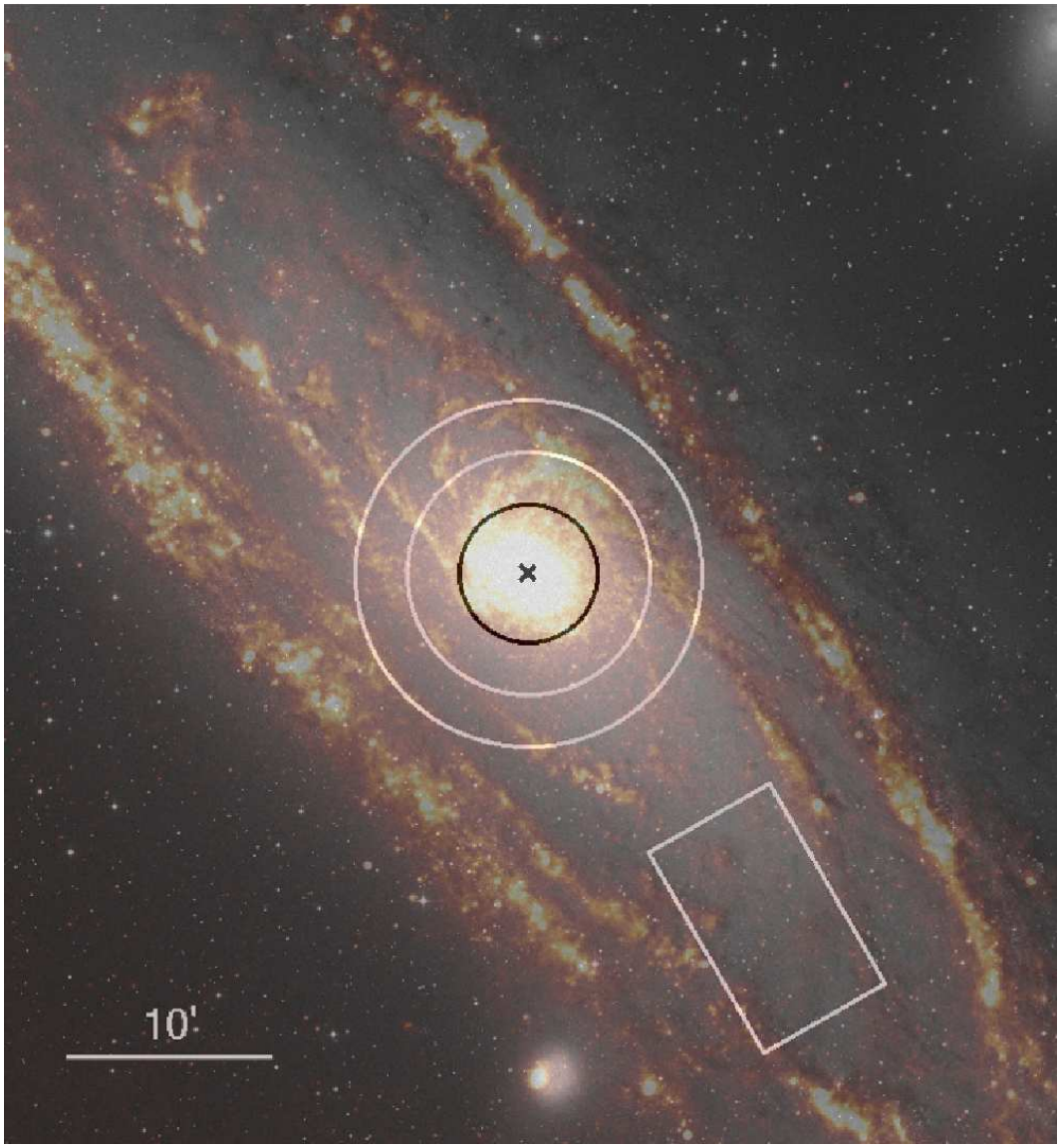

Figure 4.2: Composite image of M31 based on optical and far-infrared data. The *DSS* optical image (grey) represents the distribution of the stellar light. The 24 μm data of *Spitzer Space Telescope* (red) traces the distribution of cold gas and dust in spiral arms and in the 10-kpc star-forming ring. Overplotted are the regions used for spectral analysis in Section 4.4.2 and to compute the L_X/L_K ratios in Section 3. The center of M31 is marked with the cross. North is up and east is left.

Main steps of data analysis were performed in the same way as described in Paper I. After applying the double filtering technique (Nevalainen et al., 2005) the exposure time decreased to $T_{\rm filt} \approx 639$ ks. The out-of-time events were removed using the Oot event list. The exposure maps were calculated with EEXPMAP command of SAS, using a powerlaw model with slope of $\Gamma = 2$ The observations were re-projected and merged in the coordinate system of Obs-ID 0112570101.

In the analysis of extended emission, contribution of resolved point sources needs to be removed. For this, we used the *Chandra* source list, where available. In the disk, not covered by *Chandra*, we ran the SAS source detection tool, which gives a complete list of sources above $\sim 10^{36}$ erg s^{-1}. The resulting

Table 4.1: The list of *XMM-Newton* observations used for the analysis.

Obs-ID	$T_{\rm obs}$ (ks)	$T_{\rm filt}$ (ks)	Date
0109270101	62.5	16.0	2001 Jun 29
0109270301	54.2	25.2	2002 Jan 26
0109270401	91.6	32.2	2002 Jun 29
0109270701	54.9	53.7	2002 Jan 05
0112570101	61.1	52.6	2002 Jan 06
0112570201	62.8	42.6	2002 Jan 12
0112570301	59.9	15.2	2002 Jan 24
0112570401	31.0	25.0	2000 Jun 25
0202230201	18.3	17.8	2004 Jul 16
0202230401	14.6	9.0	2004 Jul 18
0202230501	21.8	2.0	2004 Jul 19
0402560301	66.7	33.9	2006 Jul 01
0402560401	57.0	5.0	2006 Jul 08
0402560501	57.0	24.0	2006 Jul 20
0402560701	64.4	14.0	2006 Jul 23
0402560801	64.0	41.0	2006 Dec 25
0402560901	60.0	33.6	2006 Dec 26
0402561001	63.6	39.7	2006 Dec 30
0402561101	60.0	32.0	2007 Jan 01
0402561301	52.1	25.1	2007 Jan 03
0402561401	62.0	40.0	2007 Jan 04
0402561501	54.9	36.9	2007 Jan 05
0404060201	40.0	14.0	2006 Jul 03
0410582001	20.1	8.0	2007 Jul 25

list was used to mask out compact sources in these regions. As before (Paper I), we use enlarged sources regions in order to limit the contribution of remaining counts from point sources to less than $\lesssim 10$ per cent.

The particle background components were subtracted as described in Paper I. By removal of the cosmic X-ray background (CXB) we took into account that the resolved fraction of CXB changes as the exposure time varies. In order to compensate for this effect we assumed that the point source detection sensitivity is proportional to the exposure time, and computed the resolved fraction of CXB for each pixel using $(\log N - \log S)$ distribution from Moretti et al. (2003). Such an approach does not account for the non-uniformity of the source detection sensitivity across the CCDs. This uncertainty is taken into account in computing systematic errors in the brightness profiles, along with other factors described in Paper I. Their combined effect is indicated by grey shaded area in the surface brightness profiles analyzed in the Section 4.4.1. Due to limitations of the background subtraction procedure, data can be analyzed and interpreted reliably only out to $\sim 1^\circ$ central distance along the major axis of M31 in the $0.5-2$ keV energy range. We found that in harder energy band only the bulge of the galaxy can be studied with *XMM-Newton* data.

Table 4.2: The list of *Chandra* observations used for the analysis.

Obs-ID	T_{obs} (ks)	T_{filt} (ks)	Instrument	Date
303	12.0	8.2	ACIS-I	1999 Oct 13
305	4.2	4.0	ACIS-I	1999 Dec 11
306	4.2	4.1	ACIS-I	1999 Dec 27
307	4.2	3.1	ACIS-I	2000 Jan 29
308	4.1	3.7	ACIS-I	2000 Feb 16
311	5.0	3.9	ACIS-I	2000 Jul 29
312	4.7	3.8	ACIS-I	2000 Aug 27
313	6.1	2.6	ACIS-S	2000 Sep 21
314	5.2	5.0	ACIS-S	2000 Oct 21
1575	38.2	38.2	ACIS-S	2001 Oct 05
1577	5.0	4.9	ACIS-I	2001 Aug 31
1580	5.1	4.8	ACIS-S	2000 Nov 17
1583	5.0	4.1	ACIS-I	2001 Jun 10
1585	5.0	4.1	ACIS-I	2001 Nov 19
2049	14.8	11.6	ACIS-S	2000 Nov 05
2050	13.2	10.9	ACIS-S	2001 Mar 08
2051	13.8	12.8	ACIS-S	2001 Jul 03
2895	4.9	3.2	ACIS-I	2001 Dec 07
2896	5.0	3.7	ACIS-I	2002 Feb 06
2897	5.0	4.1	ACIS-I	2002 Jan 08
2898	5.0	3.2	ACIS-I	2002 Jun 02
4360	5.0	3.4	ACIS-I	2002 Aug 11
4536	54.9	30.2	ACIS-S	2005 Mar 07
4678	4.9	2.7	ACIS-I	2003 Nov 09
4679	4.8	2.7	ACIS-I	2003 Nov 26
4680	5.2	3.2	ACIS-I	2003 Dec 27
4681	5.1	3.3	ACIS-I	2004 Jan 31
4682	4.9	1.2	ACIS-I	2004 May 23
7064	29.1	23.2	ACIS-I	2006 Dec 04
7068	9.6	7.7	ACIS-I	2007 Jun 02

4.3.2 *Chandra*

We combined an extensive set of *Chandra* data taken between 1999 October 13 and 2007 June 2, listed in Table 4.2. The data was processed with CIAO [1] software package tools (CIAO version 4.0; CALDB version 3.4.5). The 29 observations allowed us to study the bulge and the southern disk of M31, the exact data coverage is shown in Figure 4.1. In case of ACIS-S observations we used the data from S1, S2, S3,

[1] http://cxc.harvard.edu/ciao/

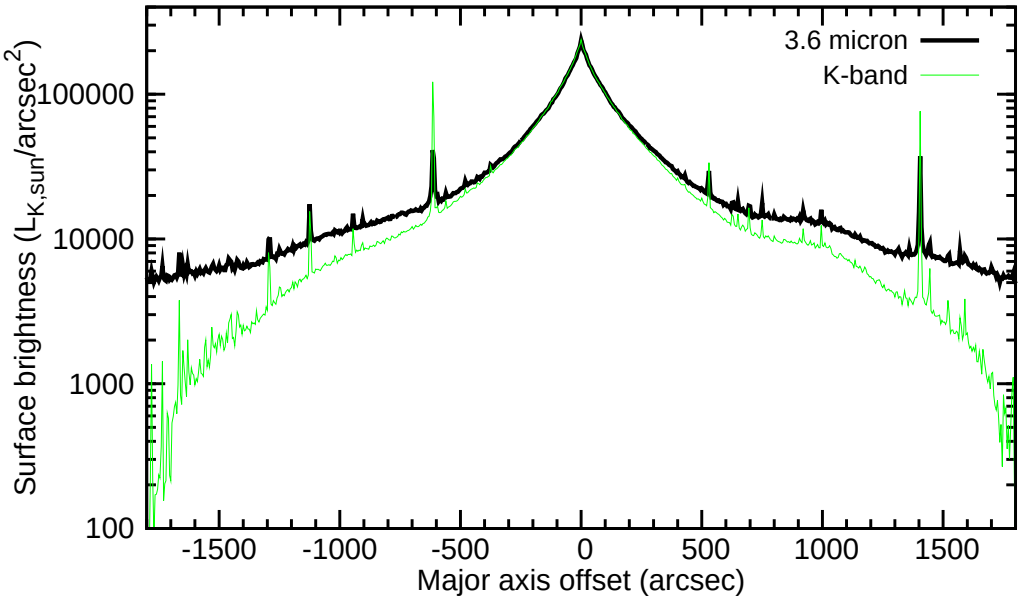

Figure 4.3: Near-infrared light distribution along the major axis of M31 based on 3.6 μm data of *Spitzer Space Telescope* (black thick line) and the *2MASS* K-band (thin green line) data. The normalization of *Spitzer* profile was adjusted to match the K-band light in the center of M31. The x-coordinate increases from south-west to north-east.

I2, I3 CCDs, except for Obs-ID 1575 where we extracted data only from the S3 chip. The peak value of the exposure time reaches $T_{filt} \approx 144$ ks in the center of the galaxy.

The main steps of the data analysis are similar to those outlined in Paper I. After excluding the flare-contaminated time intervals the total exposure time decreased by $\sim$ 25 per cent. The instrumental background was subtracted following Hickox & Markevitch (2006) and using the stowed data set[2]. By subtraction of CXB we followed the same procedure as described for *XMM-Newton*, to correct for the varying fraction of resolved CXB sources.

4.3.3 Near-infrared data

In order to compare the unresolved X-ray emission with the stellar mass distribution, a stellar mass tracer is needed. The K-band image from the *Two-Micron All Sky Survey* (*2MASS*) Large Galaxy Atlas (LGA) (Jarrett et al., 2003) image is commonly used for this purpose. Alternatively, one could use data of the Infrared Array Camera (IRAC) on the *Spitzer Space Telescope* (*SST*), which provides images at near-infrared wavelengths, among others at 3.6 μm.

Due to the large angular extent of M31 the background on the *2MASS* K-band image provided by LGA is somewhat oversubtracted (T. Jarrett, private communication), therefore the disk of M31 appears

[2]http://cxc.harvard.edu/contrib/maxim/stowed/

to be too faint. In Figure 4.3 we compare the K-band surface brightness distribution with the *Spitzer* 3.6 μm data. The profiles were extracted along the major axis of M31, with bin width of 5 arcsec and the bins were averaged on 500 arcsec in the transverse direction. The background level of *Spitzer* image was estimated using nearby fields to M31. There is a good agreement in the central $\sim$ 300 arcsec, where the background subtraction is nearly negligible, but at large offsets an increasing deviation appears. Therefore in the present study we use the 3.6 μm image of *Spitzer* to trace the stellar mass. In order to facilitate the comparison of results with other studies we converted *Spitzer* near-infrared luminosities to K-band values using the central regions of the galaxy. The obtained conversion factor between pixel units is $C_K/C_{3.6\,\mu\mathrm{m}} \approx 10.4$.

In Paper I we used 2MASS image to compute K-band luminosities and stellar masses of different parts of the galaxy. As the analysis of the Paper I did not extend beyond $\approx$ 1000 arcsec from the center, the deficiency of the 2MASS image at large offset angles has not affected our results in any significant or qualitative way. It resulted, however, in small quantitative difference in X/K ratios between this paper and Paper I.

4.4 Unresolved X-ray emission in M31

4.4.1 Surface brightness distribution

We study the brightness distribution of unresolved X-ray emission in M31 in the 0.5 – 2 keV and in the 2 – 7 keV energy range (Figure 4.4, 4.5). In all cases profiles were averaged over 500 arcsec in the transverse direction. The contribution of resolved point sources is removed. The profiles are corrected for vignetting, furthermore all instrumental and sky background components are subtracted. We found good agreement at all studied distances between *Chandra* and *XMM-Newton* data. In the inner bulge region, which is most crowded with point sources we consider only *Chandra* data. X-ray light distributions are compared with the 3.6 μm *Spitzer* data.

The upper panel of Figure 4.4 presents the surface brightness distribution along the major axis of M31 in the 0.5 – 2 keV band. The shaded area shows the background subtraction uncertainties. The profile confirms the presence of the additional soft emission in the central bulge, which was shown to originate from hot ionized gas (see Paper I). Outside few central bins X-ray flux follows the near infrared profile – unresolved emission associated with the bulge of the galaxy continues into the disk with approximately the same X-ray to K-band ratio. Although overall correlation between X-ray and near infrared brightness is quite good, there are several deviations, of which the most prominent is the excess X-ray emission at the central distance of -2500 arcsec. This excess approximately coincides with the broad hump on the 160 μm profile corresponding to the southern end of the 10-kpc star-forming ring (Figure 4.2). Similar excess emission ("shoulders" at $\sim \pm 700$ arcsec) coinciding with the peaks on the 160 μm profiles is present in the distribution along the minor axis. (Note that overall normalization of the X-ray flux is larger on the minor axis profile due to contribution of the gas emission.) A possible association of excess X-ray emission with the star-forming activity in the 10-kpc star-forming ring is further discussed in Section 4.4.4.

In Figure 4.5 we show the brightness distribution in the 2 – 7 keV energy band based on *Chandra*

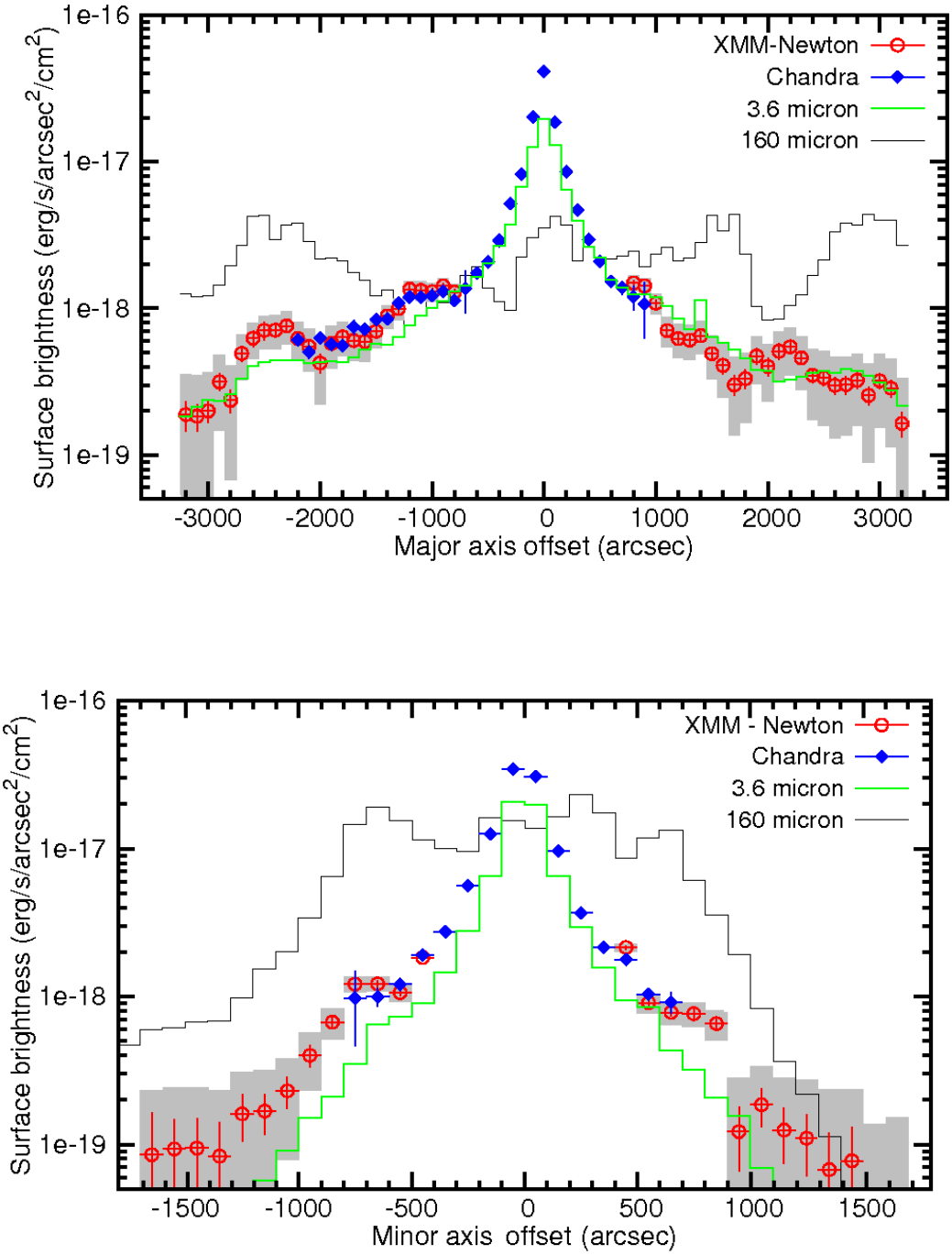

Figure 4.4: X-ray surface brightness distribution along the major axis (upper panel) and minor axis (lower) in the 0.5 – 2 keV energy band. The filled (blue) symbols show the *Chandra* data, open (red) symbols represent the *XMM-Newton* data, the solid (green) histogram is the surface brightness of 3.6 μm *Spitzer* data, the thin solid (black) line indicates 160 μm *Spitzer* data. The shaded area corresponds to the systematic uncertainty in the background subtraction for the *XMM-Newton* data. The normalization of the near- and far-infrared profiles are the same on both panels. The x-coordinate increases from south-west to north-east for the major axis and from south-east to north-west for the minor axis profile.

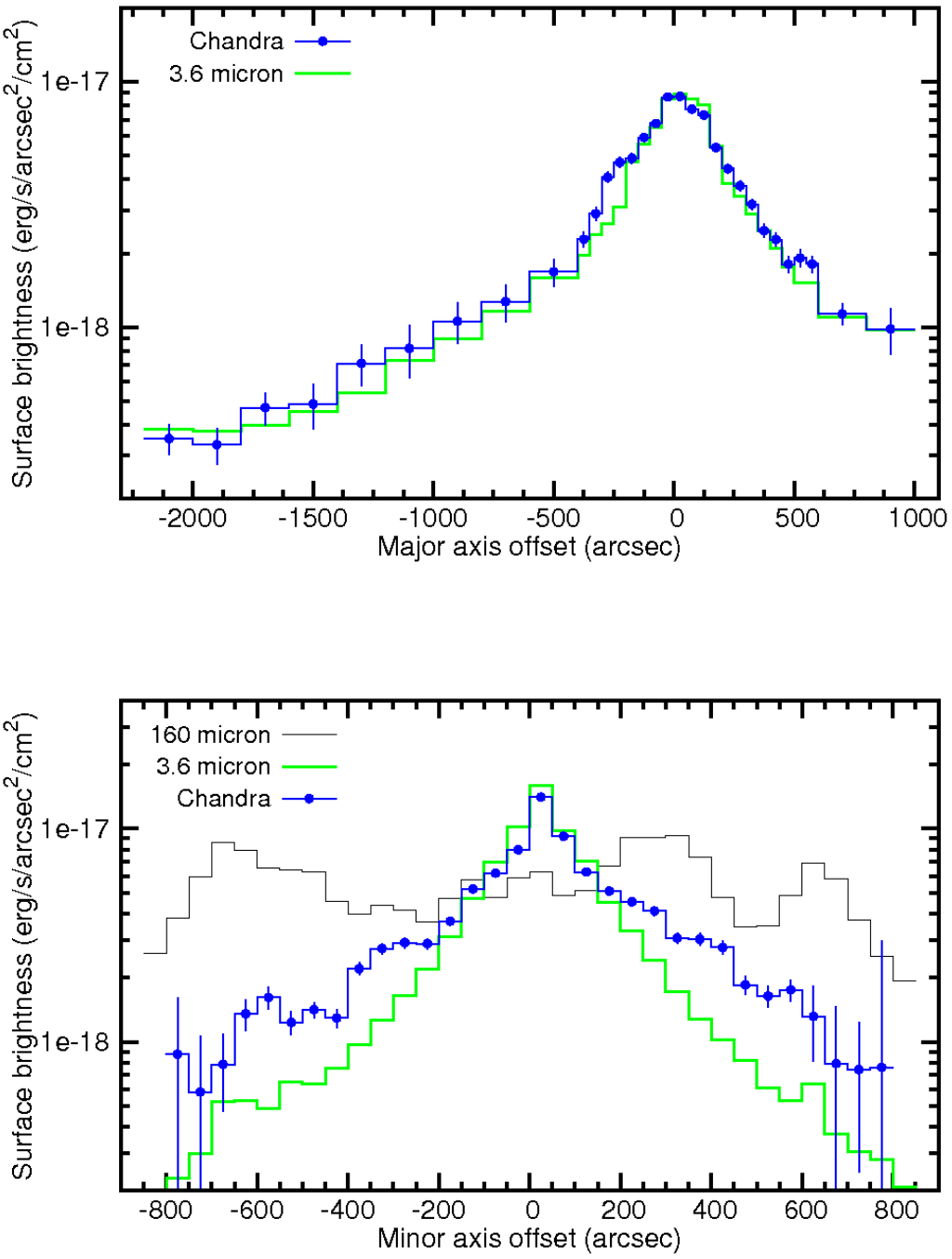

Figure 4.5: Same as Figure 4.4 but in the 2 – 7 keV energy band based on *Chandra* data. The normalization of the near-infrared profiles is the same on both panels.

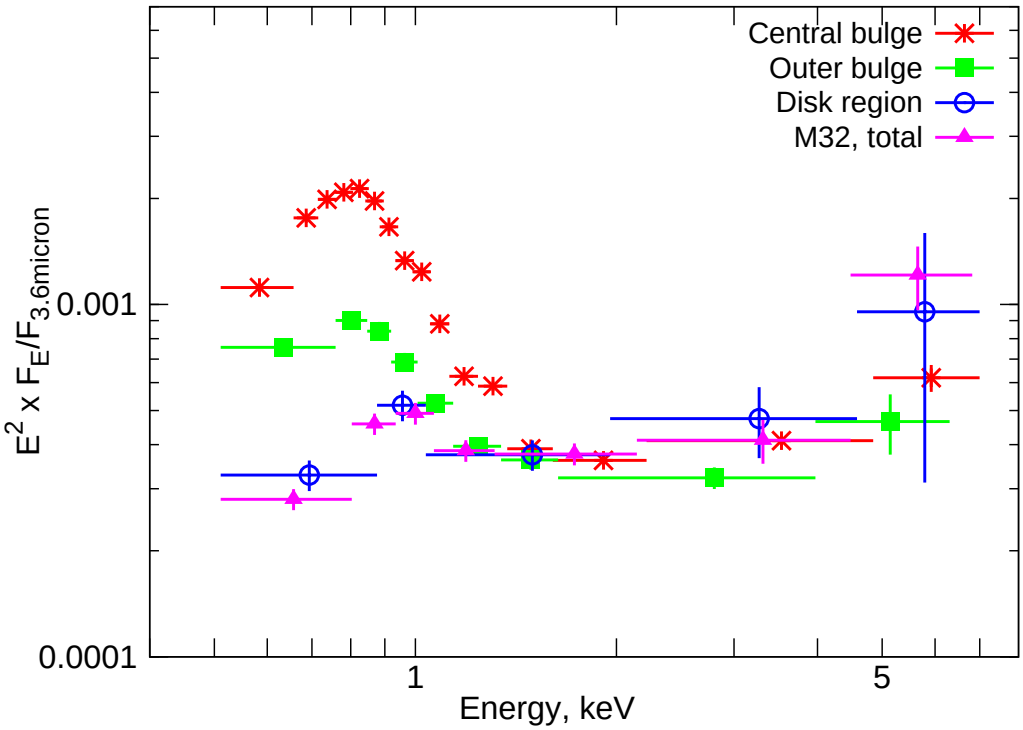

Figure 4.6: X-ray spectra of different regions in M31 and in M32: stars (red) show the spectrum of the central 200 arcsec region; filled boxes (green) are the spectrum of the 350−500 arcsec annulus; open circles (blue) are the spectrum of the disk; filled triangles (purple) show the spectrum of M32. All spectra were extracted using *Chandra* data. The spectra are normalized to the same level of near-infrared brightness.

data. No contribution of the hot gas emission with $kT \sim 300 - 400$ eV is expected in this energy range. Accordingly, there is a good agreement between the X-ray and near-infrared distribution along the major axis (Figure 4.5). However, along the minor axis the unresolved X-ray emission traces the stellar light only in the inner region. Outside $\sim 200 - 300$ arcsec the X-ray brightness becomes systematically larger than the normalized 3.6 μm distribution. The origin of this enhancement is not clear. It may be associated with the star-formation activity in the disk and 10-kpc star-forming ring, as suggested in Paper I, or may be related to the galactic scale wind.

4.4.2 Spectra

In order to extract spectra of the bulge and the disk of M31 we used only *Chandra* data. The background was subtracted using the ACIS "blank-sky" files as described in Paper I. We extracted the spectrum of the inner bulge, outer bulge, and disk of M31. The inner bulge region is represented by a circle with 200 arcsec radius, the outer bulge spectrum is extracted from a circular annuli with radii of 350 – 500 arcsec, and the disk spectrum is computed from a rectangular region at the southern part of the disk. The applied regions are also depicted in Figure 4.2. As a comparison we also added M32, the the extracted region is same as described in Paper I. In order to compare the spectra we normalized them to the same level of near-infrared luminosity.

Figure 4.6 reveals that all spectra are consistent above $\sim$ 1.5 keV. Below this energy the inner bulge region is strikingly different, it has a factor of $\sim$ 4 times stronger soft component than all other spectra. Also the outer bulge has a weak excess below $\sim$ 1 keV compared to the disk and M31 spectra, which show very similar spectral characteristics at all energies. The remarkable soft component is the consequence of the hot ionized gas, located in the bulge of M31 (see Paper I). The somewhat increased soft emission in the outer bulge is presumably due to the contribution from gas emission, lacking completely in the disk of the galaxy. Note the presence of the relatively weak soft component in the spectra of the disk region and M32, which presumably originates from the population of unresolved sources. Indeed, the different nature of the soft components in the inner bulge and in the disk of M31 is also supported by the best-fit temperatures to the soft components. Using a simple two component spectral model, consisting of an optically-thin thermal plasma emission spectrum and a power-law model (MEKAL in XSPEC), we find a best-fit temperature of $kT = 0.36 \pm 0.01$ keV for the inner bulge, whereas we obtain $kT = 0.62 \pm 0.10$ keV in the disk and $kT = 0.54 \pm 0.15$ keV in M32.

4.4.3 L_X/L_K ratios

The X-ray to K-band luminosity ratios (L_X/L_K) were computed for the same regions as used for spectral analysis. As before, we use *Chandra* data only. The L_X/L_K ratios are obtained in the $0.5-2$ keV and in the $2-10$ keV energy range to facilitate comparison with previous studies. The X-ray luminosities in the $0.5-2$ keV energy range were computed using the best fit spectral models. For the outer bulge and disk we assumed a "power law + MEKAL" model, whereas for the inner bulge a second MEKAL component was added to obtain a better fit. In the $2-10$ keV band the X-ray luminosities were computed from the count rate using the count-to-erg conversion factor for a power law spectrum with a photon index of $\Gamma = 2$. The conversion factor depends weakly on the assumed slope, changing by $\lesssim 10$ per cent when Γ varied by ± 0.4. The luminosities and their ratios are listed in Table 4.3, errors correspond to statistical uncertainties in the X-ray count rates.

The L_X/L_K ratios for the bulge regions are consistent with those given in Paper I, albeit somewhat smaller, due to the increased K-band luminosity for some of the regions (Section 4.3.3). In agreement with spectra, the L_X/L_K ratio in the soft band is highest in the inner bulge, and smallest in the disk of the galaxy, where it is consistent with M32 value (Paper I). In the outer bulge the obtained L_X/L_K ratio is in-between due to residual contribution from gas emission. In the hard band all L_X/L_K ratios are similar to each other, in the range of $(3.4-4.5)\cdot 10^{27}$ erg s^{-1} L$_{\rm K,\odot}^{-1}$. There is a statistically significant scatter

Table 4.3: X-ray to K-band luminosity ratios for different regions of M31 and for M32.

Region	L_K (L$_{\rm K,\odot}$)	$L_{0.5-2keV}$ (erg s^{-1})	$L_{2-10keV}$ (erg s^{-1})	$L_{0.5-2keV}/L_K$ (erg s^{-1} L$_{\rm K,\odot}^{-1}$)	$L_{2-10keV}/L_K$ (erg s^{-1} L$_{\rm K,\odot}^{-1}$)
Inner bulge	$1.9\cdot 10^{10}$	$1.7\cdot 10^{38}$	$8.0\cdot 10^{37}$	$(8.9\pm 0.1)\cdot 10^{27}$	$(4.2\pm 0.1)\cdot 10^{27}$
Outer bulge	$8.2\cdot 10^{9}$	$4.1\cdot 10^{37}$	$2.9\cdot 10^{37}$	$(5.0\pm 0.1)\cdot 10^{27}$	$(3.4\pm 0.1)\cdot 10^{27}$
Disk	$2.1\cdot 10^{9}$	$7.6\cdot 10^{36}$	$9.4\cdot 10^{36}$	$(3.6\pm 0.1)\cdot 10^{27}$	$(4.5\pm 0.2)\cdot 10^{27}$
M32	$8.5\cdot 10^{8}$	$3.0\cdot 10^{36}$	$3.4\cdot 10^{36}$	$(3.5\pm 0.1)\cdot 10^{36}$	$(4.0\pm 0.2)\cdot 10^{36}$

in their values, which origin is not clear. It can not be explained by the varying residual contribution of LMXBs due to different point source detection sensitivity in different region. Indeed, the latter varies from $\sim 2 \cdot 10^{35}$ erg s^{-1} in the outer bulge to $\sim 6 \cdot 10^{35}$ erg s^{-1} in the disk. If we use the luminosity function of LMXBs of Gilfanov (2004) and assume a powerlaw spectrum with slope of $\Gamma = 1.56$ as average LMXB spectrum (Irwin et al., 2003), we find that LMXBs in the luminosity range of $(2-6)\cdot 10^{35}$ erg s^{-1} contribute $L_X/L_K \sim 3\cdot 10^{26}$ erg s^{-1} L$_{\rm K,\odot}^{-1}$, which may account only for $\sim 1/4$ of the scatter. Further contribution to the observed difference in L_X/L_K ratios may be made by the difference in star-formation history of different regions. This may be an interesting topic on its own, but it is beyond the scope of this paper.

4.4.4 Emission from the 10-kpc star-forming ring

Surface brightness profiles suggest that there may be additional emission component associated with spiral arms and the 10-kpc star-forming ring. In order to study this further, we consider X-ray emission along the 10-kpc star-forming ring of the galaxy and investigate the behavior of the L_X/SFR(star formation rate) ratio. We use *XMM-Newton* data since only they provide good coverage of the star-forming ring with adequate sensitivity. Due to uncertainties in the background subtraction procedure in the hard energy band, we restrict this study to 0.5–2 keV range. The X-ray luminosity was computed in the same way as described in Section 4.4.1. The contribution of unresolved emission associated with old stellar population was removed based on the near-infrared luminosity of studied regions and using the L_X/L_K ratio of the disk of M31. The remaining X-ray emission is $25-50$ per cent of of the original value. The star-formation rate was determined based from 160 μm image of the galaxy provided by *Spitzer*. The background level for the latter was determined from a combination of nearby blank sky fields. The star-formation rate was computed from the 160μ flux using the infrared spectral fits from Gordon et al. (2006) and calibration of Kennicutt (1998). This resulted to a conversion coefficient of SFR = $9.5 \cdot 10^{-5}$ F$_{160\mu\rm m}$/Jy M$_\odot$yr^{-1} for the distance of M31.

The behavior of X/SFR ratio along the 10-kpc star-forming ring is shown in Figure 4.7. No excess X-ray emission above the level corresponding to the L_X/L_K ratio for the disk was detected in the northern (the position angle of $\sim 10^\circ$) and southern ($\sim 215^\circ$) parts of the ring. We therefore plot upper limits for these two regions, which were assumed to be 20 per cent of the X-ray emission associated with old stellar population. The X/SFR ratio is largest in the bins centered at the position angle of $\approx 90^\circ$ and $\approx 270^\circ$ corresponding to the minor axis of the galaxy. These bins are contaminated by the gas emission as it is obvious from the minor axis soft band profile shown in Figure 4.4. Apart from these bins, Figure 4.7 clearly demonstrates presence of the excess unresolved emission approximately correlated with the far-infrared luminosity. This emission presumably arises from a multitude of faint sources associated with young stellar objects (protostars and pre-main-sequence stars) and young stars (e.g. Koyama et al., 1996).

After the bins contaminated by the gas emission are excluded, a significant scatter in the obtained L_X/SFR values remains; they are in the range $(0.9 - 1.8) \cdot 10^{38}$ (erg s^{-1})/(M$_\odot$/yr). These variations may be intrinsic, due to the different star-formation history and population age in different parts of the 10-kpc star-forming ring (Shtykovskiy & Gilfanov, 2005), or may be caused by varying column density which can be as large as few times 10^{21} cm^{-2} (Nieten et al., 2006). Data in the hard band, unaffected by absorption,

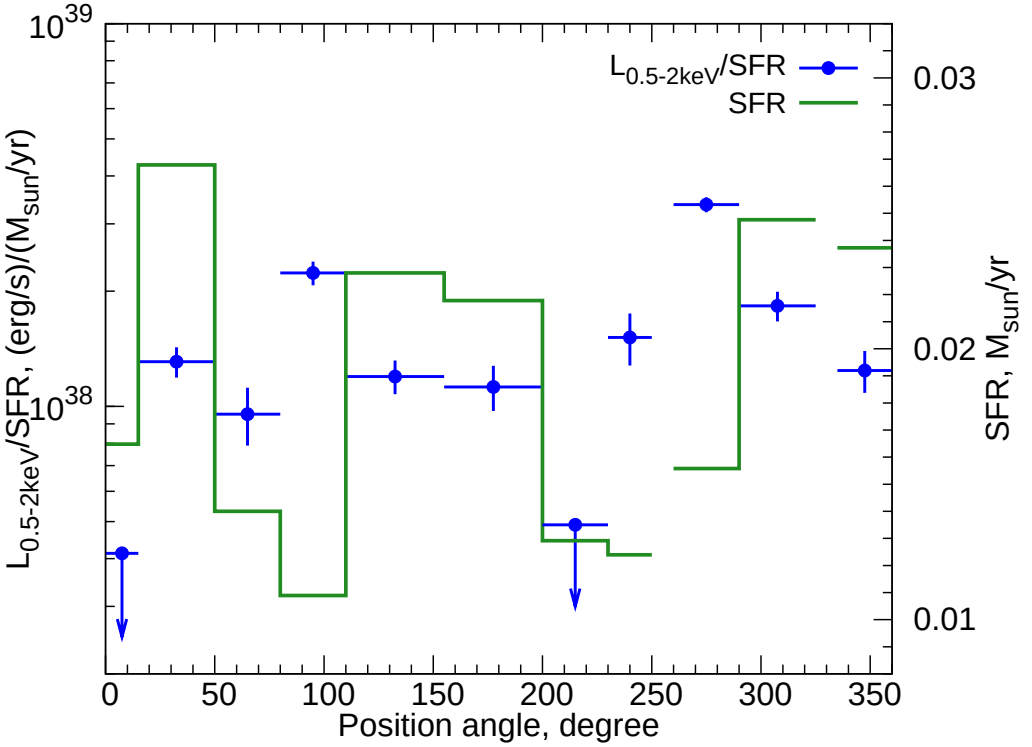

Figure 4.7: The X/SFR ratio along the 10-kpc star-forming (filled circles with error bars). The position angle increases clockwise and its zero point is at the northern side of the galaxy along its major axis. The bins centered at ≈ 90° and ≈ 270° approximately correspond to the minor axis of the galaxy. The solid histogram shows the star formation rate in the same regions (right hand *y*-axis). In the bins located at ≈ 10° and ≈ 215° we give upper limits on the X/SFR ratio. No X-ray data with sufficient exposure time was available at position angles of ≈ 250° and ≈ 330°.

could discriminate between these two possibilities. To this end, extensive *Chandra* observations of the 10-kpc star-forming ring would be instrumental.

4.5 Progenitors of classical novae in M31

4.5.1 X-ray emission from progenitors of Classical Novae

Classical Novae (CNe) are nuclear explosions occurring upon accumulation of critical mass of hydrogen-rich material on the surface of an accreting white dwarf. The frequency of these events in a galaxy depends on the rate at which matter accretes onto white dwarfs, hence it can be related to their luminosity. Indeed, the accretion energy (bolometric) released between two successive CN outbursts is:

$$\Delta E_{accr} = \frac{G M_{WD} \Delta M}{R_{WD}} \tag{4.1}$$

where $\Delta M(M_{WD}, \dot{M})$ is the mass of hydrogen-rich material needed to trigger a CN explosion (Yaron et al., 2005), M_{WD} and R_{WD} are the mass and radius of the white dwarf. For parameters believed to be typical for CN progenitors (M_{WD} = 1 $M_\odot$ and $\dot{M} = 10^{-9}$ $M_\odot$/yr) $\Delta M = 4.66 \cdot 10^{-5}$ $M_\odot$ and total accretion energy

released by an accreting white dwarf between two CN explosions is $\Delta E_{accr} \sim 2 \cdot 10^{46}$ ergs. If the frequency of CN events in a galaxy is given by ν_{CN}, the total accretion luminosity due to CN progenitors is

$$L_{accr} = \Delta E_{accr} \times \nu_{CN} \ . \tag{4.2}$$

Dependence of the accretion luminosity on the mass of the white dwarf and accretion rate is shown in Figure 4.2. In computing this curve we used the white dwarf mass-radius relation of Panei et al. (2000) for a zero temperature carbon white dwarf and $\Delta M(M_{WD}, \dot{M})$ dependence from Yaron et al. (2005).

The energy of accretion is radiated in the optical, ultraviolet or X-ray bands, depending on the type of the progenitor system. In magnetic systems (polars and intermediate polars) and dwarf novae in quiescence it is emitted predominantly in the X-ray band. Moreover, their X-ray spectra are relatively hard and their emission is therefore essentially unaffected by the interstellar absorption. X-ray radiation from these objects will contribute to unresolved emission from a galaxy. Therefore, comparing theoretical predictions with the surface brightness of unresolved emission one can constrain their contribution to the observed CN rate in galaxies. Derivation of such upper limits based on M31 data is the goal of this section.

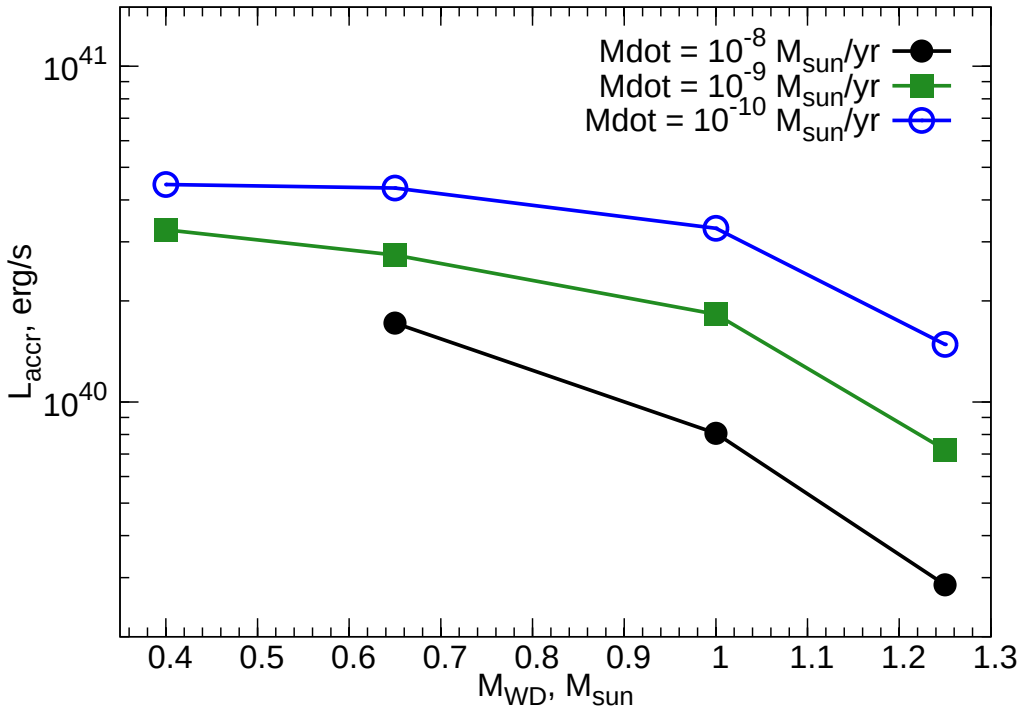

Figure 4.8: The bolometric luminosity of accreting white dwarfs – progenitors of Classical Novae in a galaxy with CN rate of $\nu_{CN} = 25$ per year. The curves show dependence of L_{accr} on the white dwarf mass for several values of the mass accretion rate.

4.5.2 Classical Novae and resolved X-ray sources and unresolved emission in the bulge of M31

The CN frequency in the bulge of M31 is 25 ± 4 (Shafter & Irby, 2001) (see also Arp, 1956). The number of progenitors required to maintain this rate is:

$$N \sim \frac{\Delta M}{\dot{M}} \nu_{CN}$$

Typical CN progenitors have accretion rate in the range of $\sim 10^{-10} - 10^{-8}$ $M_\odot$/yr (Puebla et al., 2007) and white dwarf masses of $0.65 - 1$ $M_\odot$ (Ritter & Kolb, 2003). Correspondingly, the number of CN progenitors is in the range of $\sim 2 \cdot 10^3 - 2 \cdot 10^6$, where the smaller number corresponds to the more massive white dwarfs and larger accretion rates. This exceeds significantly the number of bright resolved sources in the bulge of M31, ~ 300. The latter also includes low-mass X-ray binaries – excluding them the number of potential bright CN progenitors is yet smaller. We therefore conclude that the majority of CN progenitors can not be among bright point sources, rather they are part of the unresolved X-ray emission.

To measure the latter, we define the bulge as an elliptical region with 12 arcmin major axis, with axis ratio of 0.47 and with position angle of 45°. The total K-band luminosity of the studied region is $L_K = 4.2 \cdot 10^{10}$ $L_\odot$. We use *Chandra* data, described in the previous sections, to obtain the unresolved X-ray luminosity in the $2 - 10$ keV energy range. The advantage of this energy band is that it is not polluted by hot ionized gas (Section 4.4.2). We find a total luminosity of the unresolved component of $L_{2-10keV} = (1.6 \pm 0.1) \cdot 10^{38}$ erg s^{-1} in this region. Obviously, this value presents only an upper limit on the luminosity from the population of accreting white dwarfs, as other type of X-ray emitting sources may also contribute. To this end we use results of Sazonov et al. (2006), who studied the population of faint X-ray sources in the Solar neighborhood and found that accreting white dwarfs contribute $\sim 1/3$ of the total luminosity in the 2–10 keV band. As M31 demonstrates similar X/K ratio, we extrapolate this result to the bulge of M31 and estimate the luminosity of CVs of $L_{CV,2-10keV} = (5.7 \pm 0.3) \cdot 10^{37}$ erg s^{-1}.

4.5.3 Magnetic cataclysmic variables

Upper limit on the contribution of magnetic systems to the CN rate

Polars (AM Her systems) and intermediate polars (IPs) are accreting binary systems in which the accretion disk is partly (IPs) or entirely (AM Her systems) disrupted by magnetic field of the white dwarf. These systems are sources of relatively hard X-ray emission produced via optically-thin bremsstrahlung in an accretion shock near the white dwarf surface. They also may have a prominent soft component generated by the white dwarf surface illuminated by hard X-rays. Theory predicts (Lamb & Masters, 1979; King & Lasota, 1979) and observations confirm (Ramsay & Cropper, 2004) that the soft component account for $\sim 1/2$ of the total accretion luminosity of polars. Intermediate polars may also have a soft component in their spectra of somewhat smaller luminosity, $\sim 1/3$ of the total (Evans & Hellier, 2007). Correspondingly, we assume in the following calculations, that $1/2$ of the accretion luminosity of magnetic CVs is emitted in the hard X-ray component. To the first approximation, the bremsstrahlung temperature of this component is defined by the depth of the gravitational component on the white dwarf surface, the ob-

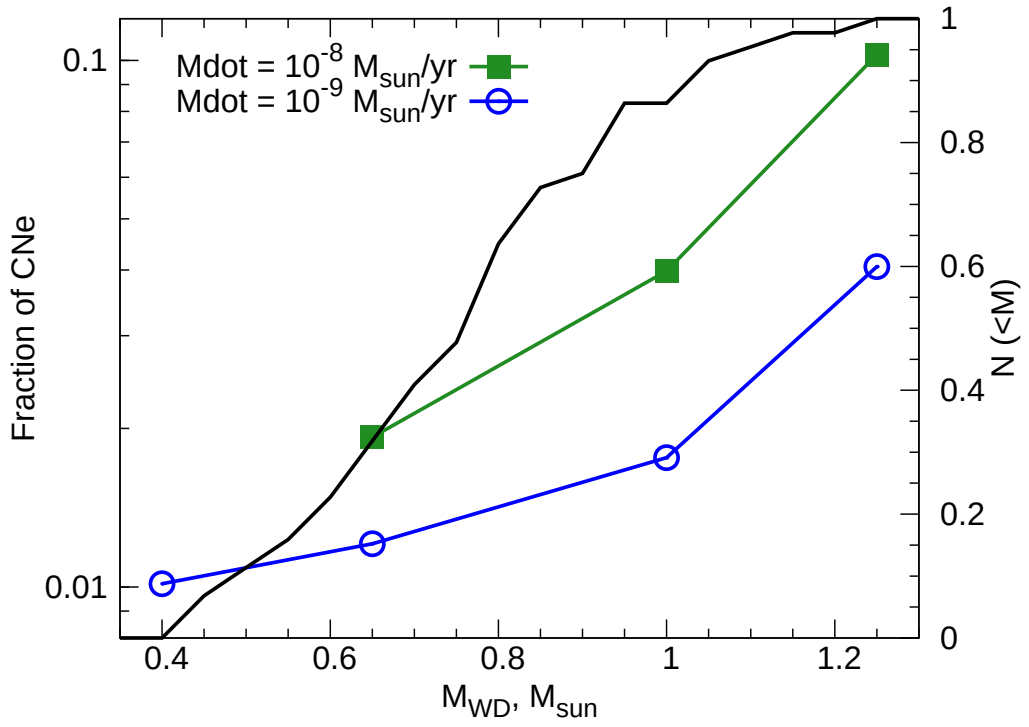

Figure 4.9: The upper limit of the contribution of magnetic systems to the CN frequency. The filled squares (green in the color version of this plot) correspond to an accretion rate of 10^{-8} $M_\odot$/yr, while the empty circles (blue) assumes an accretion rate of 10^{-9} $M_\odot$/yr. The solid line (black) shows the cumulative distribution of white dwarf masses in magnetic CVs (right hand *y*-axis), see text for references. Note, that 85 per cent of white dwarfs is less massive than 1 $M_\odot$.

served values showing considerable dispersion. For a large sample of magnetic white dwarfs (Landi et al., 2009; Brunschweiger et al., 2009) we calculate the average value of $kT \approx 23$ keV with the standard deviation of ≈ 9 keV. In the following calculations we assume $kT = 23$ keV and ignore the dependence of the temperature on the white dwarf mass. As demonstrated below this particular choice does not influence our results significantly.

In order to constrain the contribution of magnetic CVs to the CN frequency we compute their predicted X-ray luminosity assuming that CNe are exclusively produced in such systems. In this calculation we assume that the presence of strong magnetic fields does not influence the characteristics of nuclear burning and results of Yaron et al. (2005) for the mass of the hydrogen layer $\Delta M(\dot{M}, M_{WD})$ apply. The total accretion luminosity predicted by equation (4.2) is halved (see above), corrected for interstellar absorption, and converted into the 2–10 keV energy band. The obtained value is then compared with the observed luminosity of the unresolved emission, corrected for the contribution of accreting white dwarfs, as described before. The upper limit on the contribution of magnetic systems in the CN rate in M31 is shown in Figure 4.9. It shows that allowing all possible values of the white dwarf mass, no more than ≈ 10 per cent of CNe can be produced in magnetic systems. The less constraining value of the upper limit corresponds to the largest accretion rate and most massive white dwarfs. However, the combination of these extreme parameters is not typical for magnetic CVs as illustrated by the cumulative distribution of the white dwarf

mass in magnetic systems (Ritter & Kolb, 2003; Suleimanov et al., 2005; Brunschweiger et al., 2009). The distribution shows that ≈ 85 per cent of white dwarfs are less massive than 1 $M_\odot$. Furthermore the average accretion rate in these systems is fairly low, $\dot{M} \sim 1.8 \cdot 10^{-9}$ $M_\odot$/yr (Suleimanov et al., 2005). We conclude therefore that a more realistic upper limit should be ≈ 3 per cent, corresponding to $M_{WD} = 1$ $M_\odot$ and $\dot{M} = 10^{-9}$ $M_\odot$/yr.

This result weakly depends on the assumed temperature of bremsstrahlung spectrum. If $kT = 40$ keV is assumed, the upper limit becomes ≈ 4 per cent. Only unrealisticly large temperature of $kT = 75$ keV would lead to a two times larger upper limit.

Comparison with statistics of observed CNe from magnetic systems

Ritter & Kolb (2003) find that ∼ 1/3 of CNe, with known progenitors, are produced in CVs possessing a magnetic white dwarf (Table 4.4). Although this catalogue is not complete neither in the volume nor in the brightness limited sense, the ∼ 10 times discrepancy appears to be too large to be consistent with our upper limit of ≈ 3 per cent. In another study, Araujo-Betancor (2005) investigated the space density of magnetic and non-magnetic CVs, and obtained that ∼ 22 per cent of all CVs are magnetic. This number also seems to be in conflict with our upper limits. As demonstrated below, these two discrepancies are caused by the single reason – by an order of magnitude difference in mass accretion rate between magnetic and non-magnetic system.

Indeed, the average accretion rate in magnetic CVs is $\sim 1.8 \cdot 10^{-9}$ $M_\odot$/yr (Suleimanov et al., 2005), whereas for non-magnetic CNe it is $\sim 1.3 \cdot 10^{-8}$ $M_\odot$/yr (Puebla et al., 2007). The obvious consequence of this difference is that in magnetic systems it takes longer to accrete the same amount of material needed to trigger the nova explosion. Moreover, at lower accretion rates ΔM is larger by a factor of $\sim 1.5 - 2$ (Yaron et al., 2005). The consequence of these effects is that magnetic CVs undergo CN outburst ∼ 10 times less frequently. This explains the second discrepancy – between the observed fraction of magnetic CVs and our upper limit on their contribution to the CN frequency.

Another consequence of the smaller accretion rate is that Classical nova explosions are brighter in magnetic systems, therefore they can be observed at larger distances and are sampled from larger volume than CNe from non-magnetic progenitors. This explains the first discrepancy – seemingly too large fraction of CN events which progenitors are magnetic systems. To verify this, we selected CNe with known progenitors from the catalogue of Ritter & Kolb (2003) and searched for distances in the literature. In total, we collected 32 CNe, of which 11 are from magnetic progenitors (Table 4.4). Their distance distributions are shown in Figure 4.10. Obviously, magnetic systems are located at larger distances: the average distance is ≈ 6.6 kpc and ≈ 2.2 kpc for magnetic and non-magnetic CNe. Below 1 kpc almost four times more non-magnetic CNe are observed (the normalized number of magnetic systems is ≈ 1.9 and 8 for non-magnetic), whereas above ≈ 5 kpc there are more magnetic CVs (≈ 11.4 vs 3). The difference between two distributions is statistically significant, with the K-S probability of ≈ 0.008.

The difference in the distance can be compared with the prediction based on the expected brightness at the maximum of the lightcurve. Calculations of Yaron et al. (2005) show that for 0.65 $M_\odot$ white dwarf the maximum brightness achieved during the CN explosion will differ by ≈ 1 magnitude, the difference being

Table 4.4: The list of magnetic and non-magnetic Galactic CNe, classification is taken from Ritter & Kolb (2003) unless otherwise noted.

Name	CV classification	Distance, pc
V603 Aql	SH	400[a]
V1425 Aql	NL	2700[b]
OY Ara	SW	1500[a]
RS Car	SH	2100[a]
V842 Cen	NL	500[a]
RR Cha	SH	6100[a]
V1500 Cyg	AM⋆	1300[a]
V1974 Cyg	SH	1700[a]
V2275 Cyg	IP	5500[c]
V2467 Cyg	NL	3100[d]
DM Gem	SW	4700[a]
DQ Her	DQ	525[e]
V446 Her	DN	1300[a]
V533 Her	DQ	1300[a]
DK Lac	VY	3900[a]
BT Mon	SW	1000[a]
GI Mon	IP	4600[a]
GQ Mus	AM	5100[a]
GK Per	DN	500[a]
V Per	NL	1000[a]
RR Pic	SW	500[a]
CP Pup	SH	900[a]
HZ Pup	NL	5800[a]
V597 Pup	IP⋆	10300[f]
T Pyx	SS	2500[a]
V697 Sco	IP	16100[a]
V373 Sct	IP	4600[a]
WY Sge	DN	2000[a]
V630 Sgr	SH	600[a]
V1017 Sgr	DN	2600[a]
V4633 Sgr	AM⋆	9000[g]
V4745 Sgr	IP	14000[h]

⋆ The classification for V1500 Cyg, V597 Pup and V4633 Sgr was taken from Stockman et al. (1988) Warner & Woudt (2009) and Lipkin et al. (2001), respectively.

References are from: [a] Shafter (1997) – [b] Kamath et al. (1997) – [c] Kiss et al. (2002) – [d] Poggiani (2009) – [e] Vaytet et al. (2007) – [f] Naik et al. (2009) – [g] Lipkin et al. (2001) – [h] Csák et al. (2005)

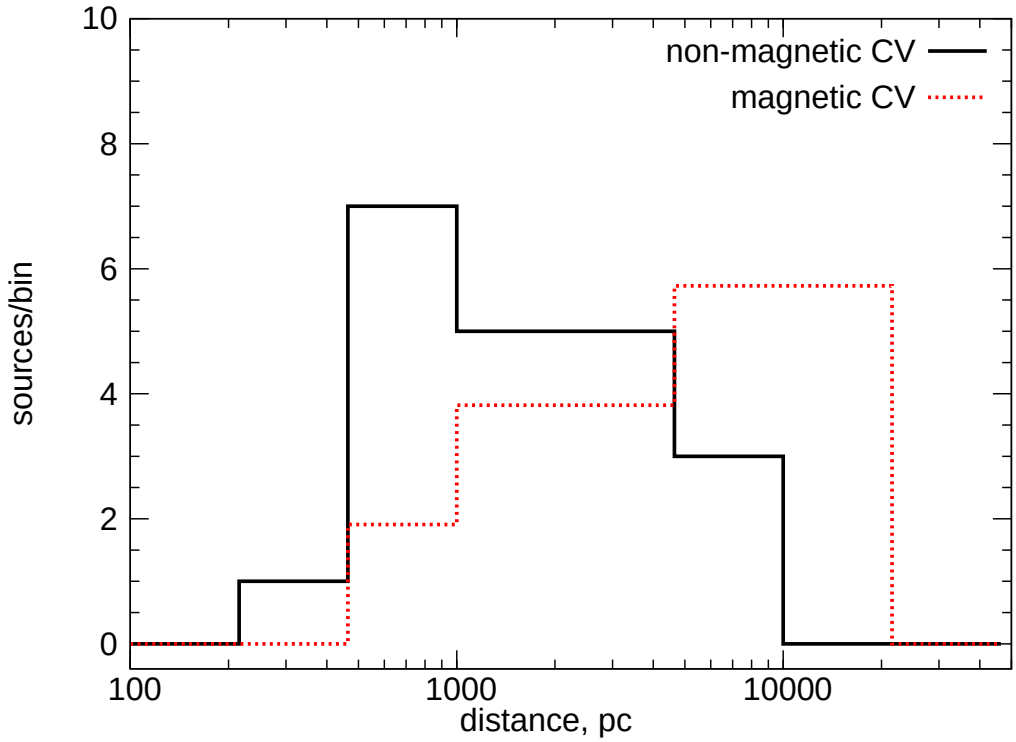

Figure 4.10: The distance distribution for CNe arising from magnetic and non-magnetic CVs. The total number of magnetic systems is normalized by 1.9 to match the number of non-magnetic ones. The data, used to produce this plot, is given in Table 4.4.

smaller for a more massive white dwarf. Taken at the face value, this would suggest the distance difference of ~ 1.6 which is smaller than the observed difference in average distance by a factor of ~ 3. Given the crudeness of this calculation, we conclude that these two numbers are broadly consistent with each other.

4.5.4 Dwarf novae

Dwarf novae (DNe) are a subclass of CVs showing frequent quasi-periodic outbursts due to thermal-viscous instability of the accretion disk (Osaki, 1974; Hoshi, 1979). In quiescence they become sources of relatively hard X-ray emission from the optically-thin boundary layer, whereas in outburst state the optically-thick accretion disk emits predominantly in the ultraviolet and soft X-ray bands. One of the models used to describe the emission spectra in the quiescence states is a cooling flow model (Meyer & Meyer-Hofmeister, 1994). Spectral analysis of a large number of quiescence spectra showed a relatively large dispersion in the value of the initial temperature $kT_{max} \sim 8 - 55$ keV with the average value of 23 keV (Pandel et al., 2005). This value is assumed in the calculations performed in this section.

Dwarf Novae give rise to CNe, contributing about $\sim 1/2$ to their observed number Ritter & Kolb (2003). In the quiescence state they may contribute to the unresolved emission. In the outburst state, to the opposite, soft emission is largely hidden because of the interstellar absorption. Therefore the bimodal behavior of dwarf novae can be used to constrain the fraction of mass which is accreted in quiescence. similar to how the upper limit on the contribution of magnetic systems was obtained. Using same approach

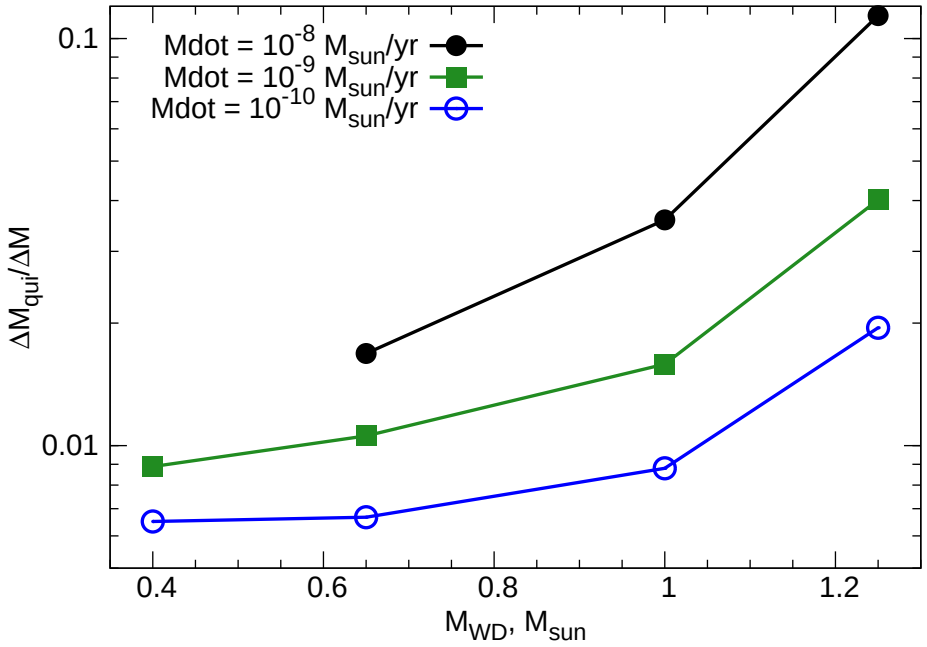

Figure 4.11: The fraction of mass accreted in quiescence as a function of white dwarf mass. Different mass accretion rates were assumed, the filled circles (black) correspond to 10^{-8} $M_\odot$/yr, the filled boxes (green) represent 10^{-9} $M_\odot$/yr, whereas the empty circles (blue) stand for 10^{-10} $M_\odot$/yr.

we calculate the X-ray luminosity in the quiescence state assuming that dwarf novae are responsible for a $\sim 1/2$ of CN events (the other half is due to nova-like variables, Ritter & Kolb (2003)). With this value one can put an upper limit on the fraction of mass, accreted during quiescence. The result of this calculation is shown in Figure 4.11. As in the case of magnetic systems, the absolute upper limit is $\sim$ 10 per cent. However, the white dwarf mass in dwarf novae typically does not exceed ≈ 0.9 $M_\odot$ and the mass accretion rate is not much larger that $\approx 10^{-8}$ $M_\odot$/yr, therefore the realistic upper limit is $\approx$ 3 per cent. As before, this result is not strongly sensitive to the choice of kT_{max} parameter of the cooling flow model. Assuming $kT_{max} = 55$ keV our upper limits would increase by $\approx 1/7$.

Using this upper limit, the enhancement factor of the accretion rate in outburst state can be inferred. Obviously, this quantity depends on the fraction of time spent in the outburst. Since for majority of DNe it is smaller than $\sim 1/5$ (Wils et al., 2009), the accretion rate increase by $\sim 30 - 1000$ during outburst. This conclusion is consistent with observations of dwarf novae. Indeed, one of the best studied dwarf nova, SS Cyg, spends $\sim$ 75 per cent of the time in quiescence (Cannizzo & Mattei, 1992). The accretion rate varies from $5 \cdot 10^{-11}$ $M_\odot$/yr in quiescence (Urban & Sion, 2006) to $3.2 \cdot 10^{-9}$ $M_\odot$/yr in outburst (Hamilton et al., 2007), hence the enhancement factor is 64 and $\approx$ 95 per cent of the material is accreted in outburst periods, in good agreement with our results.

4.5.5 Generalization of the results

Although we considered only the bulge of M31, our results can be generalized to other early-type galaxies.

The X-ray to K-band luminosity ratio in early-type galaxies, galaxy bulges, and in the Milky is in good agreement in the 2 – 10 keV band (Revnivtsev et al., 2006; Sazonov et al., 2006; Revnivtsev et al., 2007, present work).

The luminosity specific nova rate (ν_K) for a sample of galaxies is given in Williams & Shafter (2004). The obtained a fairly uniform values for early-type galaxies, in the range of $(1.80-2.72)\cdot10^{-10}$ $L_{\odot,K}$ yr^{-1}. Using the CN frequency and K-band luminosity, we obtain $\nu_K = (6.0 \pm 1.0)\cdot10^{-10}$ $L_{\odot,K}$ yr^{-1} for the bulge of M31. However, Williams & Shafter (2004) computed the K-band luminosity from (B–K) colour and B-band luminosity of the galaxy, which in case of M31 results in by a factor of $\sim$ 3 larger K-band luminosity, than the 2MASS value, and still by factor of $\sim$ 2 larger value than deduced from the Spitzer data (Williams & Shafter, 2004). With this correction $\nu_K = (3.0 \pm 0.5)\cdot10^{-10}$ $L_{\odot,K}$ yr^{-1} for the bulge of M31, which is in good agreement with other galaxies.

As both X/K ratio and ν_K are similar, our conclusions hold other early type galaxies.

4.6 Conclusion

We studied unresolved X-ray emission from the bulge and disk of M31 using publicly available *XMM-Newton* and *Chandra* data. The *XMM-Newton* survey of M31 covered the entire galaxy with the total exposure time of $\approx$ 639 ks after filtering. *Chandra* data covered the bulge and the southern part of the disk, with the exposure time of the filtered data of $\approx$ 222 ks.

We demonstrated that unresolved X-ray emission, associated with the bulge of the galaxy, extends into the disk with similar X-ray to K-band luminosity ratio. We obtained $L_X/L_K = (3.4-4.5)\cdot10^{27}$ erg s^{-1} $L_\odot^{-1}$ in the 2 – 10 keV band for all studied regions in the bulge and the disk of M31, which is in good agreement with those obtained for the Milky Way and for M32. This suggests that the unresolved X-ray emission in M31 may have similar origin to the Galactic ridge X-ray emission, namely it is a superposition of a large number of faint compact sources, such as accreting white dwarfs and coronally active binaries.

We investigated X-ray emission associated with the 10-kpc star-forming ring based on *XMM-Newton* data. We characterized this emission with L_X/SFR ratio, where L_X is calculated for the 0.5 – 2 keV energy range. We found that its value is spatially variable. After excluding the two regions along the minor axis of the galaxy, which are likely contaminated by the hot gas outflow, we obtained values ranging from zero to $L_X/SFR = 1.8\cdot10^{38}$ (erg s^{-1})/($M_\odot$/yr). The origin of these variations remains unclear.

We derived constraints on the nature of Classical Nova progenitors based on the brightness of unresolved emission. We demonstrated that magnetic CVs – polars and intermediate polars, do not contribute more than $\sim$ 3 per cent to the observed CN frequency, assuming values of parameters most likely for the CN progenitors, the absolute upper limit being $\approx$ 10 per cent. We also showed that in dwarf novae $\gtrsim$ 90 – 95 per cent of the material is accreted during outbursts, and only a small fraction during quiescent periods.

Acknowledgements. We thank the anonymous referee for useful comments. The authors are grateful to Hans Ritter for helpful discussions about cataclysmic variables. This research has made use of *Chandra* archival data provided by the *Chandra* X-ray Center. The publication makes use of software provided by the *Chandra* X-ray Center (CXC)

in the application package CIAO. *XMM-Newton* is an ESA science mission with instruments and contributions directly funded by ESA Member States and the USA (NASA). The *Spitzer Space Telescope* is operated by the Jet Propulsion Laboratory, California Institute of Technology, under contract with the National Aeronautics and Space Administration.

Bibliography

Araujo-Betancor, S., Gänsicke, B. T., Long, K. S., Beuermann, K., de Martino, D., Sion, E. M. & Szkody, P., 2005, ApJ, 622, 589

Arp, H. C., 1956, AJ, 61, 15

Bogdán, Á., Gilfanov, M., 2008, MNRAS, 388, 56

Brunschweiger, J., Greiner, J., Ajello, M. & Osborne, J., 2009, A&A, 496, 121

Cannizzo, J. K. & Mattei, J. A., 1992, ApJ, 401, 642

Csák, B., Kiss, L. L., Retter, A., Jacob, A. & Kaspi, S., 2005, A&A, 429, 599

Dickey, J. M., Lockman, F. J., 1990, ARA&A, 28, 215

Evans, P. A. & Hellier, C., 2007, MNRAS, 663, 1277

Fujimoto, M. Y., 1982, ApJ, 257, 752

Gilfanov, M. 2004, MNRAS, 349, 146

Gordon, K. D., Bailin, J., Engelbracht, C. W., et al. 2006, ApJ, 638, L87

Hamilton, R. T., Urban, J, A., Sion, E. M., Riedel, A. R., Voyer, E. N., Marcy, J. T. & Lakatos, S. L., 2007, ApJ, 667, 1139

Hickox, R. C., Markevitch, M., 2006, ApJ, 645, 95

Hoshi, R., 1979, PThPh, 61, 1307

Irwin, J. A., Athney, A. E. & Bregman, J. N. 2003, ApJ, 587, 356

Jarrett, T. H., Chester, T., Cutri, R., et al. 2003, AJ, 125, 525

Kamath, U. S., Anupama, G. C., Ashok, N. M. & Chandrasekhar, T., 1997, AJ, 114, 2671

Kennicutt, R. C. Jr., 1998, ARA&A, 36, 189

King, A. R. & Lasota, J. P., 1979, MNRAS, 188, 653

Kiss, L. L., Gogh, N., Vinkó, J., Fűrész, G., Csák, B., DeBond, H., Thomson, J. R. & Derekas, A., 2002, A&A, 384, 982K

Koyama, K., Hamaguchi, K., Ueno, S., et al. 1996, PASJ, 48, 87

Lamb, D. Q. & Masters, A. R., 1979, ApJ, 234, 117

Landi, R., Bassani, L., Dean, A. J., Bird, A. J., Fiocchi, M., Bazzano, A., Nousek, J. A. & Osborne, J. P., 2009, MNRAS, 392, 630

Lipkin, Y., Leibowitz, E. M., Retter, A. & Shemmer, O., 2001, MNRAS, 328, 1169

Macri, L. M. 2001, ApJ, 549, 721

Meyer, F. & Meyer-Hofmeister, E., 1994, A&A, 288, 175

Moretti, A., Campana, S., Lazzati, D., Tagliaferri, G. 2003, ApJ, 588, 696

Naik, S., Banerjee, D. P. K. & Ashok, N. M., 2009, MNRAS, 394, 1551

Nevalainen, J., Markevitch M. and Lumb, D. 2005, ApJ, 629, 172

Nieten, Ch., Neininger, N., Guelin, M., et al. 2006, A&A, 453, 459

Osaki, Y., 1974, PASJ, 26, 429

Paczyński, B. & Zytkow, A. N., 1978, ApJ, 222, 604

Pandel, D., Cordova, F. A., Mason, K. O., Priedhorsky, W. C., 2005, ApJ, 626, 396

Panei, J. A., Althaus, L. G. & Benvenuto, O. G. 2000, A&A, 353, 970

Poggiani, R., 2009, AN, 330, 77

Puebla, R. E., Diaz, M. P. & Hubeny, I., 2007, AJ, 134, 1923

Ramsay, G. & Cropper, M., 2004, MNRAS, 347, 497

Revnivtsev, M., Sazonov, S., Gilfanov, M., Churazov, E., Sunyaev, R., 2006, A&A, 452, 169

Revnivtsev, M., Churazov, E., Sazonov, S., Forman, W., Jones, C., 2007, A&A, 473, 783

Ritter, H. & Kolb, U., 2003, A&A, 404, 301

Sazonov, S., Revnivtsev, M., Gilfanov, M., Churazov, E., Sunyaev, R., 2006, A&A, 450, 117

Shafter, A. W., 1997, ApJ, 487, 226

Shafter, A. W., Irby, B. K., 2001, ApJ, 563, 767

Shtykovskiy, P. & Gilfanov, M., 2005, MNRAS, 362, 879

Stanek, K. Z., Garnavich, P. M., 1998, ApJ, 503, 131

Starrfield, S., Truran, J. W., Sparks, W. M., Kutter, G. S., 1972, ApJ, 176, 169

Stockman, H. S., Schmidt, G. D. & Lamb, D. Q., 1988, ApJ, 332, 282

Strüder, L., Briel, U., Dennerl, K., et al. 2001, A&A, 365, L18

Suleimanov, V., Revnivtsev, M., Ritter, H., 2005, A&A, 435, 191

Trudolyubov, S., Kotov, O., Priedhorsky, W., Cordova, F. & Mason, K., 2005, ApJ, 634, 314

Turner, M. J. L., Abbey, A., Arnaud, M., et al. 2001, A&A, 365, L27

Urban, J. A. & Sion, E. M., 2006, ApJ, 642, 1029

Vaytet, N. M. H., O'Brien, T. J. & Rushton, A. P., 2007, MNRAS, 380, 175

Voss, R. & Gilfanov, M. 2007, A&A, 468, 49

Warner, B. & Woudt, P. A., 2009, MNRAS, 397, 979

Williams, S. J. & Shafter, A. W., 2004, ApJ, 612

Wils, P., Gänsicke, B. T., Drake, A. J. & Southworth, J., 2009, arXiv:0910.3218

Yaron, O., Prialnik, D., Shara, M. M., Kovetz, A., 2005, ApJ, 623, 398

Chapter 5

Unresolved emission and ionized gas in the bulge of M31

Monthly Notices of the Royal Astronomical Society, 388, 56, 2008

Bogdán, Á. & Gilfanov, M.

5.1 Abstract

We study the origin of unresolved X-ray emission from the bulge of M31 based on archival *Chandra* and *XMM-Newton* observations. We demonstrate that three different components are present: (i) Broad-band emission from a large number of faint sources – mainly accreting white dwarfs and active binaries, associated with the old stellar population, similar to the Galactic Ridge X-ray emission of the Milky Way. The X-ray to K-band luminosity ratios are compatible with those for the Milky Way and for M32, in the $2-10$ keV band it is $(3.6 \pm 0.2) \cdot 10^{27}$ erg s^{-1} $L_{\odot}^{-1}$. (ii) Soft emission from ionized gas with temperature of about $\sim$ 300 eV and mass of $\sim 2 \cdot 10^6$ $M_{\odot}$. The gas distribution is significantly extended along the minor axis of the galaxy suggesting that it may be outflowing in the direction perpendicular to the galactic disk. The mass and energy supply from evolved stars and type Ia supernovae is sufficient to sustain the outflow. We also detect a shadow cast on the gas emission by spiral arms and the 10-kpc star-forming ring, confirming significant extent of the gas in the "vertical" direction. (iii) Hard extended emission from spiral arms, most likely associated with young stellar objects and young stars located in the star-forming regions. The L_X/SFR ratio equals $\sim 9 \cdot 10^{38}$ (erg/s)/($M_{\odot}$/yr) which is about $\sim 1/3$ of the HMXBs contribution, determined earlier from *Chandra* observations of other nearby galaxies.

5.2 Introduction

The X-ray radiation from the majority of galaxies is dominated by X-ray binaries (e.g. Fabbiano, 2006). In addition, extended emission is present in galaxies of all morphological types. At least part of this emission is associated with stellar population and is a superposition of a large number of faint compact sources – accreting white dwarfs, active binaries and other types of stellar sources, old and young (Revnivtsev et al. 2006; Sazonov et al., 2006). There is also a truly diffuse component – emission from ionized gas of sub-keV temperature. Its importance varies from galaxy to galaxy, with luminous gas-rich ellipticals, like NGC 1316 (Kim & Fabbiano, 2003) and dwarf galaxies similar to M32 (Revnivtsev et al., 2007) representing the two opposite ends of the range. Significant diffuse or quasi-diffuse emission is also associated with star-formation, the Antennae (e.g. Baldi et al., 2006) being one of the nearby examples. The morphology of the gas in starburst galaxies often indicates outflows, driven by the energy input into ISM from core collapse supernovae. Theoretical considerations suggest that gas in low mass elliptical galaxies may also be in the state of outflow (David et al., 2006). The mass and energy budget of the ISM in this case is maintained by winds from evolved stars and Type Ia supernovae. The overall X-ray radiation from a galaxy is a superposition of these (and possibly other) components, their relative importance being defined by the morphological type of the galaxy and its star-formation and merger history.

Our close-by neighbor, M31 galaxy gives a unique opportunity to explore a "full-size" spiral galaxy similar to the Milky Way without complications brought about by projection and absorption effects, often hampering studies of our own Galaxy. Not surprisingly, it has been extensively investigated by every major observatory of the past decades. Observations by the *Einstein* observatory demonstrated that X-ray binaries account for the most of the X-ray emission from the galaxy (van Speybroeck et al. 1979; Fabbiano et al., 1987). Using the complete set of *Einstein* data Trinchieri & Fabbiano (1991) constrained possible amount of ionized gas in the bulge of the galaxy by $\lesssim 2 \cdot 10^6 M_\odot$. Based on the *ROSAT* observations, Primini et al. (1993) found evidence for extended emission component with luminosity of $\sim 6 \cdot 10^{38}$ erg/s in the 0.2–4 keV band. They suggested, that this emission may be of truly diffuse origin or due to a new class of X-ray sources. The unresolved emission from M31 was investigated further by Supper et al. (1997), West et al. (1997), Irwin & Bregman (1999), Borozdin & Priedhorsky (2000). In all these studies the existence of a soft emission component with temperature $kT \sim 0.3 - 0.4$ keV has been confirmed, although different authors suggested different explanations of its origin. With advent of *Chandra* and *XMM-Newton*, the consensus seemed to be achieved in favor of truly diffuse origin of the soft emission component (Shirey et al. 2001; Takahashi et al., 2004). However, recent progress in understanding the nature of the Galactic Ridge emission as a superposition of a large number of faint stellar type sources (Revnivtsev et al., 2006), made it worth to revisit the problem of the origin of extended emission in M31. Also, with more *Chandra* and *XMM-Newton* observations, more accurate and detailed investigations became possible. Recently (Li & Wang, 2007) analyzed large *Chandra* dataset of M31 bulge observations and demonstrated presence of both ionized gas and emission of faint compact sources associated with old stellar population. Moreover, they revealed peculiar morphology of the gas emission and suggested that the X-ray gas in the bulge of M31 may be in the state of outflow.

In the present paper we combine extensive set of *Chandra* and *XMM-Newton* observations to obtain a

broad band and large field view of the X-ray emission originating in and around the bulge of M31. We restrict our study to the central region of ~ 20 arcmin in radius, covered well by *Chandra* and *XMM-Newton* observations currently available in the public archives of these observatories (Figure 5.1). The investigated region has the linear size of ~ 4 kpc along the major axis of the galaxy, but extends out to ~ 16 kpc along the plane of the galaxy in the minor axis direction, due to rather large inclination angle of M31, $i \sim 77°$ (Henderson, 1979). We assume the distance to Andromeda of 780 kpc (Stanek & Garnavich 1998; Macri, 1983). The Galactic absorption towards M31 is $6.7 \cdot 10^{20}$ cm^{-2} (Dickey & Lockman, 1990).

The paper is structured as follows. In Section 5.3 we describe the data and its reduction. We introduce our results in Section 5.4, where we present the spatial distribution, morphology and the spectra of the extended emission. In Section 5.5 the origin, properties and physical parameters of different components are discussed and in Section 5.6 we summarize our results.

5.3 Data reduction

We combine data from *Chandra* and *XMM-Newton* satellites adding their benefits together. The primal advantage of *Chandra* is its good angular resolution which allows us to resolve individual X-ray binaries everywhere including the very central region of the bulge. *XMM-Newton* provided better coverage of M31 and collected more photons, thanks to its larger effective area. It is more suitable to study the outer part of M31. On the other hand the higher and less predictable background of *XMM-Newton* complicates study of low surface brightness regions.

5.3.1 *Chandra*

We used 21 archival *Chandra* observations listed in Table 5.1, taken between 13.10.1999 and 23.05.2004. For the analysis we extracted data of the ACIS-I array except for OBS-ID 1575 where we used only the S3 chip. The pattern of available *Chandra* observations allows us to study the central ≈ 15 arcmin region. The data reduction was performed using standard CIAO [1] software package tools (CIAO version 3.4; CALDB version 3.4.1). For each observations we filtered out the flare contaminated intervals, excluding the time intervals where the count rate deviated by more than 20 per cent from the mean value. The resulting effective exposure times are given in Table 5.1.

Crucial for the analysis of the low surface brightness outer regions is the accuracy of the background subtraction. In treating the *Chandra* background we generally followed the procedures outlined in Hickox & Markevitch (2006). We determined the level of the instrumental background using the stowed data set[2]. In the stowed position of ACIS detectors the sky emission is blocked and only the instrumental background gives a contribution. As demonstrated in the above-mentioned paper, although the instrumental background level varies with time, its spectrum remains unchanged. The effective area of *Chandra* is negligible above 9 keV and the count rate is dominated by the instrumental background. Therefore the $9.5-12$ keV count rates can be used to renormalize background spectra obtained from the stowed datasets. In dealing with cosmic background we took into account that it consists of the soft emission associated

[1] http://cxc.harvard.edu/ciao/

[2] http://cxc.harvard.edu/contrib/maxim/stowed/

Table 5.1: The list of *Chandra* observations used for the analysis.

Obs ID	$T_{\rm original}$	$T_{\rm eff}$	Instrument	Date
303	12.0 ks	8.2 ks	ACIS-I	1999 Oct 13
305	4.2 ks	4.0 ks	ACIS-I	1999 Dec 11
306	4.2 ks	4.1 ks	ACIS-I	1999 Dec 27
307	4.2 ks	3.1 ks	ACIS-I	2000 Jan 29
308	4.1 ks	3.7 ks	ACIS-I	2000 Feb 16
311	5.0 ks	3.9 ks	ACIS-I	2000 Jul 29
312	4.7 ks	3.8 ks	ACIS-I	2000 Aug 27
1575	38.2 ks	38.2 ks	ACIS-S	2001 Oct 05
1577	5.0 ks	4.9 ks	ACIS-I	2001 Aug 31
1583	5.0 ks	4.1 ks	ACIS-I	2001 Jun 10
1585	5.0 ks	4.1 ks	ACIS-I	2001 Nov 19
2895	4.9 ks	3.2 ks	ACIS-I	2001 Dec 07
2896	5.0 ks	3.7 ks	ACIS-I	2002 Feb 06
2897	5.0 ks	4.1 ks	ACIS-I	2002 Jan 08
2898	5.0 ks	3.2 ks	ACIS-I	2002 Jun 02
4360	5.0 ks	3.4 ks	ACIS-I	2002 Aug 11
4678	4.9 ks	2.7 ks	ACIS-I	2003 Nov 09
4679	4.8 ks	2.7 ks	ACIS-I	2003 Nov 26
4680	5.2 ks	3.2 ks	ACIS-I	2003 Dec 27
4681	5.1 ks	3.3 ks	ACIS-I	2004 Jan 31
4682	4.9 ks	1.2 ks	ACIS-I	2004 May 23

with the Galaxy and harder extragalactic component and treated them separately. For the soft Galactic component we used the best fit spectrum from Hickox & Markevitch (2006). For the extragalactic background we took into account that some fraction of it has been resolved in our data analysis procedure and removed along with X-ray binaries. Using the incompleteness function from Voss & Gilfanov (2007), that was obtained using essentially the same data set, we estimated that our point source detection sensitivity in the outer regions is $\approx 5 \cdot 10^{35}$ erg/s. We used the sensitivity for outermost regions because the CXB subtraction plays role only in these regions where the surface brightness of the source emission is low. This point source sensitivity results in the resolved CXB fraction of ≈ 50 per cent, according to Moretti et al. (2003). The Galactic and cosmic backgrounds were subtracted from the vignetting corrected images and profiles.

In order to study the diffuse emission we need to exclude contribution of bright LMXBs. According to the luminosity functions of LMXBs and faint compact sources associated with old population (Gilfanov 2004; Sazonov et al., 2006), the contribution of the former is defined by the sources more luminous than $\log L_X \sim 35.5 - 36.0$. Below this threshold active binaries and cataclysmic variables are

Table 5.2: The list of *XMM-Newton* observations used for the analysis.

Obs ID	$T_{\rm original}$	$T_{\rm eff}$	Date
0109270101	62.5 ks	16.0 ks	2001 Jun 29
0112570101	61.1 ks	52.6 ks	2002 Jan 6
0112570401	31.0 ks	25.0 ks	2000 Jun 25
0202230201	18.3 ks	17.8 ks	2004 Jul 16
0202230401	14.6 ks	9.0 ks	2004 Jul 18
0202230501	21.8 ks	2.0 ks	2004 Jul 19

the dominating X-ray sources. The individual *Chandra* observations are too short (typically, $\sim$ 4 ks, see Table 5.1) to achieve this sensitivity, therefore we ran point source detection on the combined image with total exposure of $T_{\rm eff}$ = 112.6 ks. To combine the data, each observation was projected into the coordinate system of OBS-ID 303 and the attitude corrections from Voss & Gilfanov (2007) were applied in order to better co-align individual event lists. To detect point sources we ran CIAO `wavdetect` tool in the $0.5-8$ keV band. Some parameters were changed from the default values to fit our aims. The scales on which we were looking for sources were the $\sqrt{2}$-series from 1.0 to 8.0. To minimize the contribution of residual counts from point sources to diffuse emission we increased the value of the sigma parameter to 4; this parameters describes the size of elliptical source detection regions in standard deviations assuming a 2D Gaussian distribution of source counts. With these adjustment we obtained larger source regions than usual, including larger fraction of source counts. To increase sensitivity we did not filter out flare containing time intervals for point source detection. The resulting source list consisted totally of 238 sources in the investigated area; the detected sources are in good agreement with results of Voss & Gilfanov (2007). The sensitivity limit in the central region was 10^{35} erg/s, while in the outermost region it deteriorated to $5 \cdot 10^{35}$ erg/s. Extracting the point spread function with `mkpsf` for each source we calculated the fraction of counts inside the source cell. For most of the sources this fraction exceeded 98 per cent, if it was smaller then the source cells were enlarged accordingly. The output source cells were used to mask out the point sources for further image and spectral analysis.

We produced exposure maps using a two component spectral model consisting of an optically-thin thermal plasma emission with temperature of 0.30 keV and a powerlaw component with a slope of Γ = 1.80. The ratio of the normalizations of these two components was 3/1. This is the best fit two component model to the spectrum of the central 200 arcsec region.

5.3.2 *XMM-Newton*

We analyzed 6 archival *XMM-Newton* observations taken between 25.06.2000 and 19.07.2004, as listed in Table 5.2. We used the data of the European Photon Imaging Camera (EPIC) instruments (Strüder et al. 2001; Turner et al., 2001). For data reduction we used Science Analysis System (SAS) version 7.1.

In order to exclude the flare contaminated time intervals we double filtered the lightcurves using hard-

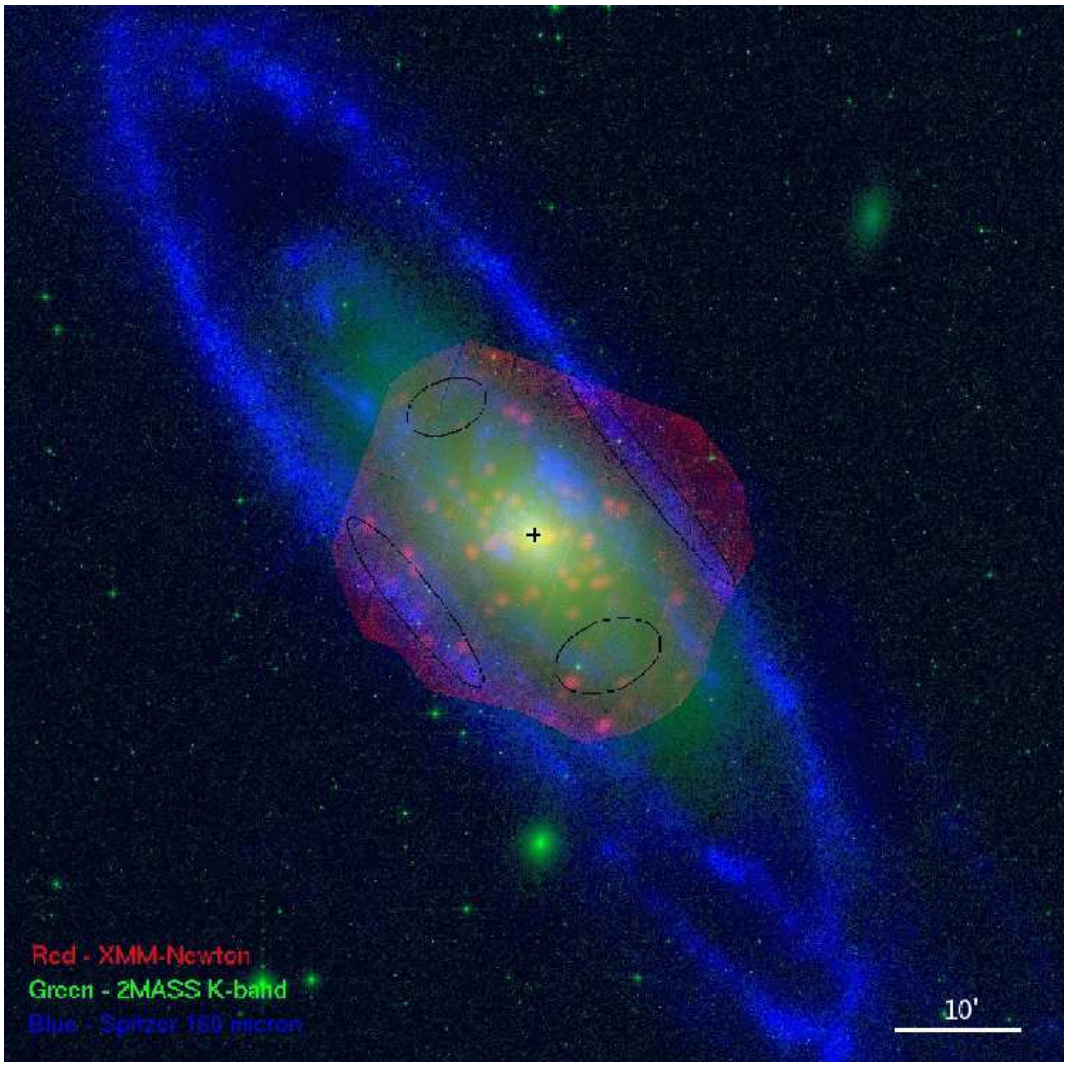

Figure 5.1: RGB image of M31. The colors are as follows: red is the *XMM-Newton* data in the 0.5−1.2 keV band, green is an image of the K-band light from 2MASS and blue is the 160 μm image of Spitzer. Center of the M31 is marked with a cross. North is up and east is left.

band ($E > 10$ keV) and soft-band ($E = 1 - 5$ keV) energy ranges according to Nevalainen et al. (2005), using 20 per cent threshold for deviation from the mean count rate. The remaining useful exposure time is about 58 per cent of the original value. The data was cleaned from the out of time events using the Oot event lists.

The observations were re-projected into the coordinate system of OBS-ID 0112570101 and merged together. For point source removal we combined the source list obtained from *Chandra* and *XMM-Newton* observations. In regions which lied outside the field of view of *Chandra* we ran the SAS source detection task to complement the *Chandra* source list. The source regions were enlarged to account for larger size of the point spread function of *XMM-Newton* mirrors, their size was adjusted to approximately match $\sim 90 - 98$ per cent PSF encircled energy radius depending on the brightness of the point source. It was not possible to reliably exclude point source contribution in the crowded central ~ 100 arcsec region, therefore

it was not used in the following analysis. Exposure maps were calculated using the `eexpmap` command of SAS. In transforming the counts to flux units we assumed the same spectrum as for *Chandra*.

The particle background on EPIC CCDs consists of two components. The "internal" component is generated in interactions of cosmic rays with the detector material and is approximately uniform across the detector. The second component is due to low energy solar protons, concentrated by the mirror systems of the telescopes; it is vignetted by the mirrors response but the vignetting is flatter than that for photons. The level of both background components is variable (see http://www.star.le.ac.uk/~amr30/BG/BGTable.html for details). According to this we performed the background subtraction in two steps. At the first step the corners of the CCDs which lie outside of the field of view, were used to determine the level of the flat internal background. The obtained background level was subtracted from each observations individually. The combined contribution of the solar protons component and cosmic background was approximately determined from the observations of nearby fields without extended sources and subtracted from the final vignetting corrected image. This method is not perfect, due to the difference in the shape of the vignetting function between solar protons and photons and due to variability of the solar protons level. However, good agreement between emission spectra obtained from *Chandra* and *XMM-Newton* data confirms adequate accuracy of this procedure.

5.4 Results

5.4.1 Images

The RGB image in Figure 5.1 presents the *XMM-Newton* data (red) overlaid on the 160 μm Spitzer image (Rieke at al., 2004) (blue) and K-band image from 2MASS Large Galaxy Atlas (Jarrett et al., 2003) (green). Although the main purpose of this image is to show the X-ray data coverage, it crudely illustrates the presence of a large population of compact sources as well as of the extended emission. It also demonstrates the effect of the spiral arms on X-ray surface brightness distribution.

The brightness distribution of the extended emission, after removal of the point sources, is shown in Figure 5.2 along with the contours of the K-band brightness. The X-ray image was constructed from *Chandra* data in the $0.5-1.2$ keV band. The point sources were excluded and their locations were filled up with the average local background around the sources. The X-ray image is adaptively smoothed. In order to compare the X-ray surface brightness with the distribution of the stellar mass we also show K-band contours. The surface brightness of the extended emission approximately follows the K-band distribution but the image suggests that the agreement is not perfect and some distortions in the east-west direction may be present. In order to investigate this in details we consider profiles along the major and minor axes of the galaxy.

5.4.2 Surface brightness distribution along the major and minor axis

We studied brightness distribution in two energy bands, $0.5-1.2$ keV and $2-7$ keV. Our choice had been motivated by the shape of the spectrum of extended emission discussed in the next Section. The profiles were constructed along the major and minor axis with position angles of 45° and 135° respectively.

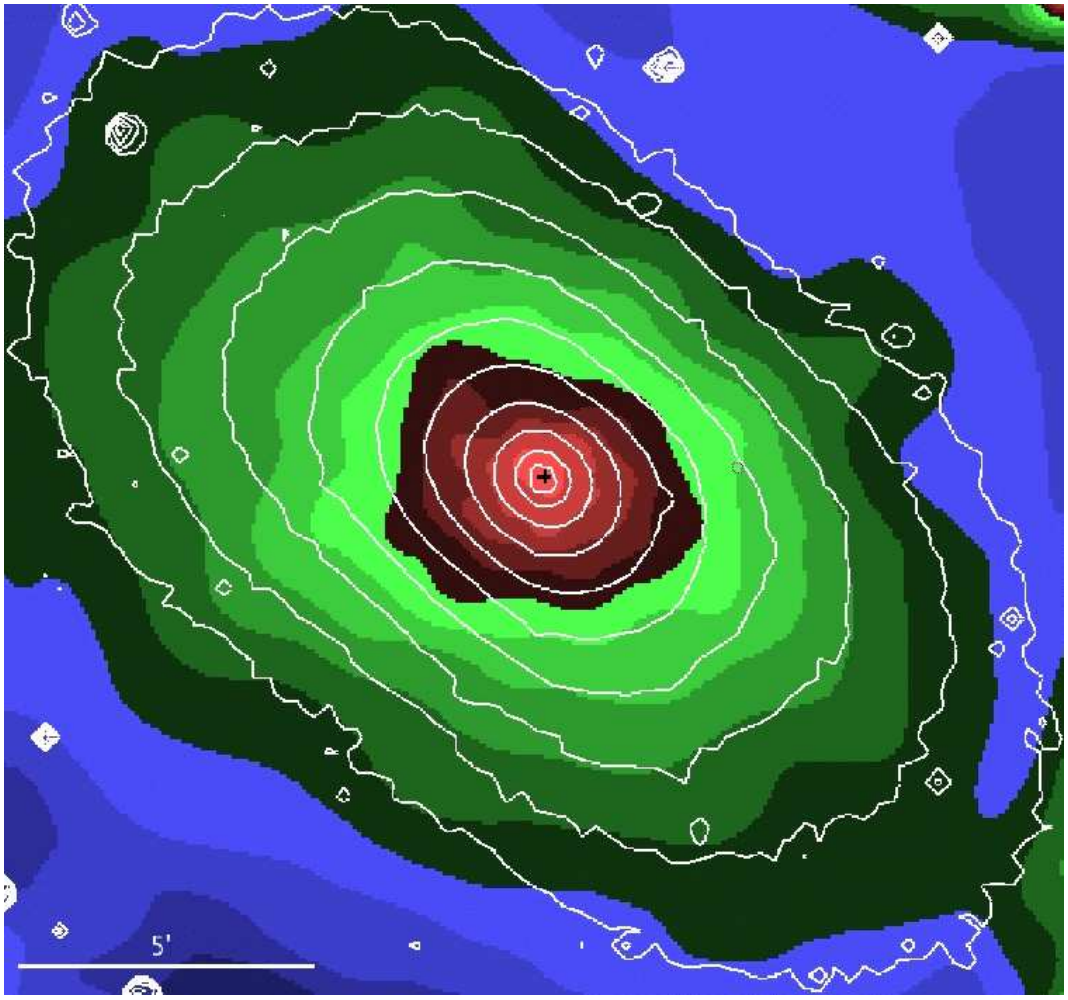

Figure 5.2: Adaptively smoothed *Chandra* image in the 0.5 – 1.2 keV band overplotted with K-band contours. The point sources were removed and their locations were filled with the local background value. Center of the M31 is marked with a cross. North is up and east is left.

For each profile surface brightness was averaged over 500 arcsec in the transverse direction, corrected for vignetting and the estimated background level was subtracted. For *XMM-Newton* the background level was adjusted to achieve better agreement with *Chandra* profiles. The adjusted values were well within the range of the background levels observed in individual blank-sky observations and differed from the average blank-sky level by $\lesssim$ 20 per cent. The values of background were $(4.3,\ 5.6,\ 5.2,\ 6.2) \cdot 10^{-19}$ erg s^{-1} arcsec^{-2} cm^{-2} for *Chandra* (soft, hard) and *XMM-Newton* (soft, hard) respectively. For all distributions we found good agreement between the *Chandra* and *XMM-Newton* data. We compare X-ray distribution with profiles of the K-band emission. As it is well-known, the latter is a good stellar mass tracer. The K-band profile was obtained for the same regions as the X-ray profiles, in particular the same source regions were excluded in computing all profiles. The normalizations for the K-band profile are $4 \cdot 10^{27}$ and $3 \cdot 10^{27}$ erg s^{-1} L$_{\odot}^{-1}$ for soft and hard band respectively.

On Figure 5.3 we show the distribution along the major axis. In the 0.5−1.2 keV band the profile shows an excess emission in the central part of the bulge. At bigger central distances the X-ray and K-band light

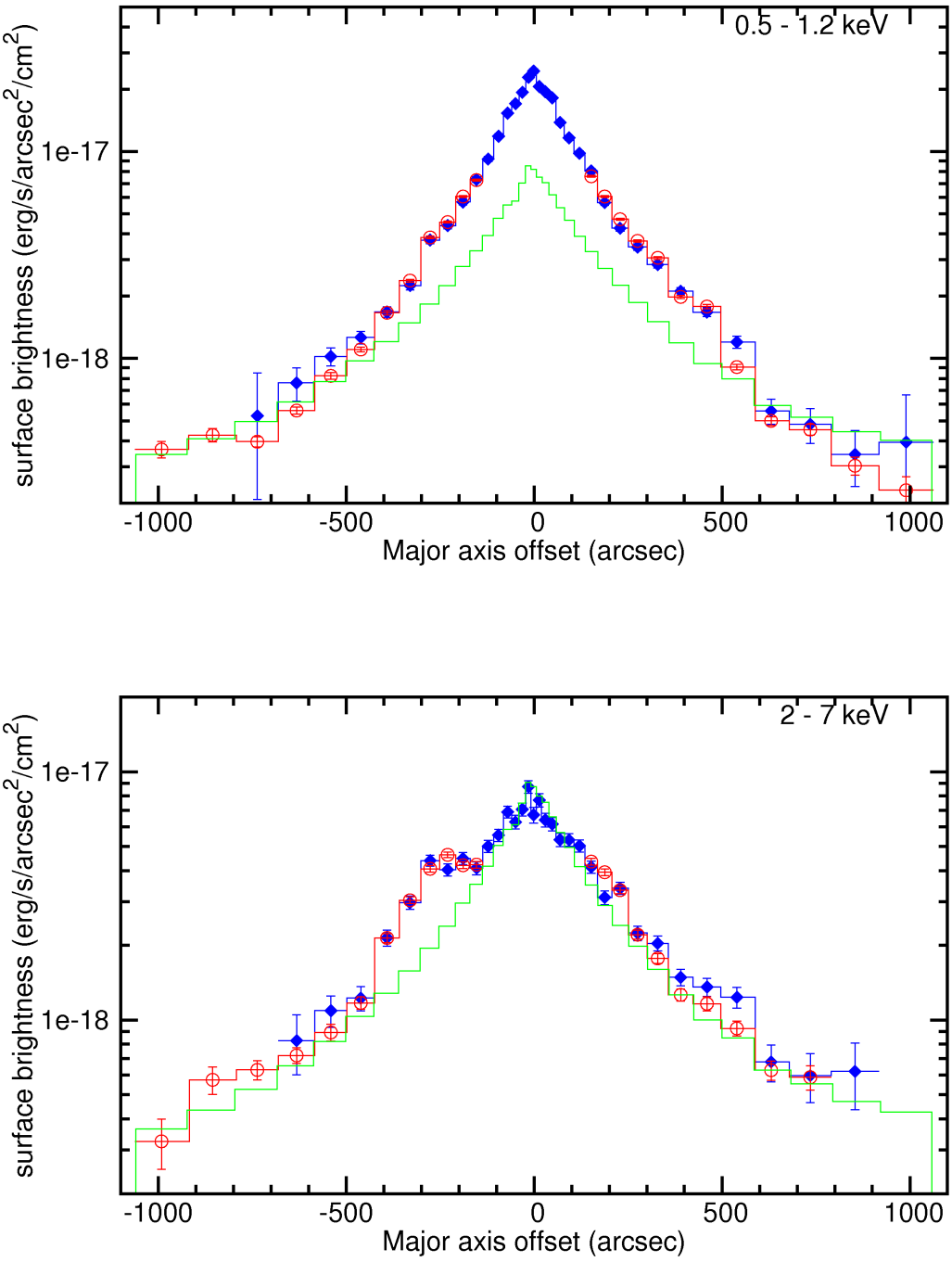

Figure 5.3: Surface brightness distribution along the major axis. in the 0.5 – 1.2 keV (upper panel) and 2 – 7 keV (lower panel) energy bands, background subtracted. The filled symbols (blue in the color version of the plot) show the *Chandra* data, open symbols (red) show the *XMM-Newton* data and the solid histogram (green) without symbols is the normalized K-band brightness. The normalization factors are $4 \cdot 10^{27}$ and $3 \cdot 10^{27}$ erg s^{-1} L$_{\odot}^{-1}$ for soft and hard band respectively. The x-coordinate increases from south-west to north-east.

follow each other. In the hard band the X-ray surface brightness follows the near-infrared light distribution rather well at all central distances, with exception of the shoulder at the offset of −300 arcsec. The excess luminosity of the shoulder above the level suggested by the K-band profile is $\sim 2 \cdot 10^{37}$ erg/s. Its origin is unclear. There is no any easily identifiable feature in the image with which it could be associated. It can not be due to residual contamination from point sources. Indeed, the excess count rate associated with the shoulder is ∼ 20 per cent of the total count rate of all point sources detected in this region. This is much larger than the expected residual contamination from point sources in *Chandra* images, $\lesssim 2-3$ per cent. Good agreement between *Chandra* and *XMM-Newton* data also excludes the possibility that it is caused by an irregularity in the instrumental background.

The soft band profile along the minor axis (Figure 5.4) at all offsets exceeds the level suggested by the K-band profile normalized according to the X/K ratio from the major axis distribution. Moreover, the X/K ratio increases significantly outside ∼ 500 arcsec from the center – the X-ray distribution appears to have "wings" extending out to ∼ 900 arcsec or more. Note that exact shape of the surface brightness distribution at large offsets from the center depends on the adopted blank-sky level. The latter can not be directly determined from the currently available data, due to its limited field of view. For this reason we used the average CXB level and corrected it for the fraction of resolved background sources, as described in Section 5.3.1. The obtained value, $\sim (4-5)\cdot 10^{-19}$ erg/s/cm^2, is comparable to the remaining (background subtracted) flux as can be seen in Figure 5.4. Therefore the extend of the X-ray emission at large off-center angles can not be unambiguously constrained from the present data. In order to eliminate this uncertainty, more extensive *Chandra* observations, including large offset angles are needed. We note however, that the existence of unresolved emission at large offsets is independently confirmed by the east-west asymmetry of the shadow cast by the 10-kpc star-forming ring, as discussed below.

There is a clear asymmetry between eastern and western halves of the profile, the latter being notably suppressed at offset values of +300 arcsec and +600 arcsec. The origin of this asymmetry becomes clear after comparison with the 160 μm Spitzer profile. The far-infrared profile, plotted in Figure 5.4 shows several prominent peaks, corresponding to the 10-kpc star-forming ring and inner spiral arms (Gordon et al., 2006). The surface brightness suppressions in the western side of the profile (positive offsets) correspond to the spiral arm and the 10-kpc ring. On the other hand no significant effect of the 10-kpc ring can be seen on the eastern side of the galaxy (negative offsets).

The spatial orientation of M31 plays an important role in understanding the link between the X-ray and far-infrared distributions. We see the galaxy with approximately 77° inclination (Henderson, 1979) and the western side of the galactic disk is closer to us (Simien et al., 1978). The effect of this is that we see the western side of the bulge through the spiral arms, so the neutral gas and dust in the star forming regions cast a shadow on the extended emission in the soft band. The eastern side of the disk, on the contrary, is located behind the bulge and does not obscure its emission. We estimated the column density of the obscuring material in the spiral arms using the observed brightness difference between the eastern and western sides and obtained $N_H \sim 1-3\cdot 10^{21}$ cm^{-2}. These numbers are compatible with values derived from CO maps (Nieten et al., 2006).

In the hard band profile along the minor axis we see correlation between the X-ray and far-infrared emission – the X-ray brightness appears to increase at the positions of spiral arms. This suggests that

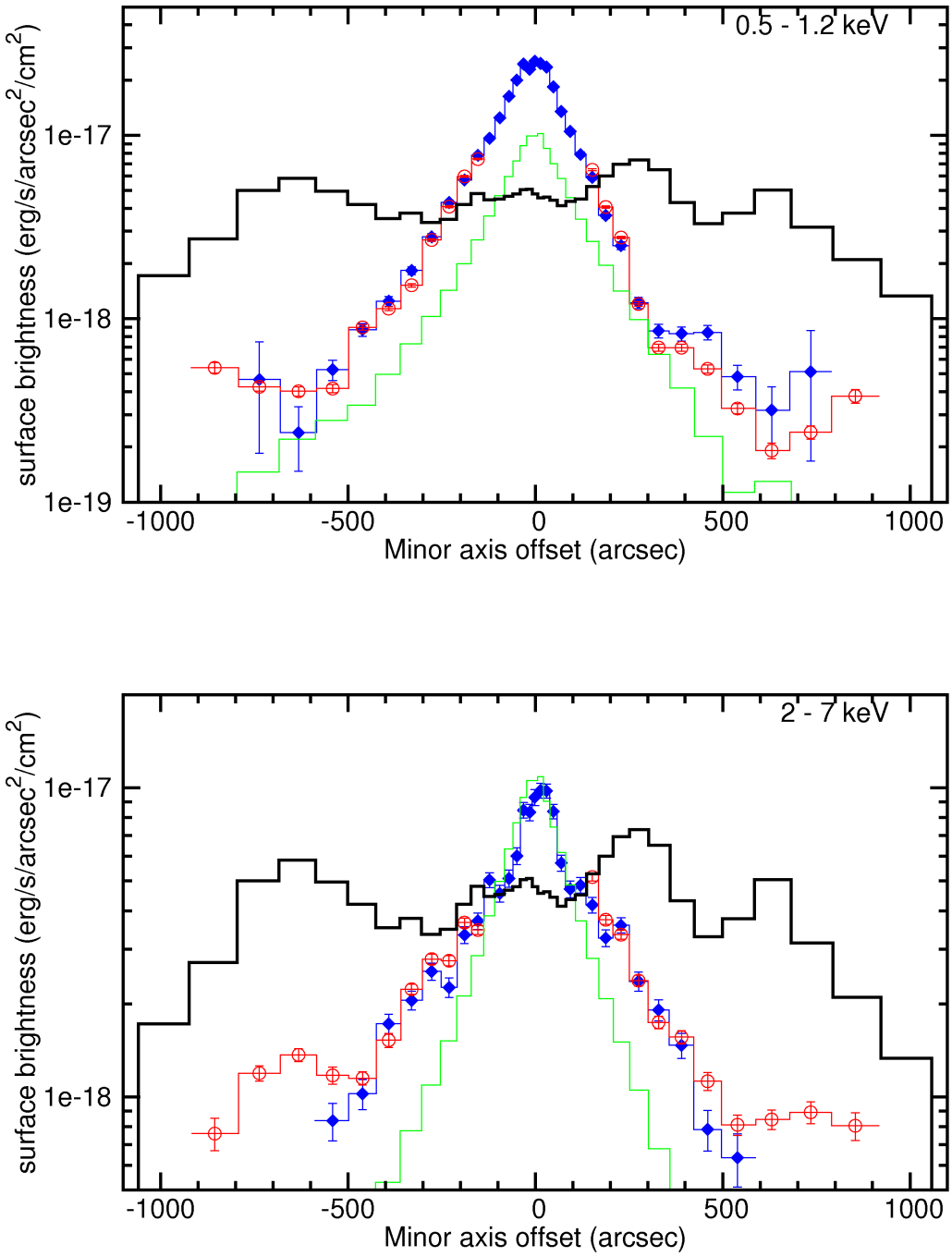

Figure 5.4: Same as Figure 5.3 but along the minor axis. The normalizations of the K-band profile are same as in Figure 5.3. The solid histogram with multiple peaks (black) shows the distribution of the 160 μm emission as obtained by Spitzer. The x-coordinate increases from south-east to north-west.

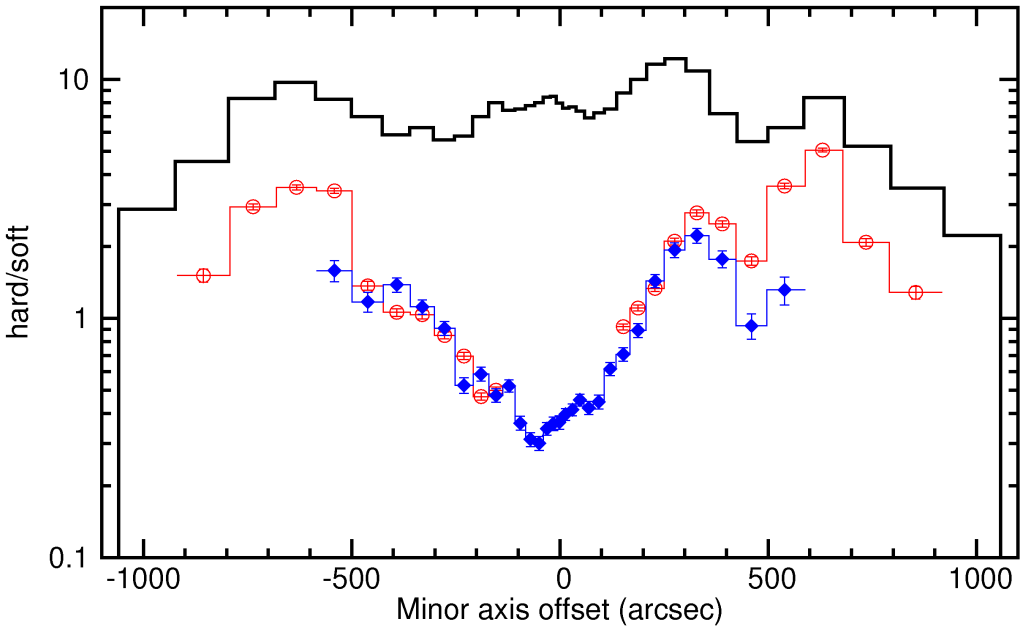

Figure 5.5: The X-ray hardness ratio profile along the minor axis, computed using the energy bands from Figure 5.4. The *Chandra* and *XMM-Newton* data are presented by the same symbols as in Figure 5.4. The solid histogram (black) shows the distribution of the 160 μm emission obtained by Spitzer. The x-coordinate increases from south-east to north-west.

spiral arms are sources of harder X-ray emission. To further illustrate the impact of spiral arms on the observed X-ray brightness we plot in Figure 5.5 the hardness ratio along the minor axis together with the 160 μm distribution. This plot confirms the presence and significance of the soft emission in the center. The hardness ratio has clear peaks at the positions of spiral arms, which are caused by two effects – obscuration by neutral and molecular gas and dust in the soft band and enhanced hard emission associated with the spiral arms.

Based on the X-ray brightness distributions we conclude that there are at least three different components in the unresolved X-ray emission from the central region of M31:

1. broad band component, following the distribution of K-band light (i.e. of stellar mass),
2. soft emission, localized in central $\sim$ 500 arcsec along the major axis of the galaxy and extending out to $\sim$ 900 arcsec or more along the minor axis,
3. harder emission from the spiral arms and 10-kpc star-forming ring.

5.4.3 Spectra

We used the ACIS "blank-sky" files in order to subtract the background from *Chandra* spectra. As before, we renormalized the background spectra using the 9.5 – 12 keV band count rates. For *XMM-*

Table 5.3: Results of the spectral fits in different regions of M31 using *Chandra* and *XMM-Newton* observations. PL denotes the power law and MKL is the optically-thin thermal plasma emission model.

	Inner region		Outer region		Spiral arms		M32	
Model	Γ/kT	χ^2/(d.o.f.)	Γ/kT	χ^2/(d.o.f.)	Γ/kT	χ^2/(d.o.f.)	Γ/kT	χ^2/(d.o.f.)
PL	—	—	—	—	2.00 ± 0.15	292/192	2.07 ± 0.15	113/72
PL	1.79 ± 0.10		$2.48^{+0.55}_{-0.44}$				1.65 ± 0.21	
MKL	0.36 ± 0.01	312/186	0.31 ± 0.08	127/101	—	—	0.54 ± 0.15	83/70

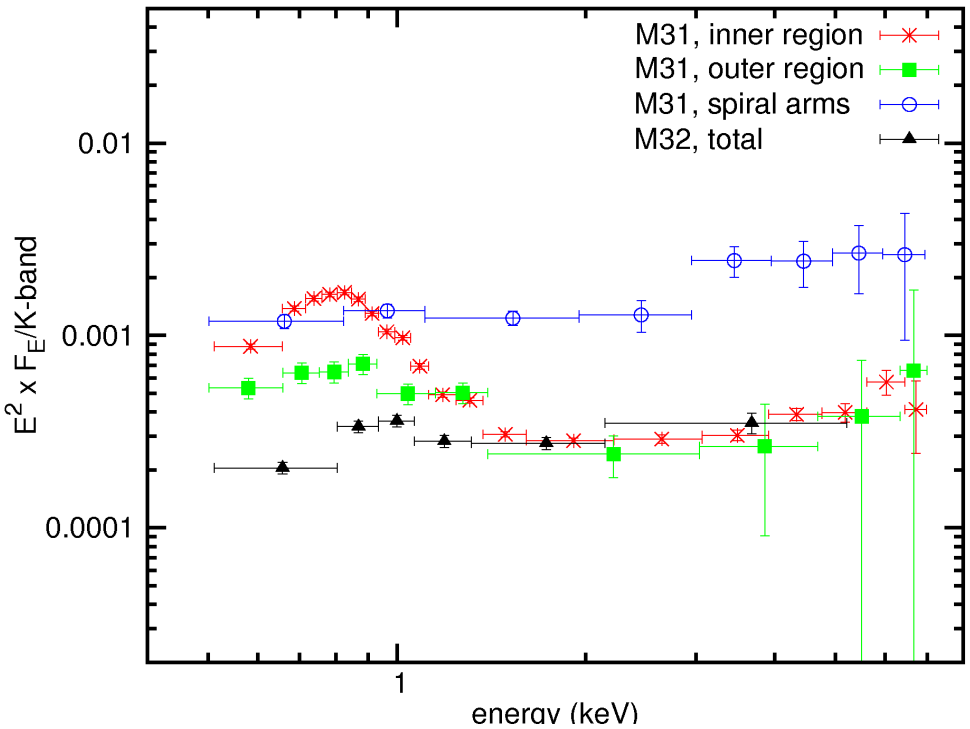

Figure 5.6: X-ray spectra of different regions in M31 and of M32: stars (red) – inner bulge – the spectrum of central 200 arcsec region; filled boxes (green) – outer bulge – combined spectrum of two elliptical regions at ∼ 700 arcsec from the center along the major axis; open circles (blue) – spiral arms – two elliptical regions at the 10-kpc ring; filled triangles (black) – spectrum of M32. The M31 regions are shown in Figure 5.1 The inner bulge and M32 spectra are obtained by *Chandra*, outer bulge and spiral arms – by *XMM-Newton*. All spectra are normalized to the K-band flux.

Newton we used a combined spectrum of observations of nearby fields as a background spectrum and renormalized it using the 10 – 12 keV count rate. We found good agreement between *Chandra* and *XMM-Newton* spectra in all investigated regions.

In Figure 5.6 we show spectra of different regions in M31. The spectral extraction regions are depicted in Figure 5.1. The spectra of outer bulge and spiral arms are based on *XMM-Newton* data, other spectra are from *Chandra*. Also shown is the spectrum of M32. It was obtained using *Chandra* observations OBSID 2017, 2494 and 5690 with exposure time of $T_{\rm eff}$ = 168.5 ks. The spectrum was extracted from elliptical region with the position angle of 40° and with 90 arcsec major and 71 arcsec minor axes; the data analysis procedures were identical to M31. All spectra are normalized to the same level of K-band brightness. The spectral fitting was done in the 0.5 – 7 keV band. The element abundances were fixed at Solar value, the hydrogen column density was fixed at the Galactic value. The results of spectral fits are summarized in Table 5.3.

All spectra shown in Figure 5.6 have a prominent power law component with the photon index of approximately $\Gamma \sim 2$ and a soft component of varying strength. It is strongest in the inner bulge where it by far dominates X-ray emission below 1.2 keV. The best-fit temperature of the soft component in the M31 spectra obtained in the two-component model is in the ∼ 0.3 – 0.4 keV range (Table 5.3). As can

be seen from the table, the simple two-component model consisting of a power law and optically-thin thermal plasma emission spectrum (MEKAL model in XSPEC) does not adequately describe the spectra, especially the spectrum of the inner bulge, having the largest number of counts. The deviations are due to the soft band, pointing at the complex shape of the soft component. With the second MEKAL component the fit improves significantly, the best fit parameters for the inner bulge spectrum are $kT_1 \approx 0.2$ keV and $kT_2 \approx 0.5$ keV with $\chi^2 = 227$ for 184 d.o.f. Making the element abundance a free parameter improves the fit quality of the three-component model further to $\chi^2 = 205$ for 183 d.o.f. with the best fit abundance of 0.17 of the solar value. We considered several other spectral models with free element abundance, they all produced sub-solar values in the range of $0.1 - 0.2$. We also tried to vary element abundances individually and found that the model is most sensitive to Ne, Fe and Ni abundances with the best fit achieved when the abundances of Ni is a free parameter. The two component (vmekal + power law) model requires the Ni abundance $\approx 3 - 4$ times solar value (abundances of other elements were fixed at solar). On the contrary, the models with the free Fe abundance give a subsolar best fit values for the latter, ~ 0.6. The fit quality improves further with the non-equilibrium thermal emission model (vnei model in XSPEC) with the best fit value of $n_e\, t \sim 5 \cdot 10^{11}$ sec/cm^3 and similar dependence on the element abundances as for vmekal model. All these modifications do not change the best fit temperature significantly. However, none of the models achieves acceptable values of χ^2. It is unclear, how much weight should be given to these results, as they can be an artifact of the inadequate spectral model and insufficient energy resolution of the ACIS-I detector. Indeed the emission from the inner bulge has a complex spectrum composed of several constituents of different temperature and ionization state, some of which may be out of the collisional ionization equilibrium.

The outer bulge spectrum has a less prominent soft component, approximately by a factor of 3 weaker than the inner bulge, but its temperature, $kT \approx 0.3$ keV, is compatible with the inner bulge value. The spectrum of M32 is similar, although only a very faint soft component is present here. Its temperature, $kT = 0.54 \pm 0.15$ keV may be somewhat higher than in M31. All three spectra (inner and outer bulge in M31 and M32) nearly perfectly match each other above ~ 1.2 keV, after normalization to the K-band flux. This is a strong argument in favor of their similar origin.

The emission from spiral arms clearly stands out. It does not have any significant soft component and, most importantly, its normalization (per unit K-band flux) is by a factor of $4 - 10$ higher in the hard band than for the other spectra. This difference is smaller in the soft band, however it is still significantly higher than the spectrum of the outer region. We describe this spectrum with a powerlaw model and we obtain $\Gamma = 2.0$. As with other spectra, the large χ^2 value indicates more complex spectral shape.

5.4.4 Morphology of the soft excess emission

To explore the spatial distribution of the soft excess emission we use two approaches. Firstly we consider the ratio of the $0.5 - 1.2$ keV X-ray image to the near-infrared image. The advantage of the ratio image is that it levels out the component in X-ray emission which is proportional to the K-band light. The disadvantage is that the X/K ratio may become very large at large central distances, where the X-ray emission is unrelated to old stellar population and deviates significantly from the K-band light

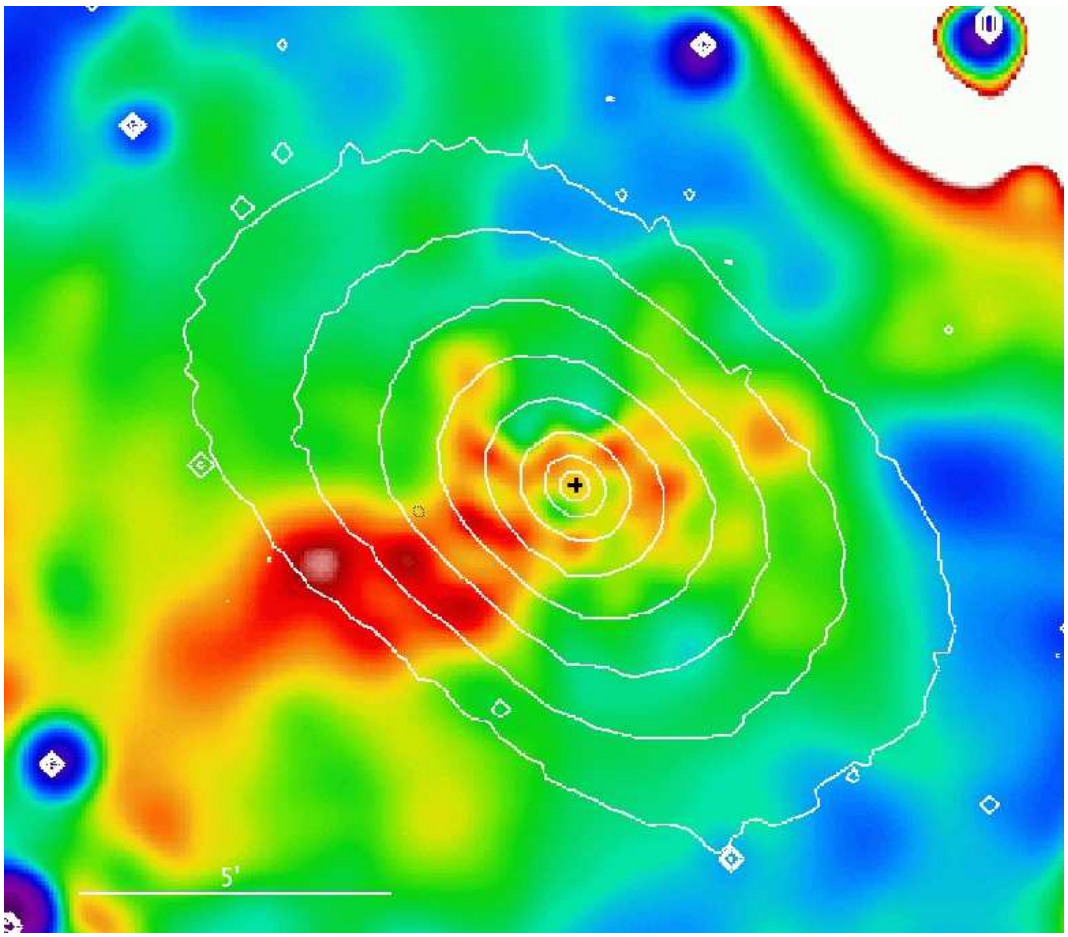

Figure 5.7: Ratio of 0.5 – 1.2 keV image to the the K-band image obtained from *Chandra* data. After the removal of the point sources the X-ray images were adaptively smoothed, the K-band image was smoothed correspondingly. The contours in show K-band brightness distribution. The center of M31 is marked with a cross. North is up and east is left.

distribution. Before producing the ratio image we excluded point sources and filled their locations with local background level using the `dmfilth` tool of CIAO. The X-ray images were adaptively smoothed and the near-infrared image was convolved with a gaussian with the width comparable to typical smoothing width near the center of X-ray image. The X-ray images were exposure corrected, the particle background and CXB was subtracted.

Figure 5.7 and Figure 5.8 shows the ratio images obtained from *Chandra* and *XMM-Newton* data. They are consistent with each other and illustrate very well the morphology of the soft excess emission. Comparison with the K-band contours shown in Figure 5.7 demonstrates clearly that the the soft excess emission has nothing to do with the old stellar population traced by the near-infrared light. Unlike stellar light, it is strongly elongated in the approximate direction of the minor axis of the galaxy extending beyond the boundaries of the bulge and projecting onto the 10-kpc starforming ring. The images also reveal strong east-west asymmetry, already seen in the minor axis distribution (Figure 5.4). As discussed in the Section 4.4.1, this asymmetry is caused by absorption of soft X-rays by the neutral and molecular gas in the spiral

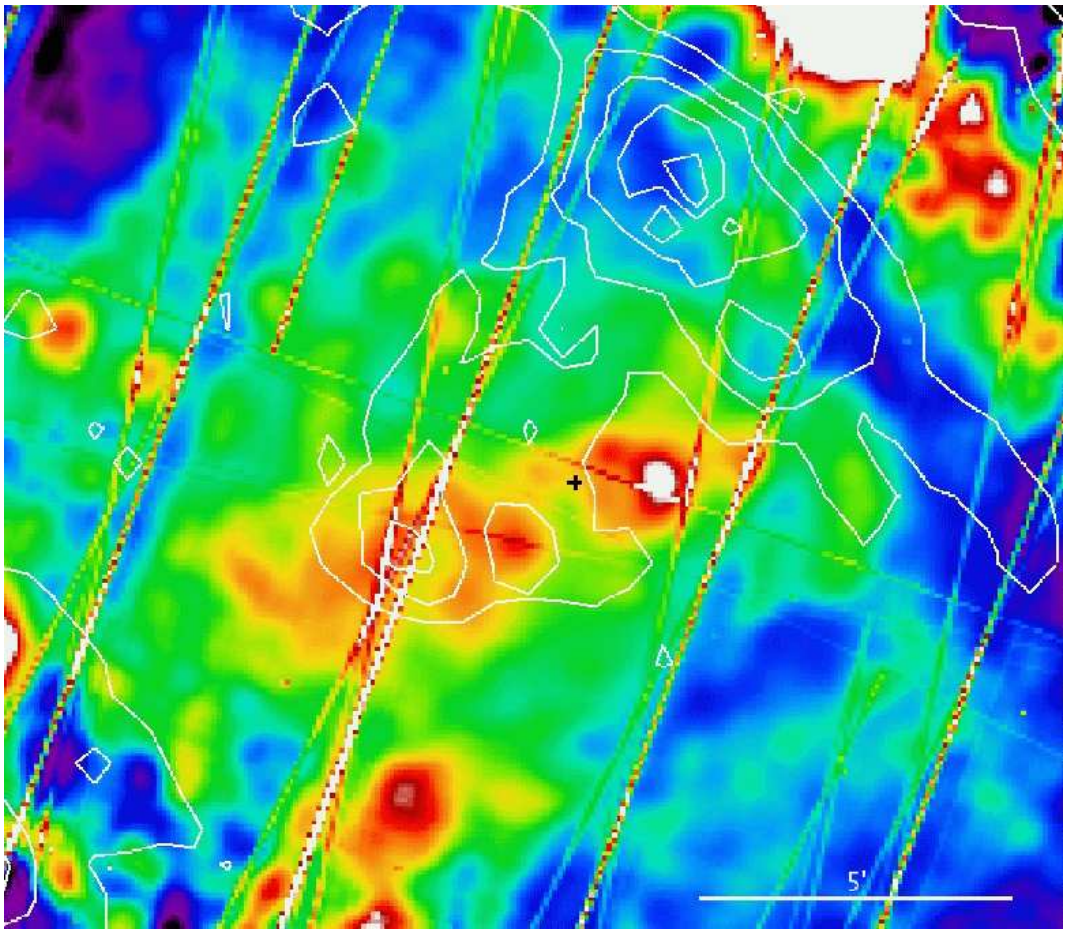

Figure 5.8: Same as Figure 5.7 but based on *XMM-Newton* data. The contours show the 160μm brightness distribution.

arms on the north-western side of the galactic disk. This conclusion is further supported by the anti-correlation between 160 μm flux and the soft X-ray brightness, with obvious shadows seen at the positions of spiral arms (Figure 5.8). At the same time, the gas and dust do not have any significant effect on the soft X-ray brightness in the south-eastern side of the galaxy.

In the second approach we consider the difference between the X-ray and the K-band images, the latter renormalized according to the X/K ratio of the old stellar population component. Unlike the ratio image it shows the true brightness distribution of the soft excess emission. For this purpose we used the same 0.5 – 1.2 keV *Chandra* image as for the ratio image; the normalization of K-band image was $4 \cdot 10^{27}$ erg s^{-1} L$_{\odot}^{-1}$. Figure 5.9 shows the result. The image generally confirms the overall morphology of the soft emission revealed by the ratio image.

The images show significant sub-structures in the inner $\sim$ 100 – 150 arcsec with the angular scale of about 30 arcsec. The origin of this substructures is not clear, although some correlation with the position of the peaks on the 160 μm image suggests that at least some of them may be caused by absorption. These sub-structures may deserve a special study which is beyond the scope of this paper.

5.4.5 L_X/L_K ratios

We calculate ratios of X-ray to K-band luminosity for the same spatial regions as used for the spectral analysis, characterizing the inner and outer bulge and spiral arms. As suggested by the spectra the natural boundary between the soft and hard energy bands is 1.2 keV. However, in order to facilitate comparison with previous studies we computed the ratios in the $0.5-2$ keV and $2-10$ keV energy bands. The X-ray luminosities for these bands were computed using the best fit spectral models. The errors for the luminosity and, correspondingly, for X/K ratios account for the model normalization error only and do not include uncertainties in the spectral parameters or any other systematic uncertainties. In computing the hard band luminosity we extrapolated the best fit model outside the energy range used for spectral fits, 0.5-7 keV. The K-band luminosities were calculated in each region using the 2MASS image.

The L_X/L_K ratios are presented in Table 5.4. These numbers can be transformed to X-ray-to-mass ratios dividing them with the K-band mass-to-light ratio, which is of the order of unity. Its value can be computed using the $B-V \approx 0.95$ colour index from Walterbos & Kennicutt (1987) and applying the relation between $M_\star/L_K$ and the B–V colour (Bell & de Jong, 2001), which gives $M_*/L_K \approx 0.85$. A close values has been derived by Kent (1992) based on the dynamical mass measurement, $M_*/L_K \approx 1.1$. We compare the X/K ratios for M31 with M32 and Milky Way. The M32 numbers were obtained from the spectra of Section 5.4.3 in the same way as for M31. For the Milky Way we used results from Revnivtsev et al. (2006) and Sazonov et al. (2006), and transformed them to L_X/L_K for two values of K-band mass-to-light ratio, 0.7 (Dwek et al., 1995) and 1 (Kent, 1992). The X/K ratio in Sazonov et al. (2006) is given for the $0.1-2.4$ keV band, following them we converted it to the $0.5-2$ keV band multiplying by 0.7 which is typical ratio for coronally active stars (Fleming et al., 1995). The contribution of young stars is excluded. Revnivtsev et al. (2006) used data from RXTE in the $3-20$ keV and calculated the $2-10$ keV luminosities assuming a powerlaw spectrum with $\Gamma = 2.1$.

In the $2-10$ keV band the X-ray to K-band ratios for bulge regions in M31 and for M32 are compatible with each other and appear to exceed slightly the Milky Way value. This may be explained by the difference in the spectral shape assumed in the flux calculation. Assuming the same power law with $\Gamma = 2.1$ as used by Revnivtsev et al. (2006), we obtained for M31 $L_X/L_K = (3.0 \pm 0.1) \cdot 10^{27}$ erg s^{-1} L$_\odot^{-1}$, in agreement with the Milky Way value. The good agreement of the X-ray to K-band ratios suggests similar origin of the 2–10 keV emission in all three galaxies, as discussed in more detail in the following Section.

In the soft band, the X/K ratios for M31 are systematically larger than M32 ones. This is to be expected from the spectra (Figure 5.6) and is due to the presence of the soft excess emission in M31. Also, in interpreting the soft band ratios the interstellar absorption should be taken into account. Indeed, Sazonov et al. (2006) studied sources in the Solar neighborhood where the absorption is insignificant. The M31 and M32 data, on the contrary, is subject to the galactic absorption, with values of $6.7 \cdot 10^{20}$ and $6.3 \cdot 10^{20}$ cm^{-2} respectively (Dickey & Lockman, 1990). In addition, M31 has spatially variable internal absorption reaching few$\cdot 10^{21}$ cm^{-2} in the spiral arm regions (Nieten et al., 2006). The total NH for the outer bulge region in M31 is probably in the range $(7-10) \cdot 10^{20}$ cm^{-2}, giving the absorption corrected value of the soft band X/K ratio $L_X/L_K \approx (8-10) \cdot 10^{27}$ erg s^{-1} L$_\odot^{-1}$. For M32 we obtain after absorption correction $L_X/L_K \approx 4.3 \cdot 10^{27}$ erg s^{-1} L$_\odot^{-1}$. Taking into account the uncertainties quoted by Sazonov et al.

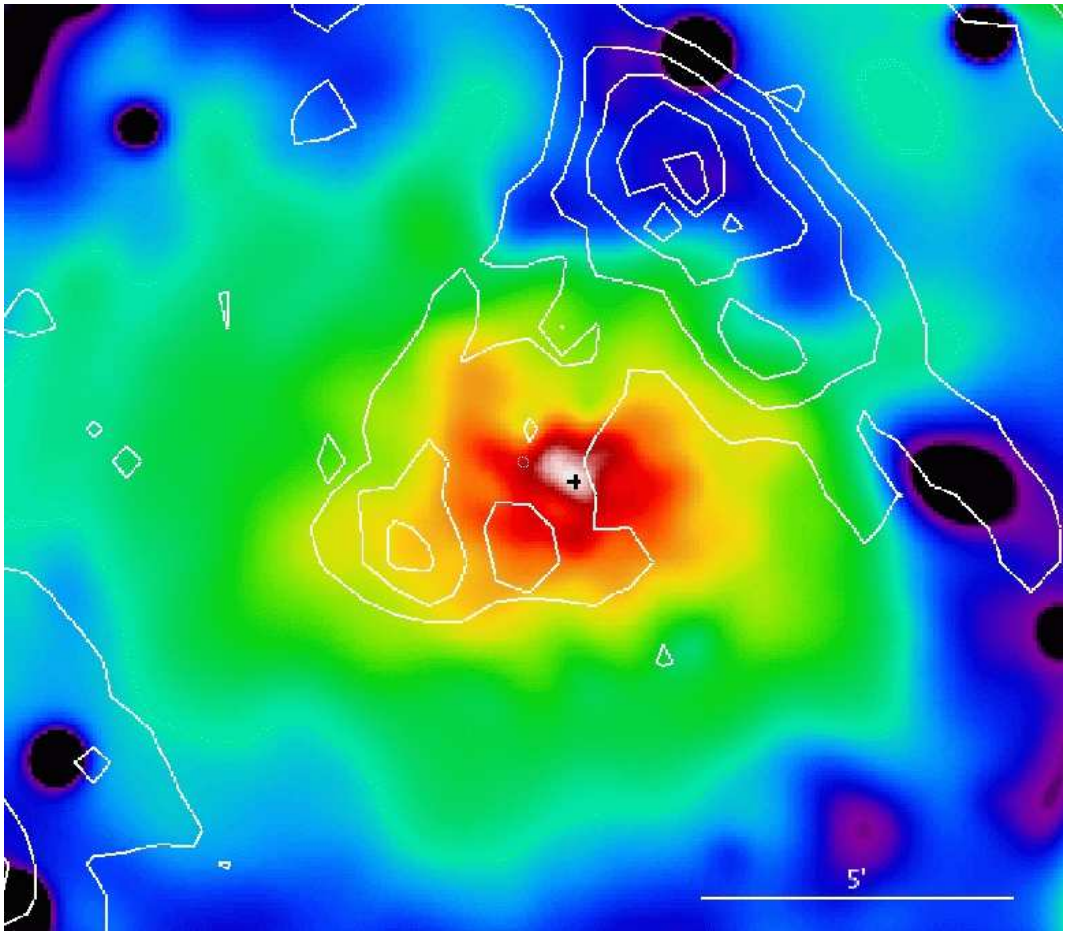

Figure 5.9: The spatial distribution of the soft component. The difference between *Chandra* image in the 0.5 – 1.2 keV band and the K-band image normalized according to the X/K ratio of the outer bulge. The contours show the intensity levels of 160 μm Spitzer image. The center of M31 is marked with a cross. North is up and east is left.

(2006) and uncertainties in the K-band mass-to-light ratio the X/K ratio for Solar neighborhood is formally compatible with the absorption corrected value for M31 and probably slightly higher than for M32. It is unclear, how much weight should be given to this discrepancy due to the number and amplitude of uncertainties involved. The absorption corrected value for the inner bulge of M31 is definitely larger, $L_X/L_K \approx (12-15)\cdot 10^{27}$ erg s^{-1} L$_\odot^{-1}$.

The X/K ratios in the spiral arm region are significantly higher. The additional internal absorption can be upto few$\cdot 10^{21}$ cm^{-2}, resulting in the absorption correction factor in the soft band as large as ≈ 4. The final X/K ratios in both bands are approximately an order of magnitude larger than for the Milky Way.

Table 5.4: X-ray to K-band luminosity ratios in different regions in M31 and in M32 compared to the Milky Way. All values are given in units of 10^{27} erg s^{-1} L$_{\odot}^{-1}$.

	0.5 – 2 keV[a]	2 – 10 keV
M31 inner bulge	9.4 ± 0.1	4.5 ± 0.1
M31 outer bulge	6.2 ± 0.1	3.6 ± 0.2
M31 spiral arms	22.1 ± 0.3	31.4 ± 0.6
M32 total	3.5 ± 0.1	4.1 ± 0.2
Galaxy Sazonov et al. (2006) [b]	7.3 – 10.5 (±3)	2.2 – 3.1 (±0.8)
Galaxy Revnivtsev et al. (2006) [b]	–	2.2 – 3.1 (±0.5)

[a] The X/K ratios for M31 and M32 were not corrected for absorption. See the text for the absorption corrected values.
[b] The X/M_* ratios were converted to X/K ratios assuming two values of the K-band mass-to-light ratio, 0.7 (first number) and 1.0; the uncertainty given in the parenthesis corresponds to $M_*/L_K = 1$

5.5 Discussion

5.5.1 Faint compact sources

We showed that a broad-band emission component exists in M31 which (i) follows the K-band light distribution and (ii) its 2 – 10 keV X/K ratio is identical to that of M32 and Milky Way. These suggest beyond reasonable doubt that this component has similar origin to the Galactic Ridge X-ray emission of the Milky Way (Revnivtsev et al., 2006). Namely, it is associated with the old stellar population and is a superposition of a large number of weak sources of stellar type, the main contributors in the 2–10 keV band being cataclysmic variables and coronally active binaries (Sazonov et al., 2006).

The X/K ratios are compatible between all three galaxies in the 2–10 keV band, but in the soft band they differ in M31 and M32 (Table 5.4). In the inner bulge this difference is clearly due to the contribution of the soft emission from the ionized gas, as discussed below. Although we chose the outer bulge region as far as possible along the major axis of the galaxy, where the soft X-ray brightness follows the K-band profile, some residual contribution from the gas can not be entirely excluded. Therefore it is not clear if this difference reflects genuine difference between properties and/or content of X-ray emitting stellar populations in these two galaxies. Due to large systematic uncertainties, the Milky Way value is formally compatible with both galaxies and any quantitative comparison is inconclusive at this point.

5.5.2 Ionized gas

There are several arguments which suggest that the excess soft component has a non-stellar origin. The most important is the morphology of the excess emission, namely the striking difference from the distribution of the near-infrared light (Figure 5.7 and Figure 5.8). As no significant color gradients are observed in the bulge of M31 (Walterbos & Kennicutt, 1988), its stellar content must be sufficiently uni-

form and can not give rise to the observed non-uniformities in the X/K ratio. Enhanced X-ray to K-band ratio could be explained if a notable young population was present in the bulge, which is also not the case (Stephens et al., 2003). With the stellar origin excluded, it is plausible that the soft excess emission is of truly diffuse nature and originates from ionized gas of $\sim 0.3 - 0.4$ keV temperature.

To study the physical properties of the ionized gas we use a rectangular region on the south-eastern side of the galaxy, to avoid the complications due to attenuation by the spiral arms on the north-western side. The size of the region is 8 arcmin along the major axis and 10 arcmin along the minor axis of the galaxy. From the spectral fit, the total X-ray luminosity of the soft component in the $0.5 - 2$ keV energy range is $\approx 10^{38}$ erg/s, after the absorption and bolometric correction the total bolometric luminosity is $L_{bol} \approx 2.3 \cdot 10^{38}$ erg/s assuming Galactic column density. From the emission measure of the gas, $\int n_e n_H dV = 6.3 \cdot 10^{60}$ cm^{-3}, we estimate that the mass of the gas in the studied volume is of the order of $\sim 10^6$ M$_\odot$. We note, that assuming the symmetry between the north-western and south-eastern sides of the galaxy, the total quantities for the mass and bolometric luminosity are twice the quoted values. The average number density is about $n_e \sim 7 \cdot 10^{-3}$ cm^{-3}. The cooling time of the gas is $t_{cool} = (3kT)/(n_e \Lambda(T)) \sim 250$ million years. We also applied a two temperature model to the soft emission and obtained for the two components: $kT_1 \sim 0.25$ keV, $kT_2 \sim 0.6$ keV, bolometric luminosities of $\sim 2 \cdot 10^{38}$ and $\sim 10^{38}$ erg/s, total masses of $\sim 10^6$ and $\sim 0.6 \cdot 10^6$ M$_\odot$ and cooling times of ~ 200 and ~ 800 million years. We mention that the above computed values strongly depend on the applied spectral model.

The morphology of the gas indicates that it is not in the hydrostatic equilibrium in the gravitational potential of the galaxy. It suggests rather, that gas is outflowing from the bulge in the direction perpendicular to the galactic disk (see also Li & Wang, 2007). The mass and energy budget of the outflow can be maintained by the mass loss from the evolved stars and Type Ia supernovae. Knapp et al. (1992) estimated the mass loss rate from evolved stars for elliptical galaxies $\sim 0.0021\ L_K/L_{K,\odot}$ M$_\odot$ Gyr^{-1}. This rate can be applicable to the bulge of M31 as the stellar populations are similar. The K-band luminosity of this region is $L_K = 1.4 \cdot 10^{10}$ L$_{K,\odot}$. The estimated total mass loss rate is ≈ 0.03 M$_\odot$/yr. The stellar yields produce the total amount of the observed gas on a timescale of ~ 35 million years which is shorter than the cooling timescale of the gas.

To estimate the energy input from type Ia supernovae we use results of Mannucci et al. (2005) who give the supernova rate of $N_{\rm SN\ Ia} = 0.035^{+0.013}_{-0.011}$ SNu for E and S0 galaxies, where 1 SNu = 1 SN/10^{10} $L_{K,\odot}$ per century. Assuming that one supernova releases $E_{\rm SN\ Ia} = 10^{51}$ ergs into the interstellar medium, we obtain about $1.5 \cdot 10^{40}$ erg/s energy that goes into ISM. The minimal energy required to lift the gas in the gravitational potential of the galaxy can be calculated from $E_{lift} = 7.2 \dot{M}_\star \sigma_\star^2$ (David et al., 2006). With $\sigma_\star = 156 \pm 23$ km/s (Lawrie, 1983) we obtain $\sim 3.3 \cdot 10^{39}$ erg/s. If the gas is heated to the observed temperature by supernovae, it requires $\sim 10^{39}$ erg/s. This estimates indicate that the energy input from supernovae is approximately $\sim 3-4$ times larger than the minimal energy required to drive a galactic wind from the galaxy, similar to the result of David et al. (2006) for low-luminosity ellipticals.

Type Ia supernovae will also contribute to the chemical enrichment of ISM with iron-peak elements. Typically 0.7 M$_\odot$ of iron is provided by each SN Ia event (Nomoto et al. 1984; Shigeyama et al. 1992; Iwamoto et al., 1999), that gives about $3.4 \cdot 10^{-4}$ M$_\odot$ of iron per year. Assuming complete mixing of the supernova ejecta with the stellar wind material we would expect the iron abundance in the hot ISM $\approx 1.1 \cdot 10^{-2}$ by mass,

which exceeds the Solar value of $1.9 \cdot 10^{-3}$ (Anders & Grevesse, 1989) by a factor of ~ 6. The observed spectra are inconsistent with high iron abundance in simple one- or two-component thermal models, but these models can not adequately describe the spectra anyway, therefore this result can not be used as a conclusive argument. On the other hand, the discrepancy between high predicted and low observed abundance of iron is a well-known problem for elliptical galaxies, where type Ia supernovae also plays important role in thermal and chemical evolution of the ISM; it has been addressed in a number of studies, e.g. Brighenti & Mathews (2005). We also note, that although the iron is the primary element by mass in the type Ia supernovae ejecta, the ISM will be also enriched by other elements, most significantly by nickel. The detailed analysis of this problem is beyond the scope of the present paper.

Assuming that the gas leaves the galaxy in a steady state wind along the axis perpendicular to the plane of the disk, the outflow speed v_w can be calculated from $\dot{M}_\star = \pi r^2 \rho_{gas} v_w$ where ρ_{gas} is the average gas density estimated above and r is the radius of the base of the imaginary cylinder filled with the outflowing gas. This calculation gives $v_w \sim 60$ km/s which is smaller by a factor of few than the local sound speed. Such a slow sub-sonic motion of the gas can not explain the observed elongated shape of the gas distribution, which may be related to the the magnetic fields and galactic rotation. We can use the fact that the shadow from the 10-kpc star-forming ring is present to estimate the extent of the gas along the axis perpendicular to the galactic disk. The angular distance of the shadow from the center is $\sim 600 - 700$ arcsec, giving the "vertical" extent of the gas of $\gtrsim 2.5$ kpc.

5.5.3 Spiral arms

The ~ 10 times higher X-ray to K-band ratios observed in the spiral arms (Table 5.4) and their different emission spectrum (Figure 5.6) suggest that X-ray emission from spiral arms has different nature than the bulge. As spiral arms are associated with star-formation, an obvious candidate is X-ray emission from young stellar objects (protostars and pre-main sequence stars) and young stars, which are well-known sources of X-ray radiation (Koyama et al. 1996; Carkner et al. 1998; Giardino et al., 2007).

As X-ray emission from the spiral arms is associated with young objects, it is natural to characterize it with L_X/SFR ratio. We compute this ratio for the regions used in spectral analysis. The FIR flux was determined from the 160 μm Spitzer image, 290 Jy. In computing this value we subtracted the blank-sky background of nearby fields. To convert it to SFR we used results of IR spectral fits from Gordon et al. (2006), which gave SFR $= 9.5 \cdot 10^{-5} F_{160\mu}$/Jy $M_\odot$/yr for the M31 distance. Thus we obtained the star-formation rate of 0.028 $M_\odot$/yr in the region used for the analysis. The X-ray luminosity in the same region is $3 \cdot 10^{37}$ erg/s in the $2 - 10$ keV band. After subtracting the X-ray emission due to the old stellar population we obtain $2.6 \cdot 10^{37}$ erg/s energy. From this we can compute $L_X/\mathrm{SFR} \approx 9.4 \cdot 10^{38}$ (erg/s)/($M_\odot$/yr). This value is $\sim 1/3$ of the total L_X/SFR arising from HMXBs which is $2.5 \cdot 10^{39}$ (erg/s)/($M_\odot$/yr) (Grimm et al. 2003; Shtykovskiy & Gilfanov, 2005).

5.6 Conclusion

We investigated the origin of unresolved X-ray emission from M31 using *Chandra* and *XMM-Newton* data. We demonstrated that it consists of three different components:

1. Broad-band emission associated with old population, similar to the Galactic ridge emission in the Milky Way. It is a a combined emission of a large number of weak unresolved sources of stellar type, the main contribution being from cataclysmic variables and active binaries. The surface brightness distribution of this component approximately follows the distribution of K-band light. The absorption corrected X-ray to K-band luminosity ratios are compatible with the Milky Way values. The total luminosity of this component inside central 800×400 arcsec is of the order of $\sim 3 \cdot 10^{38}$ erg/s in the $0.5 - 10$ keV band.

2. Soft emission localized in the inner bulge of the galaxy along its minor axis. This emission is from ionized gas with the temperature of the order of $\sim$ 300 eV, although its spectrum can not be adequately described by a simple one- or two-temperature model of optically-thin emission from a gas in a collisional ionization equilibrium. The $0.5 - 2$ keV luminosity in the central 8×20 arcmin area is $\sim 2 \cdot 10^{38}$ erg/s, the absorption corrected bolometric luminosity is $\sim 5 \cdot 10^{38}$ erg/s. The total mass of the gas is $\sim 2 \cdot 10^6$ $M_\odot$, its cooling time $\sim$ 250 Myrs. The surface brightness distribution is drastically different from the stellar light distribution, it is significantly elongated along the minor axis of the galaxy. The morphology of the soft emission suggests that gas outflows along the direction perpendicular to the galactic plane. The mass and energy budget is maintained by the mass loss by the evolved stars and type Ia supernovae. The "vertical" extent of the gas exceeds $\gtrsim$ 2.5 kpc. These results are in good agreement with those recently obtained by Li & Wang (2007).

3. Hard emission from spiral arms. In the 0.5–7 keV band this emission has approximate power law shape with $\Gamma \approx 2$. It is most likely associated with star-forming regions and is due to young stellar objects and young stars. The $L_X/SFR \approx 9.4 \cdot 10^{38}$ (erg/s)/($M_\odot$/yr) which is about $\sim 1/3$ of the contribution of HMXBs.

Acknowledgements. We thank the anonymous referee for useful and constructive comments. This research has made use of *Chandra* archival data provided by the Chandra X-ray Center. *XMM-Newton* is an ESA science mission with instruments and contributions directly funded by ESA Member States and the USA (NASA). This publication makes use of data products from Two Micron All Sky Survey, which is a joint project of the University of Massachusetts and the Infrared Processing and Analysis Center/California Institute of Technology, funded by the National Aeronautics and Space Administration and the National Science Foundation. The Spitzer Space telescope is operated by the Jet Propulsion Laboratory, California Institute of Technology, under contract with the National Aeronautics and Space Administration. (Anders & Grevesse, 1989)

Bibliography

Anders, E., Grevesse, N. 1989, Geochimica et Cosmochimica Acta, 53, 197

Baldi, A., Raymond, J. C., Fabbiano, G., et al. 2006, ApJ, 636, 158

Bell, E. F., de Jong, R. S. 2001, ApJ, 550, 212

Borozdin, K. N., Priedhorsky, W. C. 2000, ApJ, 542, L13

Brighenti, F., Mathews, W. G. 2005, ApJ, 630, 864

Carkner, L., Kozak, J. A., Feigelson, E. D., 1998, AJ, 116, 1933

David, L. P., Forman, W., Jones, C. 1990, ApJ, 359, 29

David, L. P., Jones, C., Forman, W., et al. 2006, ApJ, 653, 207

Dickey, J. M., Lockman, F. J., 1990, ARA&A, 28, 215

Dwek, E., Arendt, R. G., Hauser, M. G., et al. 1995, 445, 716

Fabbiano, G. 2006, ARA&A, 44, 323

Fabbiano, G., Trinchieri, G., van Speybroeck, L. S. 1987, ApJ, 316, 127

Fleming, T. A., Molendi, S., Maccacaro, T., Wolter, A. 1995, ApJS, 99, 701

Giardino, G., Favata, F., Micela, G., et al. 2007, A&A, 463, 275

Gilfanov, M. 2004, MNRAS, 349, 146

Gordon, K. D., Bailin, J., Engelbracht, C. W., et al. 2006, ApJ, 638, L87

Grimm, H.-J., Gilfanov, M., Sunyaev, R. 2003, MNRAS, 339, 793

Henderson, A. P., 1979, A&A, 75, 311

Hickox, R. C., Markevitch, M., 2006, ApJ, 645, 95

Irwin, J. A., Bregman, J. N. 1999, ApJ, 527, 125

Iwamoto, K., Brachwitz, F., Nomoto, K., et al. 1999, ApJS, 125, 439

Jarrett, T. H., Chester, T., Cutri, R., et al. 2003, AJ, 125, 525

Kent, S. M. 1992, 387, 181

Kim, D.-W., Fabbiano, G. 2003, ApJ, 586, 826

Knapp, G. R., Gunn, J. E., Wynn-Williams, C. G. 1992, ApJ, 399, 76

Koyama, K., Hamaguchi, K., Ueno, S., et al. 1996, PASJ, 48, 87

Lawrie, D. G., 1983, ApJ, 273, 562

Li, Z., Wang, Q. D., 2007, ApJ, 668, L39

Macri, L. M. 2001, ApJ, 549, 721

Mannucci, F., Della Valle, M., Panagia, N., et al. 2005, A&A, 433, 807

Moretti, A., Campana, S., Lazzati, D., Tagliaferri, G. 2003, ApJ, 588, 696

Nevalainen, J., Markevitch M. and Lumb, D. 2005, ApJ, 629, 172

Nieten, Ch., Neininger, N., Guelin, M., et al. 2006, A&A, 453, 459

Nomoto, K., Thielemann, F.-K., Yokoi, K. 1984, ApJ, 286, 644

Primini, F. A., Forman, W., Jones, C. 1993, ApJ, 410, 615

Revnivtsev, M., Sazonov, S., Gilfanov, M., et al. 2006, A&A, 452, 169

Revnivtsev, M., Churazov, E., Sazonov, S., et al. 2007, A&A, 473, 783

Rieke, G. H., Young, E. T., Engelbracht, C. W., et al. 2004, ApJS, 154, 25

Sazonov, S., Revnivtsev, M., Gilfanov, M., et al. 2006, A&A, 450, 117

Shigeyama, T., Nomoto, K., Yamaoka, H., Thielemann, F.-K. 1992, ApJ, 386, L13

Shirey, R., Soria, R., Borozdin, K., et al. 2001, A&A, 365, L195

Shtykovskiy, P., Gilfanov, M. 2005, A&A, 431, 597

Simien, F., Athanassoula, E., Pellet, A. et al. 1978, A&A, 67, 73

Stanek, K. Z., Garnavich, P. M., 1998, ApJ, 503, 131

Stephens, A. W., Frogel, J. A., DePoy, D. L., et al. 2003, AJ, 125, 2473

Strüder, L., Briel, U., Dennerl, K., et al. 2001, A&A, 365, L18

Supper, R., Hasinger, G., Pietsch, W., et al. 1997, A&A, 317, 328

Takahashi, H., Okada, Y., Kokubun, M., Makishima, K. 2004, ApJ, 615, 242

Trinchieri, G., Fabbiano, G. 1991, ApJ, 382, 82

Turner, M. J. L., Abbey, A., Arnaud, M., et al. 2001, A&A, 365, L27

van Speybroeck, L., Epstein, A., Forman, W., et al. 1979, ApJ, 234, 45

Voss, R., Gilfanov, M., 2007, A&A, 468, 49

Walterbos, R. A. M., Kennicutt, R. C. 1987, A&AS, 69, 311

Walterbos, R. A. M., Kennicutt, R. C. 1988, A&A, 198, 61

West, R. G., Barber, C. R., Folgheraiter, E. L. 1997, MNRAS, 287, 10

Chapter 6

Conclusions

In this dissertation we studied the progenitor scenarios of Type Ia Supernovae (SNe Ia). There is a wide agreement that SNe Ia originate from thermonuclear explosions of white dwarfs. The nuclear runaway that leads to the explosion could start in a white dwarf gradually accumulating matter from a companion star until it reaches the Chandrasekhar mass limit, or could be triggered by the merger of two white dwarfs in a compact binary system. The X-ray signatures of the two possible paths are completely different, in the accretion scenario $\sim 3 \cdot 10^{51}$ erg energy is emitted prior to the Supernova explosion on a timescale of $\sim 10^7$ years, whereas in the merger scenario no significant electromagnetic emission is predicted. This offers a means to determine which scenario dominates.

We computed the predicted X-ray luminosity in the $0.3-0.7$ keV energy range in the accretion scenario in a sample of six early-type galaxies and galaxy bulges. The SN Ia rate was estimated based on the near-infrared luminosity of galaxies, and the energy range was optimized in order to detect emission from steady nuclear burning white dwarfs, taking into account the range of effective temperatures, absorption column densities, and the effective area curve of *Chandra*. We found that the accretion scenario predicts an X-ray luminosity of $\sim 10^{40}$ erg s^{-1} per 10^{11} $L_{K,\odot}$, the exact value depends on the column density towards the galaxy. We confronted this luminosity with observed *Chandra* upper limits on the combined X-ray emission from the population of nuclear burning white dwarfs in the same energy range. The resulting luminosity is fairly uniform in the studied galaxies, $\sim 2.5 \cdot 10^{38}$ erg s^{-1} per 10^{11} $L_{K,\odot}$, and is weakly dependent on the column density.

Based on these we concluded that in early-type galaxies the observed X-ray flux is $\sim 30 - 50$ times less than predicted in the accretion scenario. This result implies that no more than about 5 per cent of SNe Ia, associated with the old stellar population, can be produced in accreting binary systems. At present the only viable alternative is the merger of two white dwarfs, hence we concluded that SNe Ia in early-type galaxies predominantly arise from the double-degenerate scenario.

Using a similar line of arguments we derived constraints on the nature of progenitors of Classical Novae (CNe). These events are another type of thermonuclear explosions associated with accreting white dwarfs, occurring upon accumulation of certain amount ($\Delta M \sim 10^{-4}-10^{-5}$ $M_\odot$) of hydrogen-rich material. The frequency of CNe in a galaxy depends on the mass accretion rate onto the white dwarfs. During

accretion energy is released in the optical, ultraviolet, or X-ray wavelengths, depending on the nature of the progenitor system. Magnetic systems, such as polars and intermediate polars, are sources of hard X-rays produced via optically-thin bremsstrahlung emission. Dwarf novae in quiescence also radiate relatively hard X-rays from their optically-thin boundary layer, whereas in outburst state the optically-thick accretion disk emits predominantly in the ultraviolet and soft X-ray bands.

We computed the X-ray luminosity of magnetic systems and dwarf novae in quiescence in M31 galaxy based on the CN rate and compared with *Chandra* observations of the galaxy. We demonstrated that no more than about 10 per cent of CNe can be produced in magnetic cataclysmic variables, the upper limit being about 3 per cent for a typical CN progenitor with $M_{WD} \approx 0.9$ $M_\odot$ and with an accretion rate of $\dot{M} \approx 10^{-9}$ $M_\odot$/yr. We also pointed out that in dwarf novae at least $\sim$ 90 per cent of the material must be accreted during outbursts, when the emission spectrum is soft, and only a small fraction in quiescent periods.

We also investigated the properties and origin of the unresolved X-ray emission from M31. The proximity of our close-by neighbor gives a unique opportunity to explore a spiral galaxy, very similar to the Milky Way without complications brought about by projection and absorption effects. The bulge of M31 is covered by *Chandra* data, whereas the entire galaxy was observed in a survey completed by *XMM-Newton*. The rich available data set allowed to resolve and remove bright sources down to the luminosity threshold of $\sim 10^{35}$ erg s^{-1} and $\sim 10^{36}$ erg s^{-1} in the bulge and the disk of M31. We demonstrated that the unresolved X-ray emission consists of three different components.

One of them is broad-band emission from large number of faint sources – mainly accreting white dwarfs and active binaries associated with the old stellar population, similar to the Galactic Ridge X-ray emission of the Milky Way. The surface brightness distribution of this component approximately follows the distribution of near-infrared light. The obtained X-ray to K-band luminosity ratios are consistent with those observed for the Milky Way, M32, and M105 galaxies. The total luminosity of this component is $\sim 6 \cdot 10^{38}$ erg s^{-1} in the 0.5 – 8 keV energy range.

Another X-ray emitting component originates from ionized gas with temperature of the order of $kT \sim$ 300 eV. The mass of the gas is $\sim 2 \cdot 10^6$ $M_\odot$ and its total absorption-corrected bolometric luminosity is $\sim 2 \cdot 10^{38}$ erg s^{-1}. The gas is significantly extended along the minor axis of the galaxy, suggesting that it outflows along the direction perpendicular to the galactic plane. We found that the mass and energy budget of the galactic wind can be sustained by the mass loss from evolved stars and by the energy input from SNe Ia. We also detected a shadow cast in the gas emission by spiral arms and the 10-kpc star-forming ring, which can be used to place a lower limit on the "vertical" extent of the outflow, being greater than $\sim$ 2.5 kpc.

The third X-ray emitting component is associated with the 10-kpc star-forming ring and spiral arms of M31. We characterized the X-ray emission from star-forming regions with the L_X/SFR (star-formation rate) ratio. We explored the L_X/SFR ratio in the 0.5 – 2 keV energy band along the 10-kpc star-forming ring, and found that it is in the range of $(0.9 – 1.8) \cdot 10^{38}$ (erg s^{-1})/($M_\odot$/yr), excluding the regions near the minor axis of the galaxy where it is $\sim 1.5 – 2$ times higher. The latter may be associated with warm ionized

gas of the galactic wind rather than with the star-forming ring itself. An obvious candidate to the X-ray emission from star-forming regions are young stellar objects (protostars and pre-main sequence stars) and young stars, which are well-known sources of X-ray radiation.

Acknowledgments

I would like to thank Rashid Sunyaev that I could be a member of his group at MPA and for his generous support.

I am very grateful to Marat Gilfanov for the stimulating scientific adventure we spent together in the last three years. I owe him special thanks for always inspiring me, for the extensive scientific discussions, and last but not least for the Friday-night paper submissions.

I wish to thank Zhongli, Stefano, Igor, and Pavel the time we shared at the institute and at conferences. I thank Markus that he was always open for my scientific and non-scientific questions.

I would like to thank my parents that they always supported and believed in me.

I owe my deepest gratitude to my wife, Erika, who was always there for me. We did not only share a lot of fun together, but she also gave me the hope in the hardest moments.

Curriculum Vitae

Name: Ákos Bogdán

Nationality: Hungarian

Education

2006 - 2010:	**Ph.D. Astrophysics**, Max Planck Institute for Astrophysics Dissertation title: X-ray emission from nearby early-type galaxies and origin of Type Ia Supernovae Research Advisors: Marat Gilfanov Rashid Sunyaev
2001 - 2006:	**M.Sc. Astronomy**, Eötvös Loránd University, Budapest, Hungary Thesis title: Transition between galactic and extragalactic sources in cosmic ray propagation Research Advisors: Peter L. Biermann Kristóf Petrovay
2005:	Erasmus fellowship at the University of Bonn Research Advisor: Peter L. Biermann
1997 - 2001:	Klára Leőwey High School, Pécs, Hungary